Spring 1994

High Energy Coupled Nucleon Tranpsort in One Dimension

Stanley L. Lamkin
Old Dominion University

HIGH ENERGY COUPLED NUCLEON TRANSPORT IN ONE DIMENSION

by

Stanley L. Lamkin

B. S. June 1969, Old Dominion College
M. S. December 1974, Old Dominion University

A Dissertation Submitted to the Faculty of
Old Dominion University in Partial Fulfillment of the
Requirements for the Degree of

DOCTOR OF PHILOSOPHY

APPLIED PHYSICS

OLD DOMINION UNIVERSITY

April 1994

Approved by:

_____
Dr. Govind S. Khandelwal (Director)

_____

_____

_____

_____

_____

ABSTRACT

The problem of energetic nucleon transport through extended bulk matter is considered in the context of the 'straight ahead' approximation. The applicable form of the Boltzmann transport equation is derived and solved in one dimension. The production term for secondary generation nucleons due to nuclear fragmentation includes 'coupling' of the flux to other types of nucleon projectiles. A physically motivated perturbation series approach is developed to enhance solution convergence. The Boltzmann operator is inverted and the flux is computed using a numerical marching scheme. The secondary production integrals are optimized for second order accuracy using a set of analytical benchmarks. The benchmarks provide precise estimation of the truncation errors involved in the numerical method. A set of continuous benchmarks are developed for cosmic ray transport applications and a set of mono-energetic benchmarks is developed for accelerator applications. The optimized marching scheme is incorporated into the BRYNTRN transport code along with a sophisticated reaction database for nuclear and atomic scattering. The method is applied to typical space shielding applications and comparisons are made with the HETC Monte Carlo benchmarks. The BRYNTRN results compare well with HETC while requiring significantly less computing power. The transport of elastically scattered neutrons is shown to be poorly converged using the coarse energy grids suited to non-elastic scattering. A grid independent model is developed for neutron elastic scattering which maintains particle conservation to within acceptable limits for deep penetration transport cases. The elastic scattering model is applied to a range of shielding cases.

DEDICATION

This work is dedicated to my parents, Paul and Mary Lamkin, and to my wife, Jean G. Lamkin.

ACKNOWLEDGMENTS

This dissertation would not have been written without the encouragement and assistance of many people including teachers, colleagues, and friends. Two people, in particular, have contributed to the success of this effort. Professor Govind Khandelwal has served as a mentor and friend since my undergraduate days. When I first developed an interest in computational physics as an undergraduate, Dr. Khandelwal created an opportunity for me to become involved with ODU's early efforts to do scientific research on the computer. That introduction to computers became the foundation for my basic career path. Several years after I graduated with a bachelor's degree, I contacted Dr. Khandelwal when I decided to return to ODU to study for a master's degree. He welcomed me back by providing both intellectual challenges and funding grants so I was able to continue my studies and grow as a physicist. In the mid-1980's I once again asked for guidance and assistance. As I had hoped, Dr. Khandelwal responded by linking me with all of the support and academic programs which would enable me to pursue this doctorate successfully. In my mind, Govind Khandelwal epitomizies the ideal of a teacher, requiring me to perform at the highest intellectual level while ensuring that I have the resources and opportunities to achieve my academic goals.

The guidance and research expertise of Dr. John Wilson, NASA Langley Research Center, has been critical to this dissertation. John Wilson, a distinguished physicist and project leader at NASA, has been generous in his willingness to assist me in applying theoretical concepts and principles to seek solutions for problems of concern to the scientific community. He has stretched my knowledge and capabilities in new directions. During the twenty years I have worked under his leadership, I have come to admire and respect the prodigious body of research done by Dr. Wilson and his staff for its depth and rigor. I appreciate the value of being a participant in those efforts.

I would also like to acknowledge the support of the NASA Langley Research Center grant which provided funding for this research through the ODU Research Foundation.

TABLE OF CONTENTS

LIST OF TABLES

LIST OF FIGURES

1. Introduction

This work is concerned with the transport of energetic nucleons through extended bulk matter.[1] The nucleons (i.e., protons, and neutrons) of interest to us are produced by, or part of, the flux of solar and galactic cosmic rays transiting the interplanetary region.[2–4] The applied physicist will find this problem to be of interest for two primary reasons. First, these processes constitute the most energetic interactions known in nature.[5] Cosmic Ray kinetic energies of 10^8 eV are common and some may reach 10^{20} eV. Therefore, depending on shield penetration depth, the entire range of elastic and nonelastic scattering phenomena in nuclear and atomic physics is involved in the transport process. Second, important health and technology issues related to space radiation require knowledge of transported particle fluences[6,7] (i.e., time-integrated flux). For example, predictions of human exposure during manned space missions or high altitude aircraft flights[8] require ionized particle fields for dose estimation.[9] In addition, space satellite circuit design relies on accurate models of phenomena such as single event-upset (SEU)[3,10] for reliability analysis. SEU refers to the process by which ionizing radiation creates a sufficient number of electron-hole pairs in a circuit to establish an electrical current which causes a change in the logic state of the device.

The National Aeronautics and Space Administration (NASA), as the name implies, has a research interest in the physics of radiation transport for both spacecraft and aircraft systems.[11,12] But NASA has a mission requirement which is central to the approach taken in the present work.[13,14] Transport models must be physically robust and computationally efficient.[15] "Computational efficiency," is required since space habitat and transportation system designs are evaluated for radiation protection in an interactive workstation environment. In order to be useful, the radiation analysis component must not require extensive computational resources.[16]

We will develop an analytical approach to the nucleon transport problem which allows for robust numerical implementation and rapid convergence of the relevant physical field quantities.[17] The analytical approach, as opposed to the conventional statistical modeling

based approach,[5,18] allows for direct application of the principles of mathematical physics to evaluate the physical effects of computational approximations.[1] But, prior to developing a cosmic ray transport model, we consider the known features of the cosmic ray environment.

Cosmic Radiation

The discovery of cosmic radiation resulted from questions arising from the study of electrical conductivity in gases around the beginning of this century.[2,3] Residual conductivity was discovered in gases which were supposed to exhibit dielectric properties. In 1912 Hess[19] conducted a series of balloon flights to an altitude of 5 km and was able to demonstrate that the current in an ion chamber increased with altitude. He established that the effect was independent of diurnal variations from which he concluded that a new penetrating radiation from outside the atmosphere was responsible. This discovery precipitated a great deal of balloon experimentation and many new discoveries during the next four decades. In 1933 Rossi used an array of Geiger-Muller detectors to exhibit the effect of particle multiplication during collisions. In 1937 Forbush observed worldwide decreases in cosmic ray intensity coincident with geomagnetic storms. In 1941 Schein, Jesse, and Wollan using balloon borne equipment, measured directly that the primary cosmic radiation consisted of protons. In 1948 Freier, Bradt, and Peters[19] found heavy nuclei components in the cosmic ray field.

With the advent of orbital space flight,[20] Van Allen and his coworkers, in 1958, used Geiger-Muller counters onboard Explorer satellites I and III to measure high count rates in confined regions beyond an altitude of about 1000 km due to trapped charged particles (the Van Allen radiation belts). In addition to the knowledge gained from balloons and[21] satellites have been added the contributions from accelerator based reaction crossection experiments[22–25] and advances in theoretical nuclear physics.[26–30] Today the interplanetary and near earth radiation environment is reasonably well understood. Briefly, some of the other findings of importance to our efforts include the existence of an inner and outer belt of trapped radiations[31–33] and also effects of the eleven year sunspot cycle.[4] The sunspot cycle modulates the solar wind affecting the magnetic shielding properties of the radiation belts.

The typical particle environment in space is shown in figure 1.[6] Low energy protons from the solar wind continuum are common but, as we shall see, are not sufficiently energetic to penetrate bulk matter. Neither is the 30 MeV proton radiation from solar storms but the solar flare radiation can be quite penetrating. Galactic cosmic rays feature heavy nuclei and very high kinetic energies per amu[34] but the fluences are small.[11,35–38] For astronaut shield design purposes the solar flares[13,39–41] are most important (fig. 2) as a determinant of early somatic injury but for interplanetary flight the long term exposure to heavy galactic cosmic rays,[6,42–44] especially Fe ions[45] (fig. 3), will be the limiting factor in long term missions. Figure 3 shows[46] the elemental abundance of cosmic rays up to iron nuclei. Protons and alpha particles constitute almost 99 percent of the heavy particles.[2] The primary proton spectra can be represented by a power law. The integral spectrum may then be written[3]

$$M(>E) = K(E + m_0c^2)^{-\gamma} \text{ particles cm}^{-2}\text{s}^{-1}\text{sr.}^{-1}$$

where K and γ are constants, and m_0c^2 is the proton rest mass energy. Protons and collision produced neutrons constitute the primary sources of transported radiation in space applications.[6]

Interaction Mechanisms

As high-energy space radiations traverse bulk matter objects, such as a spacecraft or high altitude aircraft (including the atmosphere), their radiation fields change composition through interactions with the materials in their paths.[1] As a result of these interactions, the internal radiation environment within the material can differ appreciably from the incident external environment.[2] These alterations in the incident radiation environment depend upon the thickness, geometry, and composition of the target material.[47,48] They are described by transport models which relate the transmitted flux, as a function of spatial location, kinetic energy, and direction of particle motion, to the incident flux.[5,49] The main interaction processes involved in the transport of these radiation fields through bulk matter are (1) ionization energy losses through collisions with atomic electrons,[50–65] (2) nuclear elastic and inelastic collisions,[6,14] and (3) nuclear breakup (fragmentation)[66–68]

Space Radiation Environment

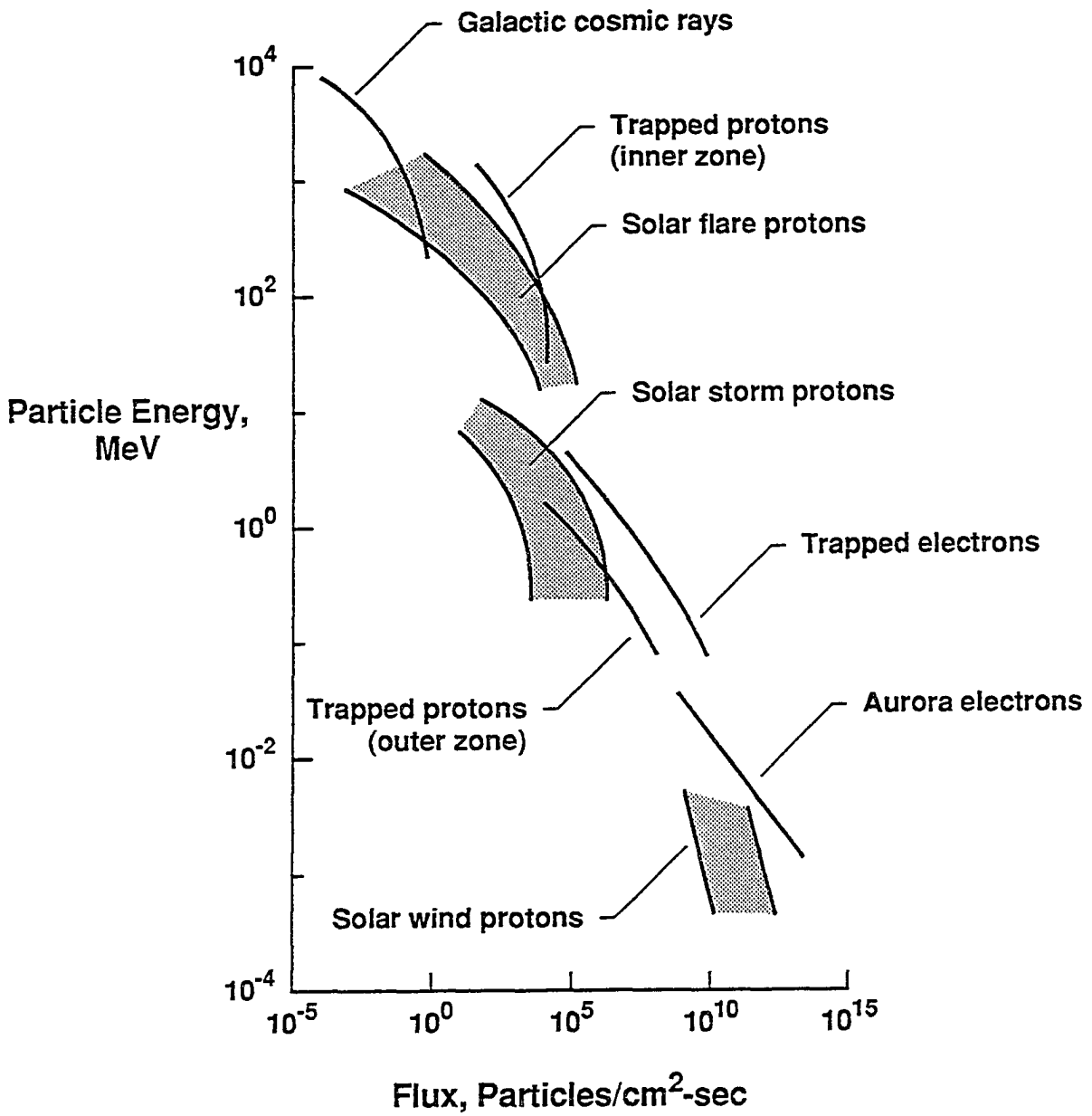

Fig. 1 Cosmic Ray Spectra in Near Earth Environment

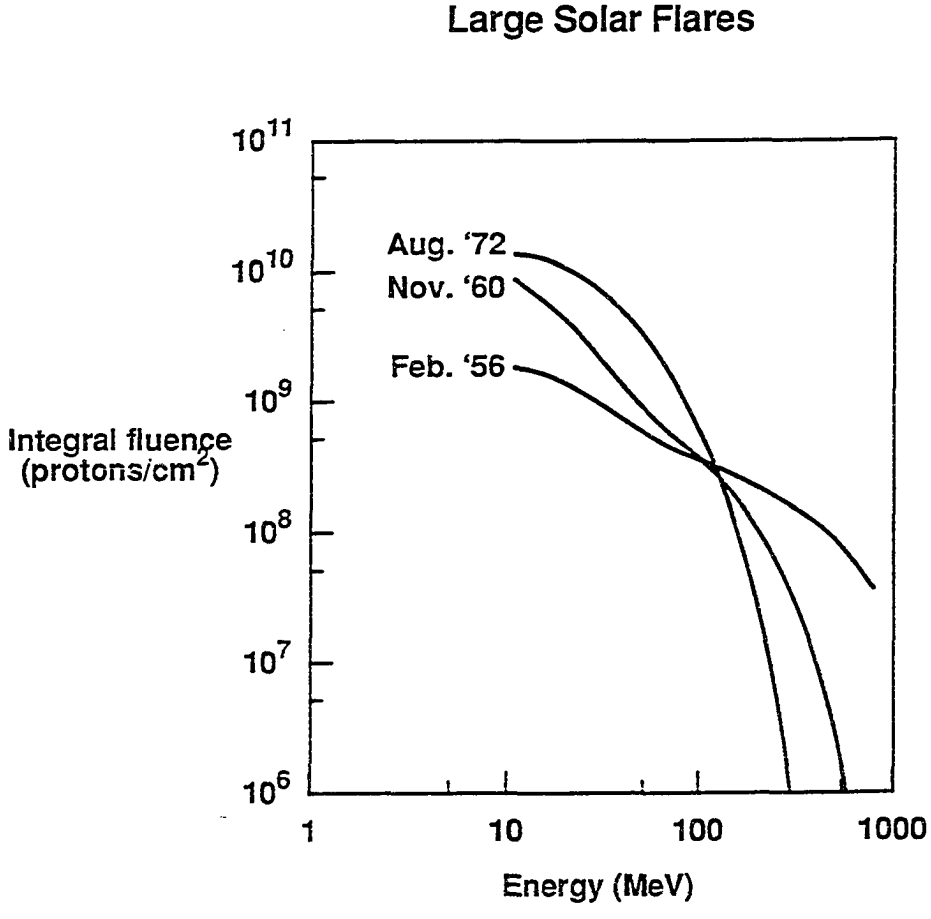

Fig. 2 Typical Spectra for Large Solar Flares

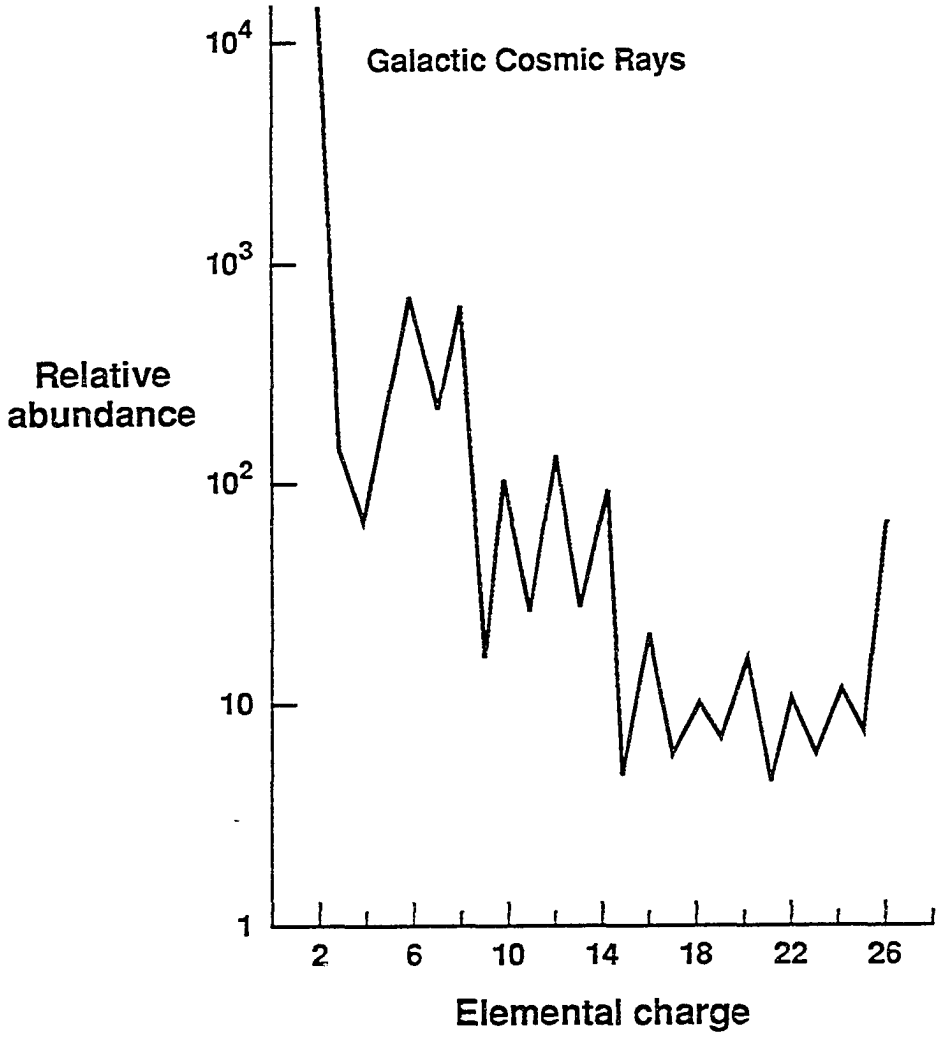

Fig. 3 Galactic Cosmic Ray Abundance

and electromagnetic dissociation interactions. The latter are particularly important because fragmentations result in the production of reaction products which alter the isotopic composition of the transported radiation fields. The radioactive decay contributions of the transported fragments are ignored because their decay times are typically much longer than the time required for the radioactive fragment to exit the spacecraft or undergo a subsequent nuclear collision.[11]

The dominant term in a shielding calculation is energy loss through ionization;[18] that is a collision between an incoming charged particle and the orbital electrons of the shield material. This coulomb interaction will cause the target atom to either be raised to an excited state or become ionized by ejecting an electron. Each collision will decrease the projectile kinetic energy by a small amount and eventually cause it to stop. This distance is called the 'range'. Figure 4 shows proton range as a function of initial kinetic energy for various shield materials. Note that the distance coordinate has the units of areal density. This scaling is common for comparing widely varying shield densities. Figure 4 reveals[18] that the <30 MeV solar storm protons from figure 1 have a range in tissue of <1 gm cm^{-2}. For our purposes penetrating protons require a kinetic energy >50 MeV. Because these interactions involve a high number of small energy exchange collisions along this path it is useful to develop a continuous slowing down approximation (cdsa) to describe the process. Bethe derived an expression for the "stopping power" or $\frac{dE}{dx}$ using the quantum mechanical Born approximation.[58] A detailed derivation of the Bethe expression for stopping power was previously fully reviewed by Lamkin[1] and is not repeated herein. Figure 5 shows[18] the proton stopping power for protons in various materials. Low energy protons exhibit very rapid slowing but stopping power decreases as the kinetic energy rises due to an inverse dependence on the square of proton velocity. Above one GeV the stopping power is roughly constant. Figure 6, however, shows[1] that stopping power eventually increases again due to relativistic increases in the proton's perpendicular field by a factor of $\frac{1}{\sqrt{1-\beta^2}}$. The increase is

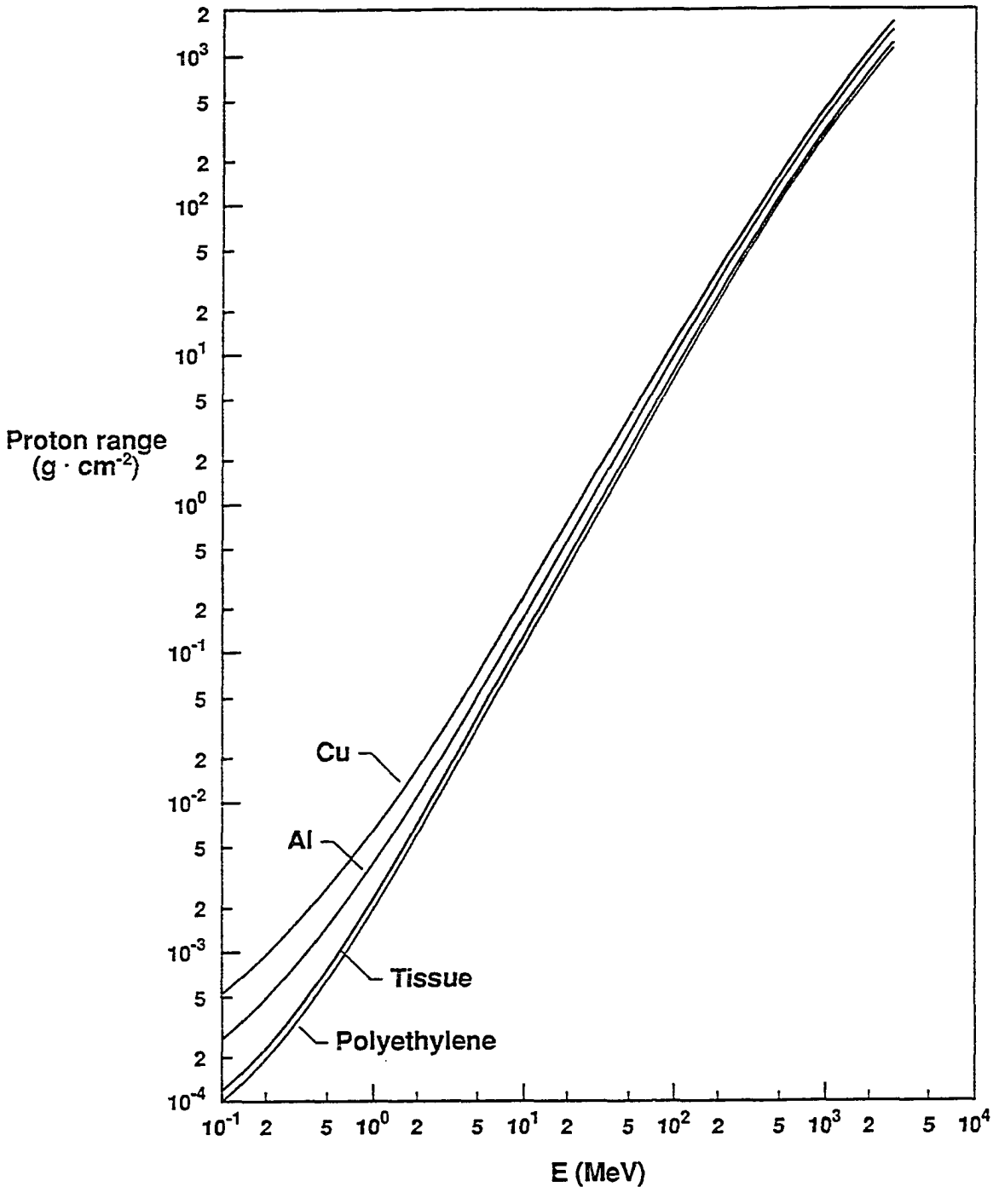

Fig. 4 Proton range vs energy in various materials

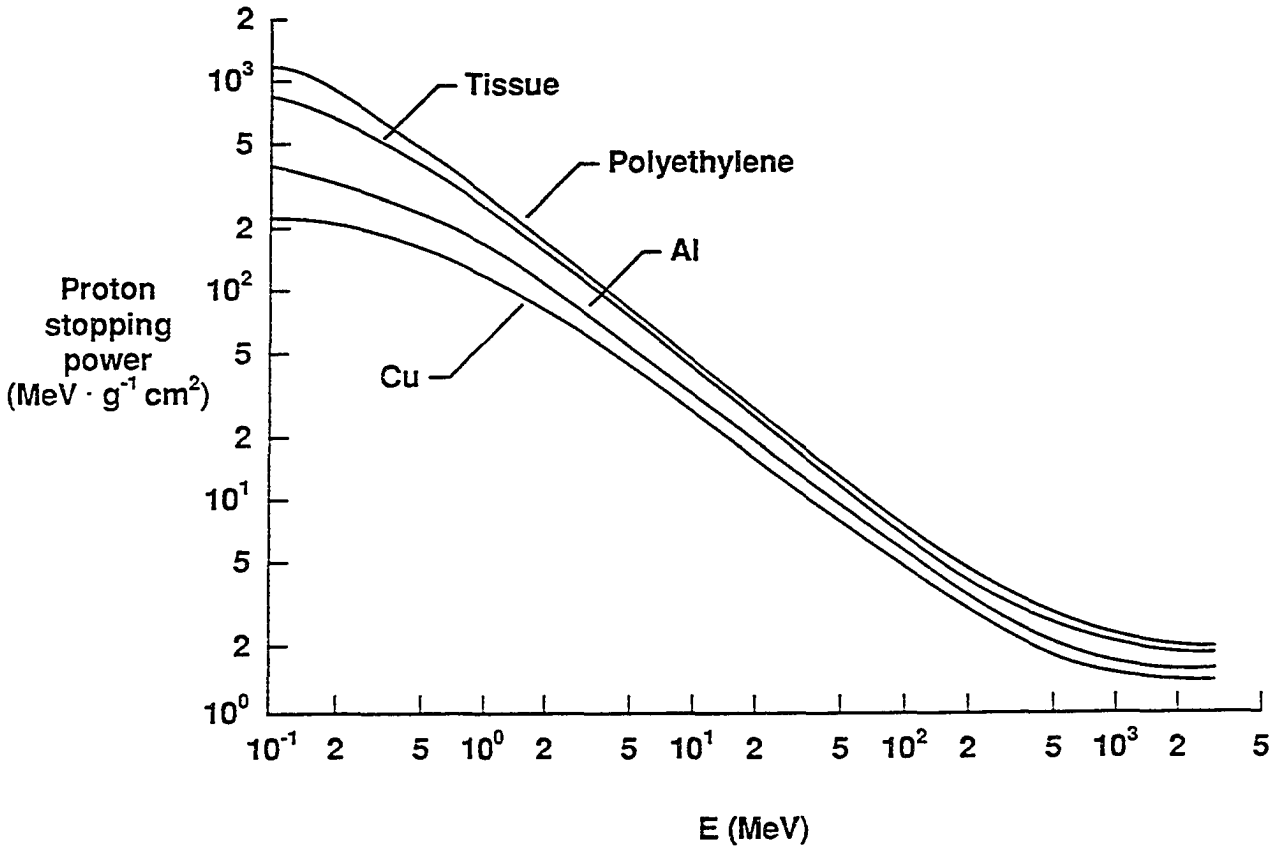

Fig. 5 Proton stopping power vs energy in various materials

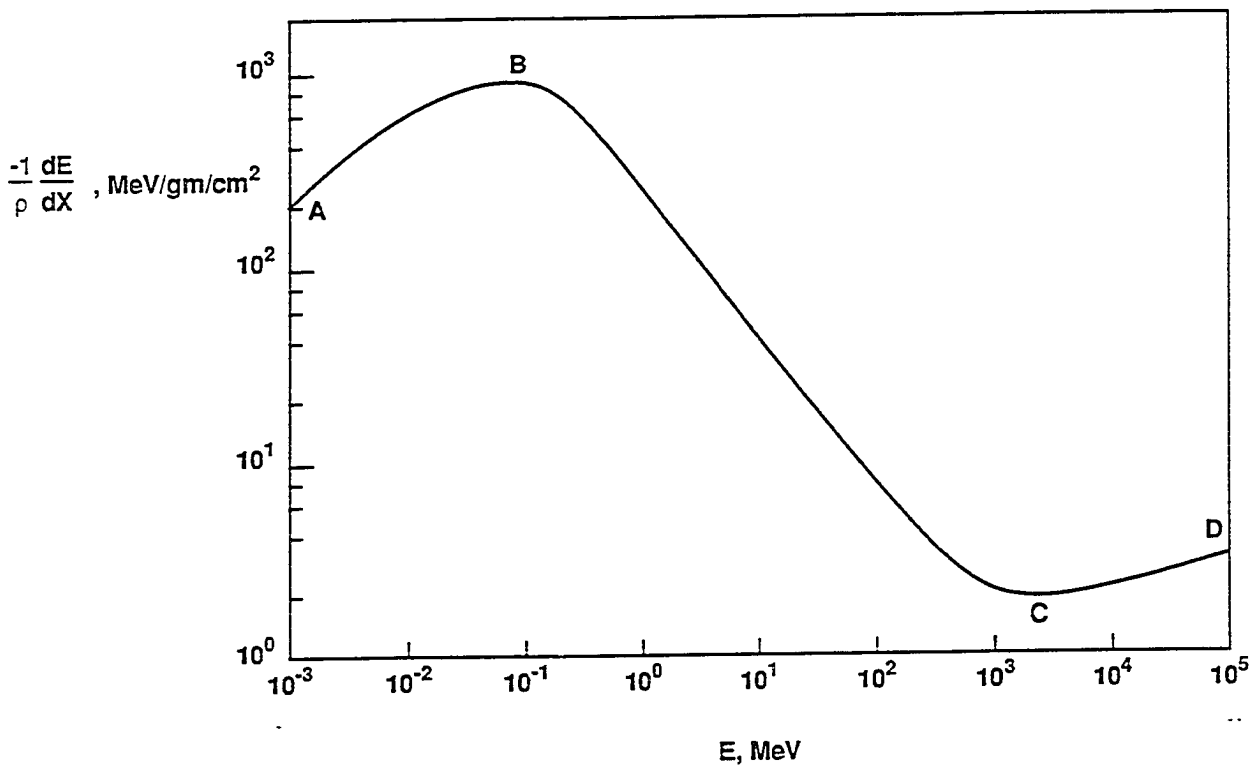

Fig. 6 Stopping power as a function of energy for protons in water

counteracted somewhat because large kinetic energy increases result in small velocity changes and because of the "screening" effect due to polarization.

A great deal of research has been devoted to the ionization process and, today, very complex models exist to represent the cdsa. This is due, both, to the relatively sophisticated state of theoretical quantum mechanical knowledge of atomic physics and to the technological motivation to correctly model the process. The treatment of stopping power can be considered to be rigorous when compared to models for nuclear fragmentation, the other critical interaction process in high energy baryon transport.

The nuclear interactions which take place between energetic baryons and bulk material constituents are quite different in character from the ionization process. The nuclear mean free path is typically on the order of several cm[69] and the corresponding crossections are about eight orders of magnitude smaller than for interactions with atomic electrons.[1] A 100 MeV proton in tissue, for example, has an ionization stopping range of 7.57 cm[58] and a nuclear mean free path of about 55 cm.[69] Figure 7 shows[18] the macroscopic nuclear cross section for protons in various materials. We see that the curve shapes are similar for a variety of common spacecraft materials. For a given material the crossection varies by no more than 10% for proton energies above 10 MeV, justifying the use of a constant crossection for analytical modeling purposes. The rarity of nuclear collisions is an important distinction when compared to ionization but the process is also quite different.

Hadrons can interact strongly with a target nucleus. One possible outcome[34,70–74] for energetic projectiles is the emission of target constituents with kinetic energies on the same order as the incident energy.[21] This process is called nuclear fragmentation. For nucleon scattering the most common result is the emission of additional nucleons. These 'knockout' particles tend to scatter in the highly-forward direction, so the incident 'primary' flux of nucleons at the boundary can create 'secondary' particles[1,15] as the beam penetrates the material. These secondary particles can also produce new particles through subsequent fragmentation interactions.[11] So, even though the proton component of the primary flux

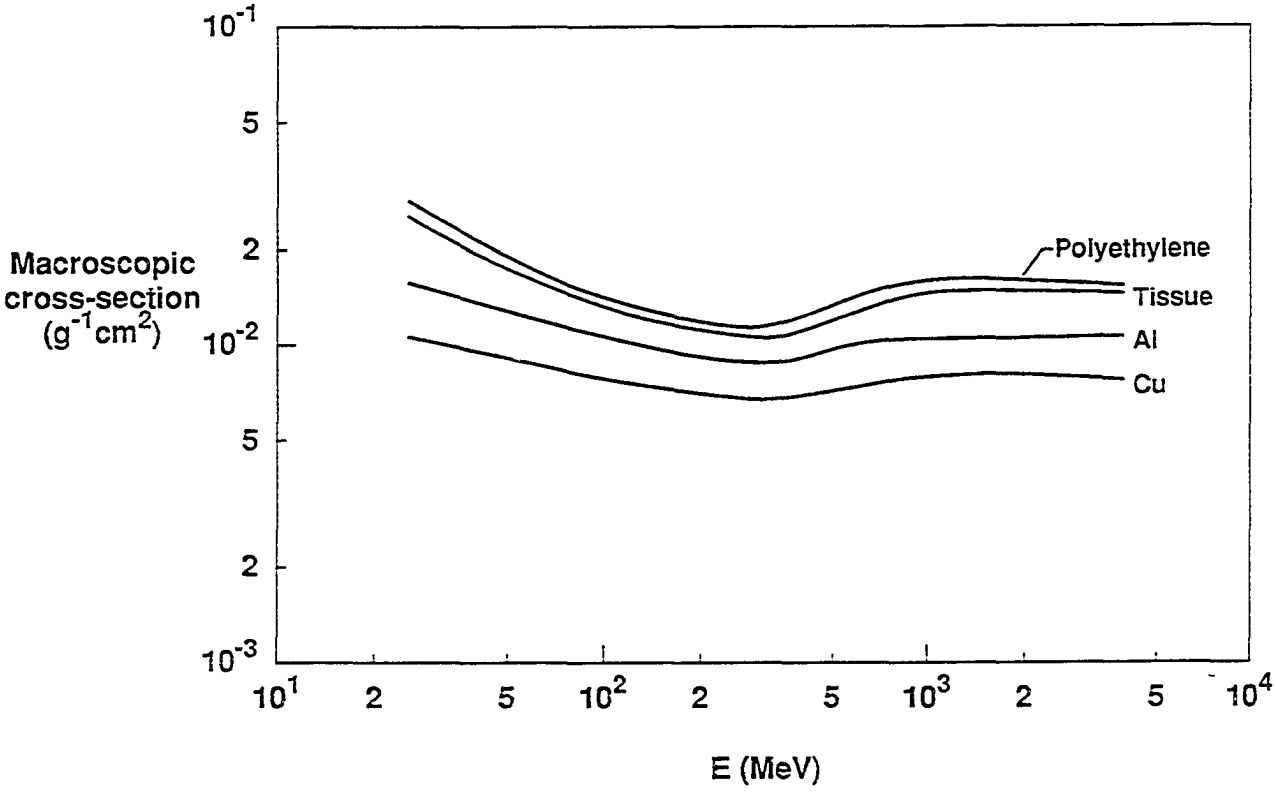

Fig. 7 Primary proton macroscopic nuclear-collision cross section vs energy in various materials

quickly disappears, the neutrons and secondary protons can sustain the overall fluence for deep penetrations.[75] The fragmentation process involves energy transfers of several MeV as opposed to the several eV transfers characteristic of atomic ionization.[66]

The commonly used models for nucleon-nucleus fragmentation in space transport are basically classical and typically involve considerable empiricism.[60,68] The typical interaction picture has the nucleon entering the nucleus (depicted as a Fermi sea) and interacting with a single nucleon or clusters (e.g., Alpha particle) of nucleons.[70,71] The models typically allow for 'multiple scattering'[71] in which one of the scattered nucleons is able to re-scatter with one or more of the target constituents before exiting the nucleus. Sophisticated models based on the Monte Carlo statistical approach have been developed to represent fragmentation.[5,76,77] These models incorporate nuclear data from experiments such as electron-nucleus scattering and nucleon-nucleon scattering to determine the probability of particular knockout processes. Monte Carlo models for nuclear fragmentation are discussed further in Chapter 5. One simple analytical form for fragmentation scattering which provides a functional expression for the production term is the 'quasi-elastic' approximation.[15] In the quasi-elastic picture the projectile nucleon interacts with a single target nucleon which is assumed to be uncoupled from the rest of the nucleus. The quasi-elastic formulation is a function of only the energy difference between the incident particle and the scattered energy of the target nucleon. Because of its functional simplicity and physical applicability, the quasi-elastic form is used for space transport benchmark cases (see Chapter 3).

The residual target nucleus is, of course, left in an excited state following the knockout but its relaxation time for de-excitation and recoil is long compared to the prompt fragmentation process. So the residual nucleus can be treated separately using, for example, an 'evaporation' model.[6] The model looks at the difference in binding energy between the original nucleus and the residual constituents and performs a stepping procedure to dexcite the nucleus. Nucleons are ejected from the nucleus one at a time, or in clusters, until a stable configuration is reached. This scattering is isotropic and the energies are too low to

allow for propagation very far from the vicinity of the nucleus. The evaporation nucleons are, therefore, not added to the transported flux but must be considered in dose calculations (see Appendix C).

We now see a picture of the nucleon transport process in bulk matter. The ionization process removes protons from the beam by the cdsa. Some nucleons are removed by nuclear collisions but may, in turn, add nucleons back in the propagated flux by the fragmentation process. The overall flux will die out at some penetration depth. Our goal is to develop a mathematical expression for the process of loss and gain. We will develop an analytical approach based on the integro-differential Boltzmann equation. This approach will be applied to problems of interest to the manned space effort.

Transport Models

Even before the inception of the manned space program it was recognized that the cosmic ray environment might produce early somatic effects[78] through the ionization and fragmentation processes described above. By early somatic effects we mean radiation induced sickness as opposed to increased long term cancer risks. The primary concern was solar flare radiation. A major thrust in the development of space radiation methods for solar flare and geomagnetically trapped protons resulted in the development of a series of Monte Carlo Codes by Alsmiller's[18] group at the the Oak Ridge National Laboratory (ORNL). The chronology of these codes is the Nucleon Transport Code[79] (NTC), then the Nucleon-Meson Transport Code[80] (NMTC) and finally the high Energy Transport Code[81] (HETC). Although the HETC, and its subsequent derivatives[2] represent the most tested and documented code of this type and was initially stimulated by the needs of the space program, the codes have had little use in space engineering applications due to program complexity and high computational resource requirements. Even though code restructing[82] and alternate handling of the nuclear database greatly improved computer efficiency, the ultimate limitation was inherent to the Monte Carlo method itself. To understand these limitations we have to examine the Monte Carlo procedure.

The Monte Carlo method represents one of the most successful scientific numerical modeling approaches developed for digital computers.[83] It has two primary advantages. The basic method uses a simple statistical decision scheme to model the physical processes and it is able to handle complex three-dimensional (3-D) problems. The Monte Carlo method has been successfully applied to such diverse physical applications as crystal growth, DNA structure, heat transfer, non Newtonian flows, thermo-nuclear explosions, circuit design, and reactor kinetics. We can illustrate the basic method by using the case of high energy neutron transport through bulk matter. Neutrons are transported, one at a time, from the boundary into the target material. At some penetration depth the code determines, based on a probability analysis, that a collision has occurred with a target nucleus. It then uses a statistical nucleon-nucleus interaction model to produce fragmentation products or elastically rescattered neutrons. Each of the fragmentation products, if any, are transported until each remaining secondary is exhausted or the out-going boundary is reached. The code maintains a 'history' file of these events for post-processing. The code then transports another neutron into the material. The idea is to transport enough primaries through the target material to develop a 'statistical ensemble' of events which represents a physically meaningful picture of the process. The success of the Monte Carlo[2] is based on this idea that a few thousand particle transport events provide convergence for a real world picture involving between 10^9 and 10^{11} incident neutrons. The relative simplicity of the basic Monte Carlo kernel belies the programming complexity involved in the book keeping requirements for the particle histories, the difficulties of data postprocessing, the myriad decisions imposed by the code designer onto the physics, and the long processing times required to reach convergence. These difficulties lead to examination of alternative analytical approaches to model the transport.

The problem with the analytical approach, of course, is that 3-D effects quickly lead to intensive computational requirements.[18] To solve the spatial and energy integrals for particle transport at arbitrary scattering angles requires storage and run times which are not feasible. Most work using analytical approaches has concentrated on the one-dimensional

(1-D) transport regime. In 1958 Peters[19] used a 1-D equilibrium solution ignoring ionization energy loss and radioactive decay to show that the light ions of the galactic cosmic rays have their origin in the breakup of heavy nuclei. At about the same time other researchers including Schaeffer,[84] Foelsche[84a], and Dye and Noyes[20] were conducting space proton studies. Their work ignored nuclear reaction and treated only the ionization energy loss. These studies were hindered by the lack of nuclear data. The development of the intranuclear cascade model by Goldberger[27] and numerical work by Metropolis[83] led to significant developments[85] in analytic and statistical transport modeling during the 1960's. Gloeckler and Jockipii[86] developed a Volterra equation solution to first order in the fragmentation ignoring ionization loss. Lezniak[87] derived a Volterra equation including energy loss which he referred to as a solution "only in the iterative sense" and evaluated only the unperturbed term. In 1974 Allkofer and Heinrich[38] used an energy multigroup method in which an energy independent fragment transport approximation was applied within each energy group after which the energy group boundaries were moved according to continuous slowing down theory ($-dE/dx$). Chatterjee, Tobias, and Lyman[74] solved the energy-independent fragment transport equation with primary collision density as a source and neglected higher order fragmentation. In fact most cosmic ray physicists have found the first fragmentation term to be sufficient since the path lengths in interstellar space are 3 to 4 g/cm^2.

Wilson and Lamkin[11] were interested in the Monte Carlo results of Alsmiller which indicated that energetic nucleon transport was confined to highly forward fragmentation scattering to penetration depths (in tissue) of 20 g/cm^2. They also knew that ionization loss and elastic scattering events were kinematically limited to forward scattering. In 1974 Lamkin,[1] and Wilson and Lamkin[11] developed a theory for high energy coupled nucleon transport in 1-D based on the successful analytic inversion of the Boltzmann transport operator and a numerical procedure for the resulting Volterra equation. In his Master's Thesis Lamkin[1] developed a perturbation approach for high energy nucleon transport. The major physical insight from this work was that the transport process could be described

by succeeding generations of secondary radiations produced from an initial primary beam. This provided, as opposed to the Monte Carlo method, a physically motivated approach to determining the convergence of the numerical scheme to the exact solution. It also provided significantly improved accuracy for deep shield penetration cases compared to prior analytic results.

The successful application of this analytical Boltzmann approach to space radiation transport was limited by lack of a mature nuclear reaction database. Further improvements to the transport procedure were not indicated until a realistic database became available. Between 1974 and 1988 numerous enhancements[6] were made to the NASA Langley Research Center database due to additional nuclear crossection experiments and improved fitting procedures to Monte Carlo based interaction models.

In this dissertation we describe improvements to the analytical Boltzmann transport method which essentially completes the process begun in 1974.[1] We develop a computationally efficient numerical marching procedure to replace the step-by-step perturbation series method for secondary generation transport. "Marching" is a process by which the known solution at a boundary position x_0 is used to obtain the solution at $x_0 + \Delta x$. The solution at $x_0 + \Delta x$ is used as the new boundary to obtain the solution at $x_0 + 2\Delta x$, etc. We tune the procedure to allow for the minimum numerical operation count to insure second order accuracy in the overall truncation error.[15] This is accomplished by the development of a set of analytical benchmark cases. One set features an incident particle flux with a continuous energy distribution characteristic of space radiation. The other set features a monoenergetic incident spectrum characteristic of particle accelerator environments. The exact benchmark solutions are compared with the numerical procedure to provide an expression for the truncation error which can then be minimized by an optimization process. We also develop a model to describe the elastic rescattering of neutrons. The model is relatively independent of energy grid mesh density. Elastic scattering is kinematically limited to small energy

transfers and the coarse grids designed to resolve the fragmentation process cannot generate the rescattered neutrons.

These improvements to the transport model, along with enhancements of the nuclear reaction data base, provide for a complete coupled nucleon transport code to handle cosmic rays.[10,88] The model does not include pion production which becomes important at nucleon kinetic energies exceeding 400 MeV.[13] Pion transport is not significant for the energy ranges and penetration depths typical of space flight.[15] The remainder of this work is organized as follows:

In Chapter 2 we sketch a derivation of the Boltzmann equation for nucleon transport and relate all of its terms to the physical processes of gains and losses due to atomic ionization and nuclear fragmentation. We solve the Boltzmann equation using a characteristics mapping to handle difficulties due to the presence of the stopping power term. We develop an expression for coupled nucleon transport as a Volterra equation of the second kind. We discuss the previous work of Lamkin which implemented the Boltzmann solution as a perturbation series in which successive order terms are directly related to physical secondary generations of particle.

In Chapter 3 we consider the coupled Boltzmann solution for an exactly solvable benchmark case in which the incident nucleon flux features a continuous energy distribution. This case is typical for cosmic ray transport.

In Chapter 4 we develop a strategy for the numerical implementation of the Volterra equation using a marching procedure. We discuss the improvements of this approach over the implementation of the perturbation series method. We then use the exact benchmark case from Chapter 3 to minimize the second order truncation error of the marching scheme. This is accomplished by exactly solving the approximated form of the particle integral. This solution uses the same functional forms for boundary flux and production spectra as the exact continuous benchmark. The difference between the exact and approximate forms displays the truncation error of the numerical method. An optimization method is

employed to minimize the second order truncation error. The error is tuned by replacing certain integration variables with constants which are expressed as fractional values of the integration step size.

In Chapter 5 the numerical marching scheme for nucleon transport is incorporated in the BRYNTRN[13] computer program. BRYNTRN (Baryon Transport) represents one of the products of a collaboration between the NASA Langley Research Center and the Radiation Physics group of Old Dominion University during the past 25 years. BRYNTRN provides a sophisticated nuclear reaction database and models for atomic ionization. These support modules provide a realistic physical basis for evaluating our transport methodology. The method is applied to a typical spacecraft radiation case using varying thickness' Aluminum slab shielding followed by tissue media. The effect of step size and order of truncation error on the dose and fluence is examined for various shield thickness' out to 100 g/cm^2. The physics of the shield-tissue interface region is studied. The absorbed dose displays a 'shoulder' effect for deeper penetration cases. This is shown to be related to the process of re-establishment of flux equilibrium as the transported flux enters a new target medium. The BRYNTRN code is compared with HETC Monte Carlo benchmarks. Very good agreement is obtained for the 20 g/cm^2 benchmark test case.

In Appendix A we develop a benchmark for the mono-energetic case. Results are shown for 100 MeV protons incident on water.

In Appendix B we study the problem of neutron elastic scattering. The energy grid resolution suited to nuclear fragmentation is shown to be too coarse to resolve the small energy transfers associated with elastic scattering. Adequate resolution grids are shown to require unreasonably high computing resources. A model is developed for neutron elastic scattering which conserves particles and is relatively insensitive to grid resolution. The physics of the model is based on an analysis which shows the elastically scattered flux at some given penetration depth x is related to the flux at $x - h$ but energy shifted by an h

dependent term. The model is applied to various targets including light and heavy elements. Numerical experiments are performed to study the physical characteristics of the model.

In Appendix C we discuss the flux of the target fragmentation products which are important to the calculation of the local dose.

2. Transport Physics—The Boltzmann Equation

2.1. Derivation of the Boltzmann Equation

In this section we sketch the derivation of the Boltzmann equation. Our purpose is twofold. First, it is the most efficient way to acquaint the reader with the physical elements of the transport process. Second, we wish to show that nucleon transport is simply a special case of the classical theory of the kinetic theory of gases. Our approach is based on conservation principles developed previously by Lamkin[1] and Wilson and Lamkin[11] but employs a more rigorous methodology.[6]

An expression for the transport of high energy nucleons may be developed from first principles by using the ideas from the kinetic theory of gases. Kinetic theory is widely used to explain phenomena in statistical mechanics,[89] plasma physics,[90] and fluid dynamics.[91] Indeed, the Navier-Stokes equations describing fluid motion are moments of the Boltzmann transport equation from single species kinetic theory. Phenomena such as shearing fluid motions,[75] low energy reactor neutron kinetics,[92] and high energy ion transport[1] can all be developed as appropriate approximations to the scattering processes that are described by Boltzmann theory. Consider an element of phase space described by a distribution function[89,90] f where $f(\vec{r},\vec{v},t)\,dv_x\,dv_y\,dv_z \equiv$ no. particles per unit volume at position $\vec{r}$, and time t, with velocity components between $\vec{v}$ and $\vec{v}+d\vec{v}$.

The number density is given by

$$n(\vec{r},t)=\int_{-\infty}^{\infty} dv_x \int_{-\infty}^{\infty} dv_y \int_{-\infty}^{\infty} dv_z f(\vec{r},\vec{v},t) \tag{2.1.1}$$

Typically we normalize f by using a probability distributions function $\hat{f}$ so that

$$\int_{-\infty}^{\infty} \hat{f}(\vec{r},\vec{v},t)d\vec{v}=1 \tag{2.1.2}$$

and

$$f(\vec{r},\vec{v},t)=n(\vec{r},t)\ \hat{f}(\vec{r},\vec{v},t) \tag{2.1.3}$$

In statistical mechanics the kinetic theory is developed further using specified functional forms for the probability distribution. But we can stay with $f(\vec{r},\vec{v},t)$ and write its total time derivative

$$\frac{df}{dt}=\frac{\partial f}{\partial t}+\frac{\partial f}{\partial x}\frac{dx}{dt}+\frac{\partial f}{\partial y}\frac{dy}{dt}+\frac{\partial f}{\partial z}\frac{dz}{dt}$$
$$+\frac{\partial f}{\partial v_x}\frac{dv_x}{dt}+\frac{\partial f}{\partial v_y}\frac{dv_y}{dt}+\frac{\partial f}{\partial v_z}\frac{dv_t}{dt} \tag{2.1.4}$$

This is seen to consist of a convective term

$$\frac{\partial f}{\partial t}+\vec{v}\cdot\nabla f$$

and a force term

$$\frac{\tilde{F}}{m}=\frac{d\vec{v}}{dt}$$

The Boltzmann equation is then written as

$$\frac{\partial f}{\partial t}+\vec{v}\cdot\nabla f+\frac{\tilde{F}}{m}\cdot\frac{\partial f}{\partial\vec{v}}=D_c f \tag{2.1.5}$$

where D_c is a Collision operator producing sources and sinks for f. A typical example of the application of the form of the Boltzmann equation is seen in the "Vlasov" equation for the case of a plasma that is sufficiently hot and tenuous to neglect collisions.[90] Then

$$\frac{\partial f}{\partial t}+\vec{v}\cdot\nabla f+\frac{q}{m}(\vec{E}+\vec{v}\times\vec{B})\cdot\frac{\partial f}{\partial\vec{v}}=0 \tag{2.1.6}$$

where, of course, q, E, and $\vec{B}$ represent charge, electric field, and magnetic induction.

In applying equation (2.1.5) to high energy nucleon transport we can ignore any effects involving the external body force $\tilde{F}$ and solve the equation due to sources at the boundary. The energy loss rate in condensed matter is $>10^{10}$ MeV/sec so that the charged particles come to rest in a small fraction of a second. Therefore, the density function is in equilibrium with the boundary sources. Our applications will assume a stationary incident fluence so that a steady state equilibrium condition is established within the shield material. In addition,any motion of target atoms due to externally applied forces is insignificant on the time scale of

a transiting nucleon. We are left with

$$\vec{v} \cdot \nabla f = D_c f \tag{2.1.7}$$

Since our problem is physically related to fluences of projectiles into a stationary target material we recast equation (2.1.7) by defining a directional particle flux density[93]

$$\phi(\vec{r}, E, \vec{\Omega}) = v f(\vec{r}, v, \vec{\Omega}) \frac{dv}{dE} \tag{2.1.8}$$

where $\vec{v} = v\vec{\Omega}$ and $\vec{\Omega} \cdot \vec{\Omega} = 1$. Then equation (2.1.7) becomes

$$\vec{\Omega} \cdot \nabla \phi(\vec{\Omega}, E, \vec{r}) = D_c \phi(\vec{\Omega}, E, \vec{r}) \tag{2.1.9}$$

the physical processes which determine $D_c\phi$ include elastic and nonelastic scattering from target nuclei and electromagnetic interactions between charged projectiles and the bound target media electrons.

$$D_c \phi = \text{gains} - \text{losses} \tag{2.1.10}$$

The gains and losses in equation (2.1.10) may be determined by the application of conservation principles[6] to the projectile fluence in an element of target media shown in figure 8 as a sphere of radius δ. Consider the flux component due to particles of type j and energy E entering through an element of area at $\vec{x} - \delta\vec{\Omega}$ in direction $\vec{\Omega}$ and leaving the sphere at $\vec{x} + \delta\vec{\Omega}$ in direction $\vec{\Omega}$. This defines a flux tube through which would pass a number of particles of type j equal to $\phi_j(\vec{x} - \delta\vec{\Omega}, \vec{\Omega}, E)\delta^2 d\vec{\Omega}$ if the propagation was taking place in a vacuum. But the two numbers of particles actually differ by the gains and losses.[11]

$$\begin{aligned}
\phi_j(\vec{x} + \delta\vec{\Omega}, \vec{\Omega}, E)\delta^2 d\vec{\Omega} = {} & \phi_j(\vec{x} - \delta\vec{\Omega}, \vec{\Omega}, E)\delta^2 d\vec{\Omega} \\
& + \delta^2 d\Omega \int_{-\delta}^{\delta} d\ell \sum_k \int \sigma_{jk}(\vec{\Omega}, \vec{\Omega}', E, E') \\
& \times \phi_k(\vec{x} + \ell\vec{\Omega}, \vec{\Omega}', E')\, d\vec{\Omega}' dE' \\
& - \delta^2 d\vec{\Omega} \int_{-\delta}^{\delta} d\ell\, \sigma_j(E)\phi(\vec{x} + \ell\vec{\Omega}, \vec{\Omega}, E)
\end{aligned} \tag{2.1.11}$$

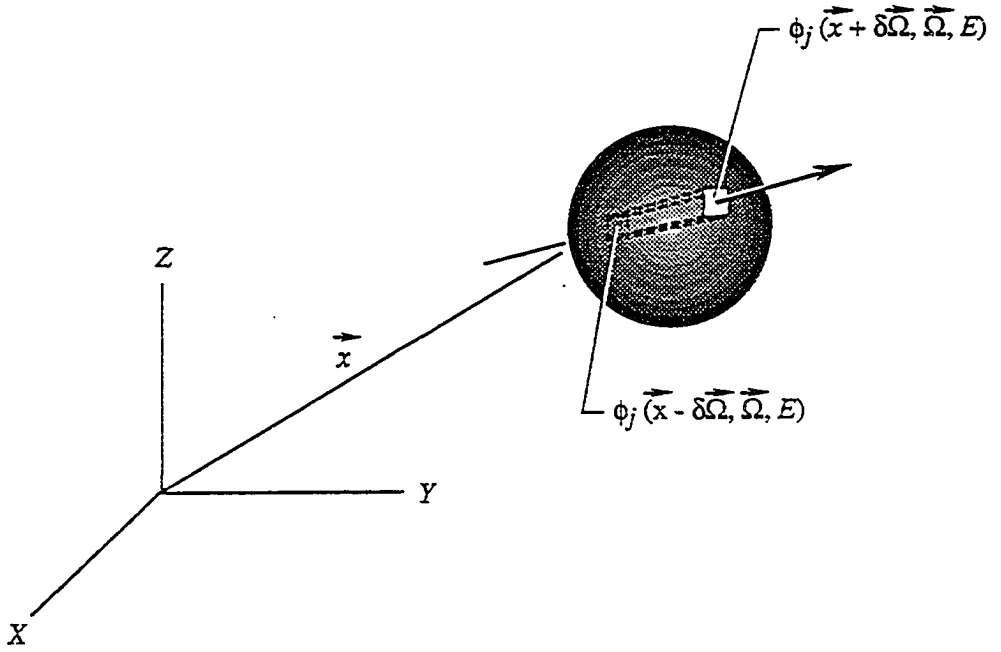

Figure 8 Transport of particles through spherical region

where $\sigma_j(E)$ and $\sigma_{jk}(\vec{\Omega},\vec{\Omega}',E,E')$ are the media macroscopic crossections. The cross-section $\sigma_{jk}(\vec{\Omega},\vec{\Omega}',E,E)$ represents all of those processes by which a particle of type k moving in the direction $\vec{\Omega}'$ with energy E' produces a type j particle in direction $\vec{\Omega}$ and energy E. The σ_{jk} term provides all sources of "secondary" generations of particles of type j and the σ_j term denotes all of losses of type j particles due to interaction with target nuclei. Expanding equation (2.1.11) in a Taylor series about $\vec{x}$ and retaining terms to order δ^3

$$\begin{aligned}\delta^2 d\vec{\Omega}[\phi_j(\vec{x},\vec{\Omega},E)+\delta\vec{\Omega}\cdot\nabla\phi_j(\vec{x},\vec{\Omega},E)] \\ &= \delta^2 d\vec{\Omega}\Big[\phi_j(\vec{x},\vec{\Omega},E)-\delta\vec{\Omega}\cdot\nabla\phi_j(\vec{x},\vec{\Omega},\vec{E}) \\ &+ 2\delta\sum_k\int\sigma_{jk}(\vec{\Omega},\vec{\Omega}',E,E')\phi_k(\vec{x},\vec{\Omega}',E')d\vec{\Omega}'\,dE' \\ &- 2\delta\sigma_j(E)\phi_j(\vec{x},\vec{\Omega},E)\Big] \qquad (2.1.12)\end{aligned}$$

Dividing equation (2.1.12) by $2\delta(\delta^2 d\hat{\Omega})$ and collecting terms gives

$$\begin{aligned}\vec{\Omega}\cdot\nabla\phi_j(\vec{x},\vec{\Omega},E) = \sum_k\int\sigma_{jk}(\vec{\Omega},\vec{\Omega},E,E') \\ &\times\phi_k(\vec{x},\vec{\Omega}',E')d\vec{\Omega}'\,dE' \\ &-\sigma_j(E)\phi_j(x,\vec{\Omega},E) \qquad (2.1.13)\end{aligned}$$

Comparison with equation (2.1.7) shows that equation (2.1.13) accounts for interactions with target nuclei.

Atomic interactions will result in both gains and losses for $\phi_j(x,\vec{\Omega},E)$. Charged particles entering the region with energy E will exit with some energy $E-\Delta E$ and thus constitute a loss. Particles entering with energy $E'>E$ may, depending on the crossections, exit with energy $E'-\Delta E=E$ and this contribute a gain. We write the atomic crossection as

$$\sigma_j^{at}(E,E') = \sum_n \sigma_{jn}^{at}(E+\mathcal{E}_n)\delta(E+\mathcal{E}_n-E') \qquad (2.1.14)$$

where n labels the electronic excitation levels and $\mathcal{E}_n$ are the corresponding excitation energies. Typical values for $\mathcal{E}_n$ range from 1–100 eV so that $\mathcal{E}_n \ll E$.

Define the total atomic crossection as

$$\sigma_j^{at}(E) \equiv \sum_n \sigma_{jn}^{at}(E) \tag{2.1.15}$$

and the stopping power as

$$S_j(E) \equiv \sum_n \sigma_{jn}^{at}(E)\mathcal{E}_n \tag{2.1.16}$$

then for atomic collisions

$$\begin{aligned}\text{gain—losses} &= \sum_n \sigma_{jn}^{at}(E+\mathcal{E}_n)\ \phi_j(\vec{x},\vec{\Omega},E+\mathcal{E}_n) \\ &\quad - \sigma_j^{at}(E)\phi_j(\vec{x},\vec{\Omega},E) \\ &\approx \sum_n \sigma_{jn}^{at}(E)\phi_j(\vec{x},\vec{\Omega},E) + \sum_n \mathcal{E}_n \frac{\partial}{\partial E}\ \sigma_{jn}^{at}(E)\phi_j(\vec{x},\vec{\Omega},E) \\ &\quad - \sigma_j^{at}(E)\phi_j(\vec{x},\vec{\Omega},E) \\ &= \frac{\partial}{\partial E}\left[S_j(E)\phi_j(x,\vec{\Omega},E)\right]\end{aligned} \tag{2.1.17}$$

Using equations (2.1.13) and (2.1.17) we can write equation (2.1.7) as

$$\begin{aligned}\vec{\Omega}\cdot\nabla\phi_j(\vec{x},\vec{\Omega},E) - \frac{\partial}{\partial E}\left[S_j(E)\phi_j(\vec{x},\vec{\Omega},E)\right] \\ + \sigma_j(E)\phi_j(\vec{x},\vec{\Omega},E) = \sum_k \int \sigma_{jk}(\vec{\Omega},\vec{\Omega}',E,E') \\ \times \phi_k(\vec{x},\vec{\Omega}',E')d\vec{\Omega}'dE'\end{aligned} \tag{2.1.18}$$

Equation (2.1.18) provides the form of the Boltzmann equation normally used in high energy nucleon transport.[11] We will employ the "straight ahead"[5,17,94,95] approximation to write

$$\begin{aligned}\left[\frac{\partial}{\partial x} - \frac{\partial}{\partial E}S_j(E) + \sigma_j(E)\right]\phi_j(x,E) \\ = \sum_k \int F_{jk}(E,E')\phi_k(\vec{x},E')dE'\end{aligned} \tag{2.1.19}$$

where the secondary production spectra F_{ji} has the same meaning as σ_{jk}.

$$F_{jk} \equiv \sigma_{jk}(E,E') = \sigma_k(E')\nu_{jk}(E')P_{jk}(E,E') \tag{2.1.20}$$

where $\nu_{jk}(E')$ is the average number (referred to as multiplicity of type j particles being produced by a collision of type k with energy E', and $P_{jk}(E, E')$ is the probability density distribution for producing type j particle of energy E from a collision of type k particle of energy E'.

In sections 2.2 and 2.3 we will solve equation (2.1.19) for j = proton and j = neutron. Our approach will be to obtain an integrating factor for the equation. For protons this process is complicated by the presence of the stopping power term in the energy derivative term. We obtain a tractable form for the proton equation by employing a transformation to characteristic coordinates.

Separate development of proton and neutron transport is slightly repetitious but organizationally worthwhile because it enhances independent development and analysis of the two nucleon types.

2.2. Proton Transport

Consider the 1-D Boltzmann equation (2.1.19) for particle type j = proton. Let $F(E, E') = F_{pp}(E, E')$

$$\left[\frac{\partial}{\partial x} - \frac{\partial}{\partial E}\, S(E) + \sigma_p\,(E)\right]\, \phi_p(x, E) = \int_E^\infty F(E, E')\, \phi_p(x, E')\, dE' \qquad (2.2.1)$$

Multiply through by $S(E)$ and define

$$\psi_p(x, E) \equiv S(E)\, \phi_p(x, E)$$
$$\overline{F}(E, E') \equiv S(E)\, F(E, E') \qquad (2.2.2)$$

The variables defined by equation (2.2.2) provide a compact notation for solution of equation (2.2.1). Equation (2.2.1) becomes

$$\left[\frac{\partial}{\partial x} - S(E)\frac{\partial}{\partial E} + \sigma_p(E)\right]\psi_p(x,E) = \int_E^\infty \overline{F}(E,E')\ \phi_p(x,E')\ dE'$$

$$= \int_E^\infty \overline{F}(E,E')\ S(E')\ \phi_p(x,E')\frac{dE'}{S(E')} \qquad (2.2.3)$$

Define the "range"

$$r(E) \equiv \int_o^E \frac{dE'}{S(E')} \rightarrow dr = \frac{dE'}{S(E')} \qquad (2.2.4)$$

where $r(E)$ is the distance required to stop a proton of kinetic energy E by energy loss due to coulomb interactions with bound atomic electrons. Note the mapping

$$\overline{F}(E,E') = \overline{F}(r,r')$$

$$\psi_p(x,E') = \psi_p(x,r')$$

$$\sigma(E) = \sigma(r)$$

$$\left[\frac{\partial}{\partial x} - S(E)\ \frac{\partial}{\partial E} + \sigma_p(E)\right]\ \psi_p(x,r) = \int_r^\infty \overline{F}(r,r')\ \psi_p(x,r')dr' \qquad (2.2.5)$$

Note

$$\frac{\partial\psi(x,r)}{\partial E} = \frac{\partial\psi}{\partial r}\ \frac{\partial r}{\partial E}$$

$$\frac{\partial r}{\partial E} = \frac{1}{S(E)}$$

so that

$$S(E)\frac{\partial}{\partial E} = \frac{\partial}{\partial r}$$

Equation(2.2.6) becomes

$$\left[\frac{\partial}{\partial x} - \frac{\partial}{\partial r} + \sigma_p(x)\right]\psi_p(x,r) = \int_r^\infty \overline{F}(r,r')\ \psi_p(x,r')dr' \qquad (2.2.6)$$

We can further simplify (2.2.6) by mapping to a set of "characteristic" coordinates η, ξ defined by

$$\begin{cases} \eta \equiv x - r & x = \frac{\xi+\eta}{2} \\ \xi \equiv x + r & r = \frac{\xi-\eta}{2} \\ \frac{\partial}{\partial x} = \frac{\partial}{\partial \xi}\frac{d\xi}{dx} + \frac{\partial}{d\eta}\frac{d\eta}{dx} = \frac{\partial}{\partial \xi} + \frac{\partial}{d\eta} \\ \frac{\partial}{\partial r} = \frac{\partial}{\partial \xi}\frac{d\xi}{dr} + \frac{\partial}{d\eta}\frac{d\xi}{dr} = \frac{\partial}{\partial \xi} - \frac{\partial}{d\eta} \end{cases} \tag{2.2.7}$$

The mapping is shown in figure 9. Note that the boundary $x = 0$ maps onto $\eta = -\xi$, and $E = 0$ maps onto $\eta = \xi$. The curved line $(a - b)$ in x, E space maps to the straight line $\xi =$ constant in characteristic space. Characteristic coordinate η varies along particle path and ξ is constant along the particle trajectory so that equation (2.2.6) becomes

$$\left[2\,\frac{\partial}{\partial \eta} + \sigma_p\,(\xi, \eta)\right] \chi(\xi, \eta) = G(\xi, \eta) \tag{2.2.8}$$

where

$$\begin{aligned} G(\xi, \eta) &= \int_r^\infty \overline{F}(r, r')\ \psi_p(x, r')dr' \\ \chi(\xi, \eta) &= \psi_p(x, r) \end{aligned} \tag{2.2.9}$$

Equation (2.2.8) can be solved by use of integrating factor.[96] Given a linear differential equation of first order

$$\frac{dy}{dx} + P(x)\ y = 0$$

we write

$$P(x)dx + \frac{dy}{y} = 0$$

$$\int_{xo}^{x} P(x)dx + \ln y(x) - \ln y(x_o) = 0$$

and

$$\frac{y(x)}{y(x_o)}\ e^{\int P(x)dx} = 1$$

taking the differential of both sides gives

$$d\left[y\ e^{\int P(x)dx}\right] = y\ e^{\int P(x)dx} P(x)dx + e^{\int P(x)dx} dy = 0 \tag{2.2.10}$$

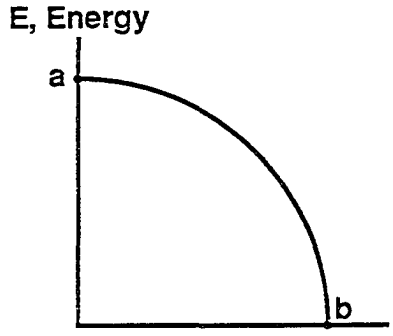

(a) x, E plane

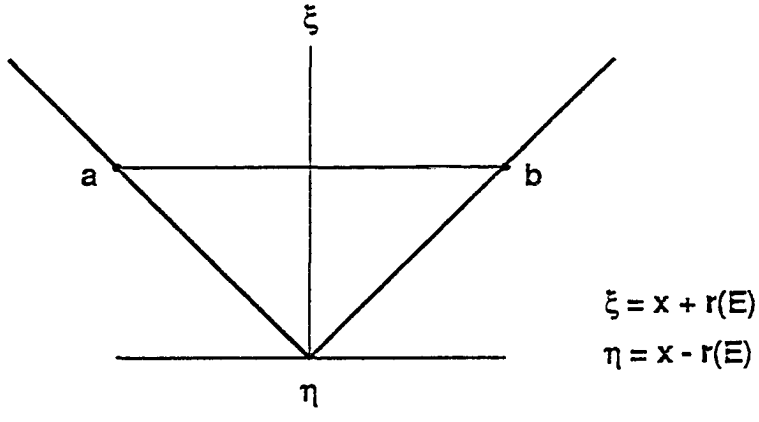

(b) (η, ξ) plane

Fig. 9 Mapping of x, E coordinates onto characteristic coordinates

this is an exact differential. We can also make an inhomogeneous equation exact. Consider

$$\frac{dy}{dx} + P(x)y = Q(x)$$

now write

$$e^{\int P(x)dx}\Big[P(x)ydx + dy\Big] = e^{\int P(x)dx}\ Q(x)\ dx \tag{2.2.11}$$

But from equation (2.2.10) this is

$$d\Big[y\ e^{\int P(x)dx}\Big] = e^{\int P(x)dx}Q(x)dx \tag{2.2.12}$$

we can write equation (2.2.8) as

$$\frac{d\chi}{d\eta} + \frac{1}{2}\sigma_p\chi = \frac{1}{2}\ G \tag{2.2.13}$$

$$\frac{d}{d\eta}\ \chi(\eta,\xi) + \frac{1}{2}\ \sigma_p\,(\eta,\xi)\ \chi(\eta,\xi) = \frac{1}{2}\ G(\eta,\xi)$$

Use integrating factor $\int_a^\eta \frac{1}{2}\sigma\,(\eta',\xi)d\eta'$. Put (2.2.13) in form of (2.2.12).

$$d\Big[\chi(\eta,\xi)\exp\left\{\int_a^\eta \frac{1}{2}\ \sigma_p\,(\eta',\xi)d\eta'\right\}\Big] = \exp\left\{\int_a^{\eta''} \frac{1}{2}\ \sigma_p\,(\eta',\xi)d\eta'\right\} G(\eta'',\xi)d\eta''$$

$$\chi(\eta,\xi)\exp\left\{\int_a^\eta \frac{1}{2}\ \sigma_p(\eta',\xi)d\eta'\right\} - \chi(a,\xi) = \int_a^\eta \exp\left\{\int_a^{\eta''} \frac{1}{2}\ \sigma_p\,(\eta',\xi)d\eta'\right\} \frac{G(\eta'',\xi)}{2}\ d\eta''$$

$$\begin{aligned}\chi(\eta,\xi) = {} & e^{-\int_a^\eta \frac{1}{2}\ \sigma_p\,(\eta',\xi)d\eta'}\ \chi(a,\xi) \\ & + e^{-\int_a^\eta \frac{1}{2}\ \sigma_p\,(\eta',\xi)d\eta'} \int_a^\eta \exp\left\{\int_a^{\eta''} \frac{1}{2}\ \sigma_p(\eta',\xi)d\eta'\right\} \frac{G(\eta'',\xi)}{2}d\eta''\end{aligned} \tag{2.2.14}$$

The effect of the characteristics mapping in (2.2.7) is shown in figure 9. Note that $x = 0$ maps into $(\eta = -r, \xi = r)$ so that $\eta_0 = a = -\xi$. For $x = x_{\max}$ we see that $r = 0$ gives

$(\eta = x,\ \xi = x)$ so that $\eta_{\max} = \xi$. We apply these limits to (2.2.14) obtaining

$$\chi(\eta,\xi) = e^{-\int_{-\xi}^{\eta} \frac{1}{2}\sigma_p(\eta',\xi)d\eta'} \chi(-\xi,\xi) + \int_{-\xi}^{\eta} \exp\left\{ \int_{-\xi}^{\eta''} - \int_{-\xi}^{\eta} \right\} \frac{G(\eta'',\xi)}{2} d\eta''$$

but

$$\int_{-\xi}^{\eta''} - \int_{-\xi}^{\eta} = \int_{-\xi}^{\eta''} + \int_{\eta}^{-\xi} = -\int_{\eta''}^{\eta}$$

$$\chi(\eta,\xi) = \exp\left[-\frac{1}{2} \int_{-\xi}^{\eta} \sigma_p(\eta',\xi)d\eta' \right] \chi(-\xi,\xi)$$
$$+ \frac{1}{2} \int_{-\xi}^{\eta} \exp\left\{ -\frac{1}{2} \int_{\eta''}^{\eta} \sigma_p(\eta',\xi)d\eta' \right\} G(\eta'',\xi)d\eta'' \qquad (2.2.15)$$

Consider the solution to equation (2.2.15) for constant crossection σ. Let

$$\sigma_p(\eta,\xi) = \sigma$$

then

$$\chi(\eta,\xi) = e^{-\frac{1}{2}\sigma(\eta+\xi)}\chi(-\xi,\xi) + \frac{1}{2} \int_{-\xi}^{\eta} e^{-\frac{1}{2}\sigma(\eta-\eta'')} G(\eta'',\xi)d\eta'' \qquad (2.2.16)$$

Use equations (2.2.7) and (2.2.9) to write (2.2.16) in terms of x and r. The inverse transformation is

$$G(\eta'',\xi) = \int_{\frac{\xi-\eta''}{2}}^{\infty} \overline{F}\left[\frac{\xi-\eta''}{2}, r' \right] \psi_p\left(\frac{\xi+\eta''}{2}, r' \right) dr'$$

Recall from equation (2.2.9) that $\chi(\xi,\eta) = \psi(x,r)$, and from (2.2.7) that $x = \frac{1}{2}(\xi+\eta)$, $r = \frac{1}{2}(\xi-\eta)$

$$\psi(x,r) = e^{-\sigma x}\psi(0,x+r) + \frac{1}{2}\int_{-(x+r)}^{x-r} d\eta''\, e^{-\frac{1}{2}\,\sigma(x-r-\eta'')} \int_{\frac{x+r-\eta''}{2}}^{\infty} \overline{F}\left[\frac{x+r-\eta''}{2}, r'\right]\psi\left(\frac{x+r+\eta''}{2}, r'\right)dr' \tag{2.2.17}$$

The notation in equation (2.2.17) can be made more compact.

Let

$$\left.\begin{aligned} z' &= \tfrac{1}{2}(x-r-\eta'') \\ \eta'' &= x-r-2z' \\ dz' &= -\tfrac{d\eta''}{2} \end{aligned}\right\} \tag{2.2.18}$$

so

and since x and r are fixed

Consider the integral limits in equation (2.2.17) using the notation of equation (2.2.18)

$$\eta'' = -(x+r) \quad \rightarrow \quad z' = \frac{1}{2}(x-r+x+r) = x$$

$$\eta'' = (x-r) \quad \rightarrow \quad z' = \frac{1}{2}(x-r-x+r) = 0$$

$$r' = \frac{x+r-\eta''}{2} = \frac{x+r-x+r+2z'}{2} = r+z'$$

$$\psi_p(x,r) = e^{-\sigma x}\psi_p(0,r+x) + \frac{1}{2}\int_{x}^{0}(-2dz')e^{-\sigma z'} \int_{r+z'}^{\infty} \overline{F}\left[r+z', r'\right]\psi_p(x-z', r')dr'$$

$$\psi_p(x,r) = e^{-\sigma x}\psi_p(0,r+x) + \int_{0}^{x} dz' e^{-\sigma z'} \int_{r+z'}^{\infty} \overline{F}\left[r+z', r'\right]\psi_p(x-z', r')dr' \tag{2.2.19}$$

Equation (2.2.19) is a key result for our study of high energy proton transport using the assumption of constant macroscopic crossection σ.

Returning to equation (2.2.15) we can obtain a similar result for energy dependent $\sigma(r)$.

$$\sigma_p(\eta',\xi) = \sigma_p(\frac{\xi-\eta'}{2})$$
$$-\frac{1}{2}\int_{-\xi}^{\eta} \sigma_p(\eta',\xi)d\eta' = -\frac{1}{2}\int_{-\xi}^{\eta} \sigma_p\left(\frac{\xi-\eta'}{2}\right)d\eta' \tag{2.2.20}$$

using equations (2.2.7) and (2.2.18)

$$\frac{\xi-\eta'}{2} = \frac{1}{2}[x+r-(x-r-2z')]$$
$$= \frac{1}{2}[2r+2z'] = r+z'$$

Integral limits:

$$\eta' = -\xi = -(x+r) \quad \rightarrow \quad z' = \frac{1}{2}(x-r+x+r) = x$$

$$\eta' = \eta = (x-r) \quad \rightarrow \quad z' = \frac{1}{2}(x-r-x+r) = 0$$

Equation (2.2.20) becomes

$$-\frac{1}{2}\int_{x}^{0} \sigma_p(r+z')\left(\frac{-dz'}{2}\right) = -\int_{0}^{x} \sigma_p(r+z')dz' \tag{2.2.21}$$

Similarly,

$$-\frac{1}{2}\int_{\eta''}^{\eta} \sigma_p(\eta',\xi)d\eta' = -\int_{0}^{z} \sigma_p(r+w)dw \tag{2.2.22}$$

Equations (2.2.21) and (2.2.22) can be used in equation (2.2.19) to give

$$\psi_p(x,r) = \exp\left\{-\int_0^x \sigma_p(r+z)dz\right\}\ \psi_p(0,r+x)$$
$$+\int_0^x dz' \exp\left\{-\int_0^{z'} \sigma_p(r+w)dw\right\}\int_{r+z}^{\infty} \overline{F}[r+z',r']\ \psi_p(x-z',r')dr' \tag{2.2.23}$$

2.3. Neutron Transport

Writing equation (2.1.19) for j = neutrons, and $F(E,E') = F_{nn}(E,E')$ and noting that $S_n(E) = 0$

$$\left[\frac{\partial}{\partial x} + \sigma_n(E)\right]\phi_n(x,E) = \int_E^\infty F(E,E')\,\phi_n(x,E')dE' \tag{2.3.1}$$

Multiply through by $S(E)$ as

$$\left[\frac{\partial}{\partial x} + \sigma_n(E)\right]S(E)\phi_n(x,E) = \int_E^\infty S(E)\,F(E,E')\;S(E')\,\phi_n(x,E')\frac{dE'}{S(E')}$$

Using the definitions and rearrangements of equations (2.2.4)–(2.2.7) we write

$$\left[\frac{\partial}{\partial x} + \sigma_n\,(r)\right]\psi_n(x,r) = \int_r^\infty \overline{F}(r,r')\,\psi_n(x,r')dr' \tag{2.3.2}$$

Note that equation (2.3.2) has same basic form as equation (2.2.13) if r is considered a parameter. Then we can write equation (2.3.2) as an ordinary differential equation.

$$\frac{d}{dx}\psi_n(x,r) + \sigma_n\,(r)\,\psi_n(r) = G(x,r)$$

and use integrating factor

$$\exp\left[\sigma_n(r)\int_0^x dx\right] = e^{\sigma_n(r)x}$$

So, using the procedure following equation (2.2.13), we write

$$d\left[\psi_n(x,r)e^{\sigma_n(r)x}\right] = e^{\sigma_n(r)x'}G(x',r)dx'$$

$$\psi_n(x,r)e^{\sigma_n(r)x} - \psi_n(0,r) = \int_0^x e^{\sigma_n(r)x'}G(x',r)dx'$$

$$\psi_n(x,r) = e^{-\sigma_n(r)x}\psi_n(0,r) + \int_0^x dx'\;e^{\sigma_n(r)(x'-x)}\int_r^\infty \overline{F}(r,r')\psi_n(x',r')dr' \tag{2.3.3}$$

Let

$$z = x - x' \quad dz = -dx'$$

Integral limits are:

$$x' = 0 \rightarrow \quad z = x$$

$$x' = x \rightarrow \quad z = 0 \tag{2.3.4}$$

Then equation (2.3.3) becomes

$$\psi_n(x,r) = e^{-\sigma_n(r)x}\psi_n(0,r) + \int_0^x dz\; e^{-\sigma_n(r)z} \int_r^\infty \overline{F}(r,r')\psi_n(x-z,r')dr' \tag{2.3.5}$$

2.4. Coupled Transport

In deriving equations (2.2.23) and (2.3.5) we obtained analytical solutions for nucleon fluences. The only assumption made was the straight ahead approximation.

A complete model for high energy nucleon transport must provide for diverse elastic and nonelastic interactions between projectiles and constituent target nuclei. Our approach assumes that only the nucleon components of collision process will propagate with the beam. We assume that other products will not move far from the collision site before depositing their kinetic energy and that their effect (e.g., Dose) can be modeled separately. The development of this process is described in Appendix C.

In our propagation model the production spectra must allow for a projectile nucleon of type i to produce propagated collision nucleons of type j.

Then $F_{ji}(E,E')$ = Production of nucleons of type j with energy E form a projectile of type i with energy E'. Then equations (2.2.23) and (2.3.5) become

$$\psi_p(x,r) = \exp\left[-\int_0^x \sigma_p(r+z)dz\right]\psi_p(0,r+x) + \int_0^x dz \exp\left[-\int_0^z \sigma_p(r+w)dw\right]\left\{\int_{r+z}^{\infty} \overline{F}_{pp}(r+z,r')\,\psi_p(x-z,r')dr' + \int_{r+z}^{\infty} \overline{F}_{pn}(r+z,r')\,\psi_n(x-z,r')dr\right\} \quad (2.4.1)$$

$$\psi_n(x,r) = \exp\left[-\sigma_n(r)x\right]\psi_n(0,r) + \int_0^x dz \exp\left[-\sigma_n(r)z\right]\left\{\int_r^{\infty} \overline{F}_{nn}(r,r')\,\psi_n(x-z,r')dr' + \int_r^{\infty} \overline{F}_{np}(r,r')\,\psi_p(x-z,r')dr'\right\} \quad (2.4.2)$$

Equations (2.4.1) and (2.4.2) may be combined into a compact representation[15] as

$$\psi_j(x,r) = \exp\left[-\int_0^x \sigma_j(r+\nu_j z)dz\right]\psi_j(0,r+\nu_j x) + \int_0^x dz \exp\left[-\int_0^z \sigma_j(r+\nu_j w)\right]\sum_i \int_{r+\nu_j z}^{\infty} \overline{F}_{ji}(r+\nu_j z,r')\,\psi_i(x-z,r')dr' \quad (2.4.3)$$

where $\nu_{\text{Proton}} = 1$ and $\nu_{\text{Neutron}} = 0$ and the i summation denotes projectile nucleon type.

The use of the range coordinate in place of energy is deliberate. Range is a smooth function over the entire span of projectile kinetic energy. However, $S(E) = dE/dx$ is very steep at low energy. This means that a numerical method based on the energy variable will require substantially more grid points than a range based scheme for a given degree of physical resolution.

The double integral in equation (2.4.3) is not easy to solve. Direct numerical simulation requires an unrealistically high operation count. In the next section we describe a perturbation approach which allows for iterative convergence to the desired level of accuracy.

2.5. Perturbation Theory for Nucleon Transport

The integral equations (2.4.1) and (2.4.2) are of the form[97]

$$\phi(x) = F(x) + \lambda \int_a^x K(x,t)\varphi(t)dt$$

This is classified as a Volterra equation of the "Second Kind". The "First Kind" has $F(x) = 0$. If the integral contained two definite limits it would be classified as a Fredholm equation.

One straight forward approach to the solution of equation (2.4.3) for bounded kernel $K(x,t)$[98,99] is a perturbation approach. This is an iterative technique for successive powers of λ, starting with

$$\phi(x) \approx F(x) \tag{2.5.1}$$

then

$$\phi(x) = F(x) + \lambda \int_a^x K(x,t)F(t)dt + \lambda^2 \int_a^x dt \int_a^t dt' K(x,t)K(t,t')F(t') + ... \tag{2.5.2}$$

Equation (2.5.2) is called a Neumann series. For sufficiently small parameter λ, it will converge. Using the formalism of equation (2.5.2) we define the Boltzmann operator B to represent field drift and collisional losses (atomic and nuclear) and G_o as the Boltzmann propagator formed from the inverse of the integrating factor for B. The method of characteristics discussed previously shows that G_o is the solution of

$$BG_o = 0 \tag{2.5.3}$$

the general solution of the Boltzmann equation is then

$$\phi = G_o\phi_B + B^{-1}C\phi \tag{2.5.4}$$

where ϕ_B is the specified boundary fluence and C is an integral operator for the secondary production terms. The Neumann series for equation (2.5.4) can be written[1,11] as

$$\phi = G_o\phi_B + B^{-1}CG_o\phi_B + B^{-1}CG_oB^{-1}CG_o\phi_B + \ldots \tag{2.5.5}$$

If the complete propagator is labelled G then

$$\phi = G\phi_B \tag{2.5.6}$$

and

$$G = G_o + B^{-1}CG \tag{2.5.7}$$

G depends, in general, on the bounding surface and the physical properties of the target media.[47] The perturbation series (2.5.5) has been used previously[1] to form the basis for a physical representation of high energy nucleon transport through extended matter. In this approach, $G_o\phi_B$ represents the uncollided "primaries." The primaries can create "first generation" secondaries and so on. The boundedness of this series expansion can be seen physically by noting that each generation decays exponentially. First generation secondaries can only be created by primaries. The primaries decay like $\exp(-\sigma x)$ guaranteeing that the loss mechanisms will eventually overpower the source terms for the first generation secondaries. This feature propagates to all orders of the series. We seek a series of the form

$$\psi_j(x,r) = \sum_{i=0}^{\infty} \psi_j^i(x,r) \tag{2.5.8}$$

satisfying the boundary condition at $x = 0$ that

$$\psi_j^0(0,r) = \psi(r) \tag{2.5.9}$$

$$\psi_j^i(0,r) = 0 \qquad \text{for } i \geq 1 \tag{2.5.10}$$

The prescription of equations (2.5.3)–(2.5.10) applied to equations (2.4.1) and (2.4.2) leads to

$$\psi_p^0(x,r) = \exp\Big[-\int_0^x \sigma_p(r+z)dz\Big]\,\psi_p(0,r+x) \tag{2.5.11}$$

$$\psi_p^i(x,r) = \int_0^x dz \exp\Big[-\int_0^z \sigma_p(r+w)dw\Big]\left\{\int_{r+z}^{\infty} \overline{F}_{pp}(r+z,r')\,\psi_p^{i-1}(x-z,r')dr' + \int_{r+z}^{\infty} \overline{F}_{pn}(r+z,r')\,\psi_n^{i-1}(x-z,r')dr'\right\} \tag{2.5.12}$$

$$\psi_n^0(x,r) = \exp\Big[-\sigma_n(r)x\Big]\,\psi_n(0,r) \tag{2.5.13}$$

$$\psi_n^i(x,r) = \int_0^x dz \exp\Big[-\sigma_n(r)z\Big]\left\{\int_r^{\infty} \overline{F}_{nn}(r,r')\,\psi_n^{i-1}(x-z,r')dr' + \int_r^{\infty} \overline{F}_{np}(r,r')\,\psi_p^{i-1}(x-z,r')dr'\right\} \tag{2.5.14}$$

Equations (2.5.12) and (2.5.14) apply to $i \geq 1$. Equations (2.5.11)–(2.5.14) are solved in a recursive fashion until satisfactory convergence is obtained.

Equation (2.5.5) was implemented in a computer program[1,11] to study the coupled transport of successive generation of secondary nucleons. A simplified form for the production spectra $\overline{F}_{ji}$ was employed[100] and the macroscopic crossection and projectile multiplication were assumed to be constants. The boundary condition was specified to be a 1 GeV (monoenergetic) beam of normally incident on a tissue slab. Figure 10 shows the evolution of secondary protons out to 60 cm of tissue penetration.[1] The secondary fluence is, of course, zero at the boundary but builds quickly to a plateau around 30 cm. $\psi_p^{(1)}$ is formed from the collisions of primary proton projectiles. $\psi_p^{(2)}$ is sum of $\psi_p^{(1)}$ and the secondary generation formed by collisions of $\psi_n^{(1)}$ neutrons (there is no $\psi_n^{(0)}$ component in the problem). The significant result of this analysis is that proton fluence rapidly converges. The proton fluence out to 60 cm is closely approximated by the primaries and two generations of secondaries.

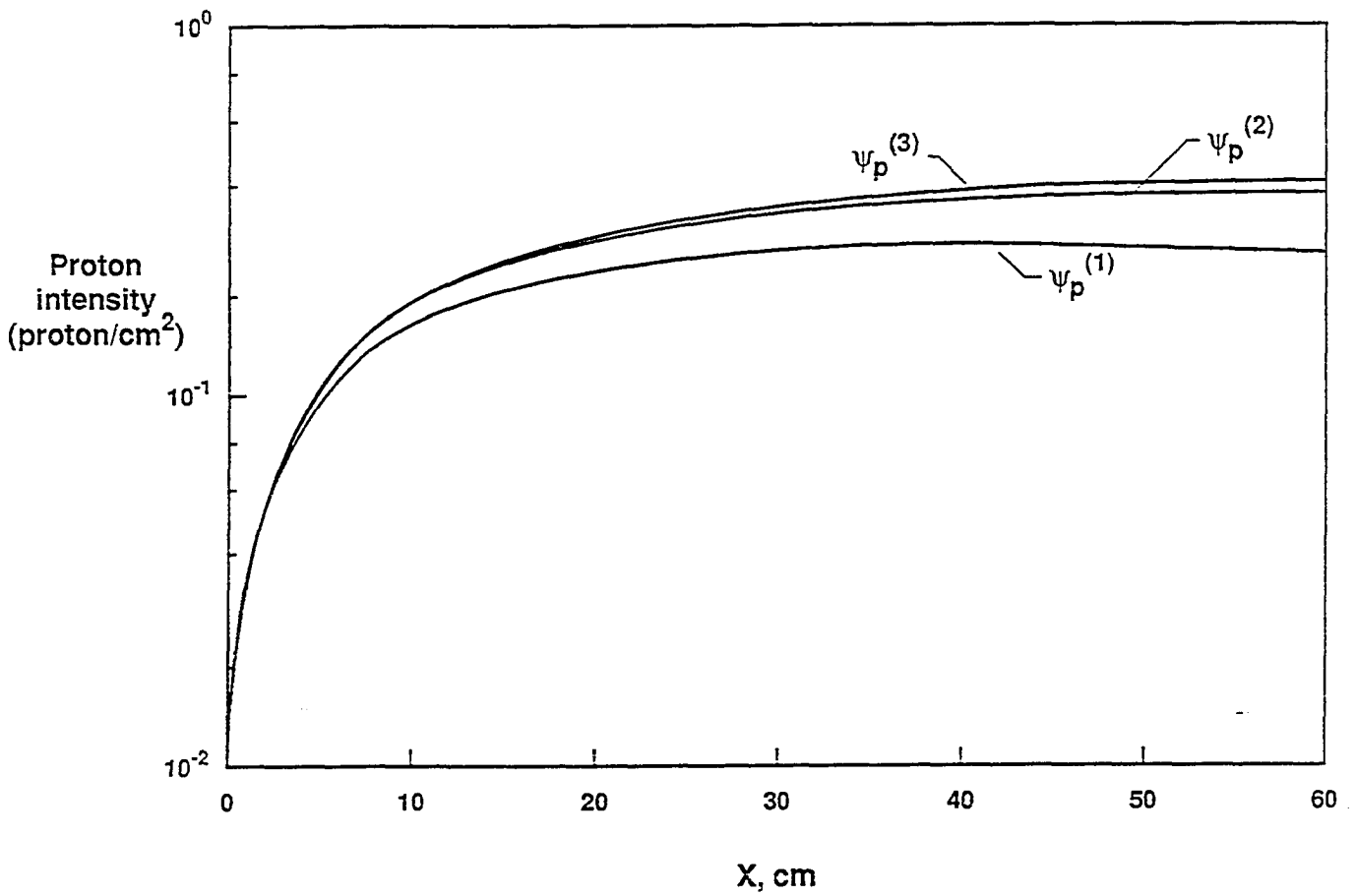

Fig. 10 Integrated intensities as a function of penetration depth in first, second and third order approximation to secondary protons

The plateauing is explained by two offsetting processes. The protons, will slow down due to atomic collisions so each generation of secondaries cannot sustain itself. However the neutrons are not slowed and will continue to contribute to proton production through the Boltzmann coupling mechanism. We see the effect of secondary neutron growth[1] in figure 11. We see first that the relative magnitude of $\psi_n^{(2)}$ at 60 cm penetration depth is four times greater than $\psi_p^{(2)}$. We also see that no plateau effect is evident in the neutron fluence.

Figure 12 shows[1] the contributions to dose from successive generations of protons. Proton dose is given by

$$\begin{aligned} D_p(x) &= \int_0^\infty S_p(E)\phi_p(x,E)\ dE \\ &= \int_0^\infty \psi(x,r')\ dr' \end{aligned} \tag{2.5.15}$$

The uncollided primaries display an exponential decay as expected. We also see see the plateau effect for the secondaries. Note that $D_p^{(1)}$ peaks near 30 cm and then begins to decay. The results of the analysis in figures 10–12 provide useful qualitative insight into the effectiveness of the iterative convergence procedure for the Neumann series. The neutrons are not easily converged using this method but the dose for relatively short penetration depths, is converged to within acceptable limits.

The problem with the iterative approach lies in the computational expense of implementing the numerical scheme. We used a quadrature to solve the collision terms and were required to store the entire field of successive generation of particles into memory (60 space, and 1000 energy points) for bi-cubic spline interpolation. Since the goal of this work is to provide accurate estimates of nucleon exposure using workstation class computers, we seek an alternative approach to the numerical scheme. To minimize operation count (i.e., computer arithmetic) we will employ a numerical marching procedure. We will simplify the required integrals by replacing selected variable arguments with suitably chosen constants. In order to develop a procedure for determining the values of these constants we first require the exact solutions to some benchmark transport cases.

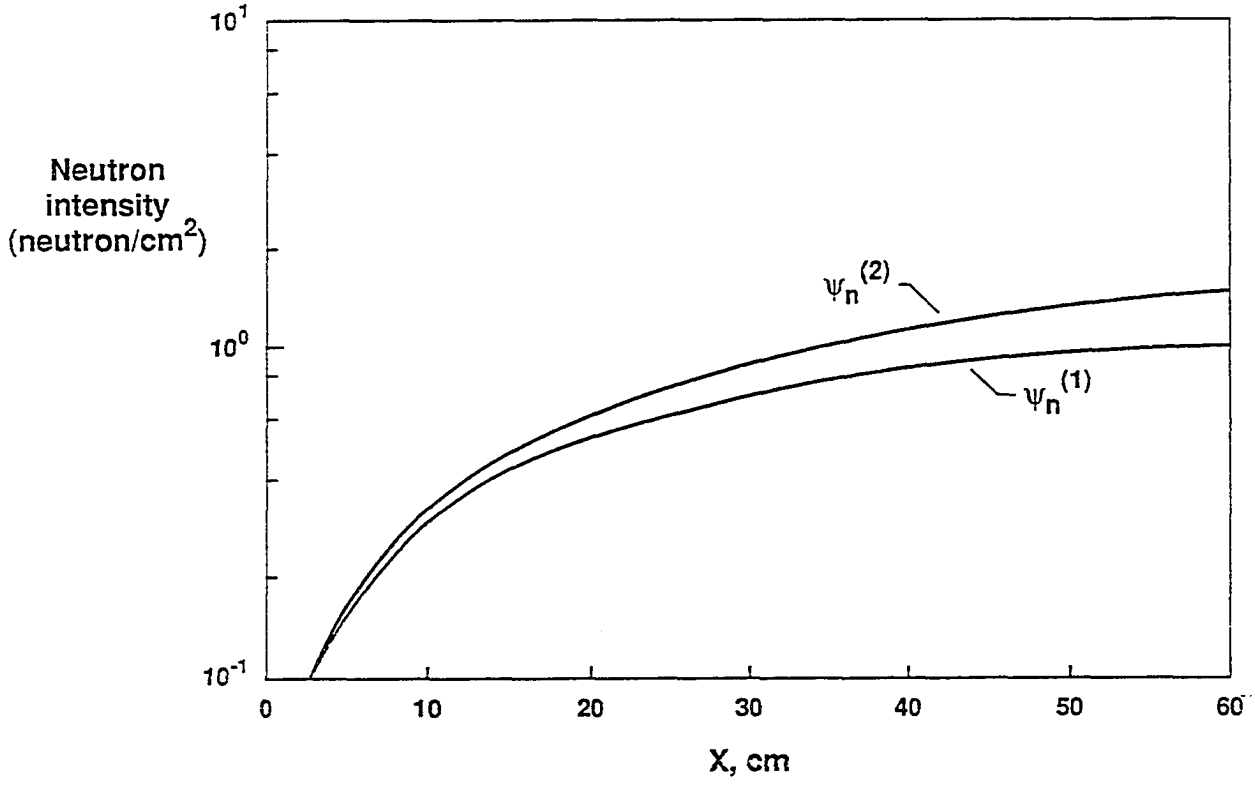

Fig. 11 Integrated intensities as a function of penetration depth for first and second order approximation to secondary neutrons.

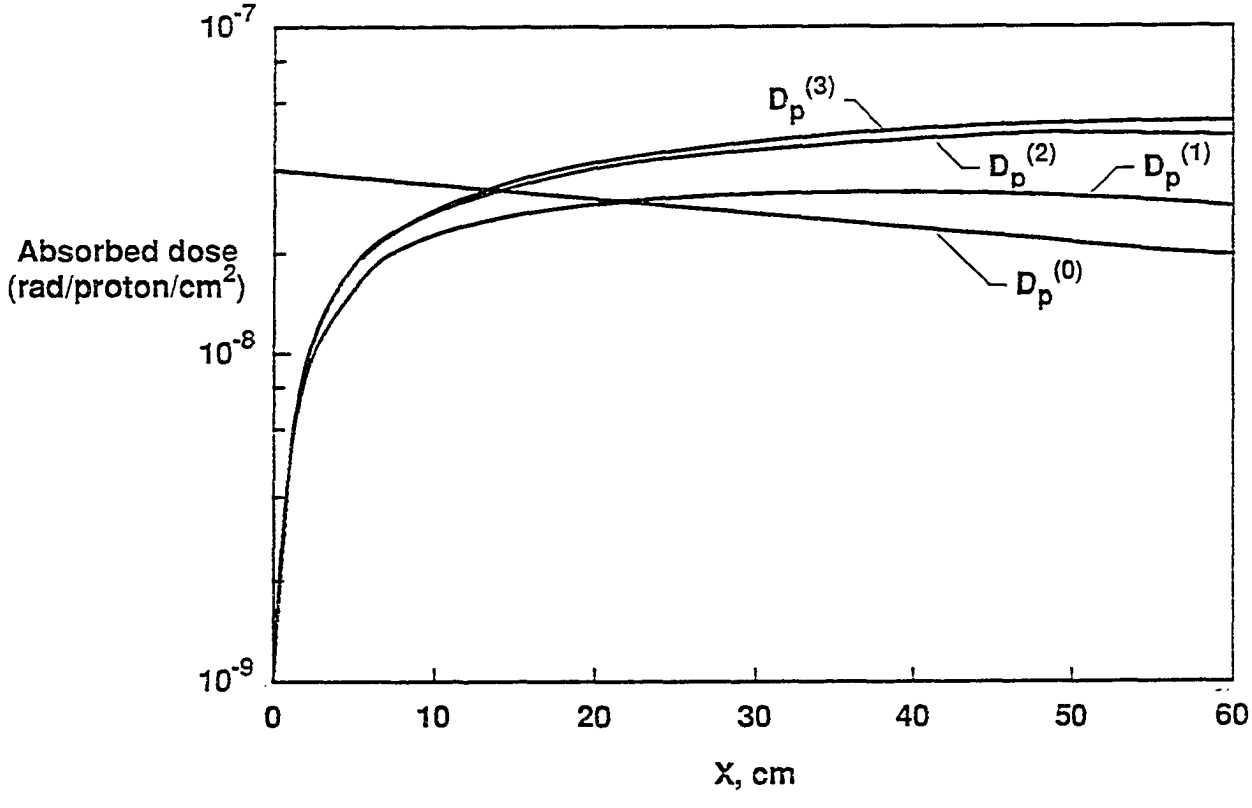

Fig. 12 Proton doses in tissue:

$D_p^{(0)}$ Primary proton dose

$D_p^{(N)}$ N^{th} approximation to secondary dose

3. Continuous Benchmark Cases

Recursive application of equations (2.5.11)–(2.5.14) provides a methodology for obtaining solutions for nucleon fluxes. In general, of course, we do not have analytical expressions available for $F(r,r')$ and $\psi_j(x,r')$ so that numerical methods must be employed. Numerical solutions to arbitrary accuracy are typically not feasible. We seek ways to determine the physical effect of approximative numerical procedures on the accuracy of our solution.

In this chapter we consider expressions for the incident fluence and production spectra that allow for analytical evaluation of the integrals. These solutions can be used as benchmarks to test the accuracy of numerical procedures. We will now consider the case of an incident nucleon spectrum with a continuous energy distribution. This case is relevant for the space radiation environment (fig. 2). Monoenergetic benchmarks are considered in Appendix A. The methodology is the same for both cases.

Our choice for $\overline{F}_{ji}$ is motivated by the interesting result of Turner, Wright, and Grossen[101] that the shielding properties can be approximately represented by taking the nuclear properties as a uniform distribution of free nucleons. The scattered nucleon spectrum is represented by

$$\overline{F}_{pp}(r,r') = \overline{F}_{nn}(r,r') = k_1\, e^{\alpha(r'-r)} \tag{3.1}$$

$$\overline{F}_{pn}(r,r') = \overline{F}_{np}(r,r') = k_2\, e^{\alpha(r'-r)} \tag{3.2}$$

where α, k_1, and k_2 are constants. This form reasonably represents the most energetic particles produced (quasi-elastic) in nuclear collisions. Also, assume macroscopic crossections are energy independent

$$\sigma_p(r) = \sigma_p \tag{3.3}$$

$$\sigma_n(r) = \sigma_n \tag{3.4}$$

For the incident flux we set

$$\psi(0,r) = (\delta_p + \delta_n)e^{-\beta r} \tag{3.5}$$

The Kronecker delta δ_j is

$= 0$ Type j nucleons absent from incident beam

$= 1$ Type j nucleons present in the incident beam

Now apply equations (3.1)–(3.5) to (2.5.11)–(2.5.14)

$$\psi_p^0(x,r) = e^{-\sigma x}\delta_p\, e^{-\beta(r+x)} \tag{3.6}$$

$$\psi_n^0(x,r) = e^{-\sigma x}\delta_n\, e^{-\beta(r)} \tag{3.7}$$

$$\begin{aligned}
\psi_p^1(x,r) &= \int_0^x dz\, e^{-\sigma z}\left\{\int_{r+z}^{\infty} \overline{F}_{pp}(r+z,r')\,\psi_p^0(x-z,r')dr'\right. \\
&\quad \left. + \int_{r+z}^{\infty} \overline{F}_{pn}(r+z,r')\,\psi_n^0(x-z,r')dr'\right\} \\
&= \int_0^x dz\, e^{-\sigma z}\left\{\int_{r+z}^{\infty} k_1\, e^{-\alpha(r'-r-z)}\delta_p\, e^{-\sigma(x-z)}\, e^{-\beta(r'+x-z)}dr'\right. \\
&\quad \left. + \int_{r+z}^{\infty} k_2\, e^{-\alpha(r'-r-z)}\delta_n\, e^{-\sigma(x-z)}\, e^{-\beta(r)}dr'\right\} \\
&= \int_0^x dz\, e^{-\sigma x}\left[k_1\delta_p\, e^{-\beta(x-z)} + k_2\delta_n\right]\int_{r+z}^{\infty} e^{-\alpha(r'-r-z)}\, e^{-\beta r}dr' \\
&= \int_0^x dz\, e^{-\sigma x}\left[k_1\delta_p\, e^{-\beta(x-z)} + k_2\delta_n\right]\frac{e^{-\beta(r+z)}}{(\alpha+\beta)} \\
&= \frac{e^{-\sigma x}}{(\alpha+\beta)}\left[k_1\delta_p\int_0^x dz\, e^{-\beta(x+r)} + k_2\delta_n\int_0^x dz\, e^{-\beta(r+z)}\right]
\end{aligned} \tag{3.8}$$

$$\psi_p^1(x,r) = \frac{e^{-\sigma x}}{(\alpha+\beta)}\left[k_1\delta_p\, x\, e^{-\beta(x+r)} + k_2\delta_n\frac{e^{-\beta(x+r)}}{\beta}\,(e^{\beta x}-1)\right] \tag{3.9}$$

$$\psi_n^1(x,r) = \int_0^x dz\ e^{-\sigma z} \left\{ \int_r^\infty \overline{F}_{nn}(r,r')\,\psi_n^0(x-z,r')dr' + \int_r^\infty \overline{F}_{np}(r,r')\,\psi_p^0(x-z,r')dr' \right\}$$

ψ_p^0 and ψ_n^0 are available from equations (3.6) and (3.7)

$$\begin{aligned}\psi_n^1(x,r) &= \int_0^x dz\ e^{-\alpha z} \left\{ \int_r^\infty k_1\ e^{-\alpha(r'-r)}\delta_n\ e^{-\sigma(x-z)}\ e^{-\beta r'}dr' \right. \\ &\quad \left. + \int_r^\infty k_2\ e^{-\alpha(r'-r)}\delta_p\ e^{-\sigma(x-z)}\ e^{-\beta(r'+x-z)}dr' \right\} \\ &= \int_0^x dz\ e^{-\sigma x}\ e^{\alpha r}\left[k_1\delta_n + k_2\delta_p\ e^{-\beta(x-z)}\right]\frac{e^{-(\alpha+\beta)r}}{(\alpha+\beta)} \\ &= \frac{e^{-\sigma x}\ e^{-\beta r}}{(\alpha+\beta)}\left[k_1\delta_n x + k_2\frac{\delta_p}{\beta}\left(1-e^{-\beta x}\right)\right]\end{aligned}$$

$$\psi_n^1(x,r) = \frac{e^{-\sigma x}\ e^{-\beta(r+x)}}{(\alpha+\beta)}\left[k_1\delta_n x\ e^{\beta x} + \frac{k_2\delta_p}{\beta}\left(e^{\beta x}-1\right)\right] \tag{3.10}$$

Equations (3.9) and (3.10) can be used to obtain the second order terms

$$\psi_p^2(x,r) = \int_0^x e^{-\sigma z}dz \left\{ \int_{r+z}^\infty \overline{F}_{pp}(r,r')\,\psi_p^1(x-z,r')dr' + \int_{r+z}^\infty \overline{F}_{pn}(r,r')\,\psi_n^1(x-z,r')dr' \right\}$$

$$\begin{aligned}\psi_p^2(x,r) = \int_0^x dz\ e^{-\sigma z} \int_{r+z}^\infty dr'\ \frac{e^{-\sigma(x-z)}}{(\alpha+\beta)}\ e^{-\beta(r'+x-z)} \\ \left\{ k_1\ e^{\alpha(r'-r-z)}\left[k_1\delta_p(x-z) + \frac{k_2}{\beta}\delta_n\left(e^{\beta(x-z)}-1\right)\right] \right. \\ \left. + k_2\ e^{\alpha(r'-r-z)}\left[k_1\delta_n(x-z)e^{\beta(x-z)} + \frac{k_2}{\beta}\delta_p\left(e^{\beta(x-z)}-1\right)\right] \right\}\end{aligned}$$

$$= \int_0^x dz \frac{e^{-\sigma x}}{(\alpha+\beta)} \int_{r+z}^{\infty} e^{-\beta(r'+x-z)}\, e^{-\alpha(r'-r-z)} \Big\{ \ldots \Big\} dr'$$

$$= \int_0^x dz \frac{e^{-\sigma x}}{(\alpha+\beta)}\, e^{-\beta(x-z)}\, e^{\alpha(r+z)}\, \frac{e^{-(\alpha+\beta)(r+z)}}{(\alpha+\beta)} \Big\{ \ldots \Big\}$$

$$= \frac{e^{-\sigma x}\, e^{-\beta(r+x)}}{(\alpha+\beta)^2} \int_0^x dz \Big\{ \ldots \Big\}$$

$$= \frac{e^{-\sigma x}\, e^{-\beta(r+x)}}{(\alpha+\beta)^2} \int_0^x dz \left[k_1^2 \delta_p (x-z) + \frac{k_1 k_2}{\beta} \delta_n \left(e^{\beta(x-z)} - 1 \right) \right.$$

$$\left. + k_2 k_1 \delta_n (x-z)\, e^{\beta(x-z)} + \frac{k_2^2 \delta_p}{\beta} \left(e^{\beta(x-z)} - 1 \right) \right]$$

$$\psi_p^2(x,r) = \left(\ldots \right) \left[k_1^2 \delta_p \left(x^2 - \frac{x^2}{2} \right) + \left(\frac{k_1 k_2 \delta_n}{\beta} + \frac{k_2^2 \delta_p}{\beta} \right) \left[\frac{1}{\beta} \left(e^{\beta x} - 1 \right) - x \right] \right.$$

$$\left. + \int_0^x k_2 k_1 \delta_n (x-z)\, e^{\beta(x-z)} dz \right]$$

but

$$\int_0^x (x-z)\, e^{\beta(x-z)} dz = -\int_x^0 z'\, e^{\beta z'} dz \quad \text{for} \quad z' = x - z$$

$$= \frac{e^{\beta x}}{\beta} \left(x - \frac{1}{\beta} \right) + \frac{1}{\beta} 2$$

so

$$\psi_p^2(x,r) = \frac{e^{-\sigma x}\, e^{-\beta(r+x)}}{(\alpha+\beta)^2} \left[k_1^2 \delta_p \frac{x^2}{2} + \frac{k_1 k_2}{\beta^2} \delta_n \left(e^{\beta x} - 1 - \beta x \right) \right.$$

$$\left. + \frac{k_2^2 \delta_p}{\beta^2} \left(e^{\beta x} - 1 - \beta x \right) + \frac{k_2 k_1}{\beta^2} \delta_n \left(\beta x\, e^{\beta x} - e^{\beta x} - 1 \right) \right]$$

$$\psi_p^2(x,r) = \frac{e^{-\sigma x}\, e^{-\beta(r+x)}}{(\alpha+\beta)^2} \left[k_1^2 \delta_p \frac{x^2}{2} + k_2 \left\{ \frac{k_2 \delta_p}{\beta^2} \left(e^{\beta x} - 1 - \beta x \right) \right. \right.$$

$$\left. \left. + \frac{k_1 \delta_n x}{\beta} \left(e^{\beta x} - 1 \right) \right\} \right] \tag{3.11}$$

the second order neutrons are

$$\psi_n^2(x,r) = \int_0^x dz\; e^{-\sigma z}\left\{\int_r^\infty \overline{F}_{nn}(r,r')\,\psi_n^1(x-z,r')dr' + \int_r^\infty \overline{F}_{np}(r,r')\,\psi_p^1(x-z,r')dr'\right\}$$

$$= \int_0^x dz\; e^{-\sigma z}\int_r^\infty dr' \frac{e^{-\sigma(x-z)}}{(\alpha+\beta)}\; e^{-\beta(r'+x-z)}\left\{k_1\; e^{-\sigma(r'-r)}\left[k_1\delta_n(x-z)\;\; e^{\beta(x-z)} + \frac{k_2\delta_p}{\beta}\left(e^{\beta(x-z)}-1\right)\right] + k_2 e^{-\alpha(r'-r)}\left[k_1\delta_p(x-z) + \frac{k_2\delta_n}{\beta}\left(e^{\beta(x-z)}-1\right)\right]\right\}$$

$$= \frac{e^{-\sigma x}e^{-\beta r}}{(\alpha+\beta)^2}\int_0^x e^{-\beta(x-z)}\left\{\ldots\right\}dz$$

We will need the following;

$$\int_0^x dz\; e^{-\beta(x-z)} = \frac{1}{\beta}(1-\; e^{-\beta x})$$

$$\int_0^x dz(x-z)\; e^{-\beta(x-z)} = -\int_x^0 dz' z'\; e^{-\beta z'} = \frac{e^{-\beta x}}{\beta^2}\left[-1+e^{\beta x}-\beta x\right]$$

then

$$\psi_n^2(x,r) = \frac{e^{-\sigma x}e^{-\beta r}}{(\alpha+\beta)^2}\left[k_1^2\delta_n\left(x^2-\frac{x^2}{2}\right) + \frac{k_2k_1\delta_p}{\beta}\left(x-\frac{1}{\beta}\left(1-e^{-\beta x}\right)\right) + k_2k_1\delta_p\frac{e^{-\beta x}}{\beta^2}\left(-1+e^{\beta x}-\beta x\right) + \frac{k_2^2\delta_n}{\beta}\left(x-\frac{1}{\beta}\left(1-e^{-\beta x}\right)\right)\right]$$

$$\psi_n^2(x,r) = \frac{e^{\sigma x}e^{-\beta(r+x)}}{(\alpha+\beta)^2}\left[k_1^2\delta_n\frac{x^2}{2}\; e^{\beta x} + k_2\left\{k_1\delta_p\frac{x}{\beta}\left(e^{\beta x}-1\right) + \frac{k_2\delta_n}{\beta}\left[x\; e^{\beta x} - \frac{1}{\beta}\left(e^{\beta x}-1\right)\right]\right\}\right] \tag{3.12}$$

We now have a set of analytical solutions for ψ_p and ψ_n to the second order in the secondary spectrum. These results can be used as benchmarks about which to establish a desired level of accuracy in the numerical scheme used to compute the general case. In the next chapter we describe the numerical solution.

4. Numerical Method

4.1. Numerical Marching Method

Equations (2.2.23) and (2.3.5) provide solutions for the proton and neutron fluence components of high energy nucleon transport. Equations (2.4.1) and (2.4.2) explicitly show the coupling of the fluence components. Equations (2.5.11)–(2.5.14) suggest a recursive perturbation methodology for obtaining type j nucleon fluences.

In this section we will develop a strategy for the numerical implementation of these transport solutions. Our approach will be to minimize the numerical operations count within the constraint of some pre-defined level of solution accuracy.

It is natural to seek a spatial marching scheme to simulate nucleon transport. Our paradigm begins with a specified fluence incident at the boundary ($x = 0$). We then compute the solution at some small distance h into the target material. These values are used as new boundary conditions to propagate the solution an added distance h.

We can write equation (2.4.3) for spatial position $x + h$ with assumed boundary x as[102]

$$\begin{aligned}\psi_j(x+h,r) = \; & e^{-\sigma_j h}\psi_j(x, r+\nu_j h) \\ & + \int_0^h dz\, e^{-\sigma_j z} \sum_i \int_{r+\nu_j z}^{\infty} \overline{F}_{ji}(r+\nu_j z, r')\psi_i(x+h-z, r')dr' \end{aligned} \quad (4.1.1)$$

where we have assumed the σ's to be energy independent. The analysis is not affected by this choice but the notation is made less cumbersome.

It is clear that the computational effort in equation (4.1.1) lies in evaluating the double integral over space and energy. Our strategy will be to decouple the interior integrand.

Recall from our discussion of perturbation theory that to first order accuracy in t the flux can be represented by equations (2.5.11) and (2.5.13) as

$$\psi_i(x+t,r) = e^{-\sigma t}\psi(x, r+\nu_i t) + O(h) \quad (4.1.2)$$

Let

$$t = h - z$$

then to within $O(\sigma h)$

$$\psi_i(x + h - z, r') \approx e^{-\sigma(h-z)}\psi_i(x, r' + \nu_i(h - z)) \tag{4.1.3}$$

Substituting equation (4.1.3) into (4.1.1) gives

$$\begin{aligned}\psi_j(x + h, r) = \; & e^{-\sigma_j h}\, \psi_j(x, r + \nu_j h) \\ & + \int_0^h dz\; e^{-\sigma_j z} \sum_i \int_{r+\nu_j z}^{\infty} dr' \overline{F}_{ji}(r + \nu_j z, r') \\ & \times e^{-\sigma_i(h-z)}\psi_i[x, r' + \nu_i(h - z)] + O(\sigma^2 h^2)\end{aligned} \tag{4.1.4}$$

Note that upon integration we recover second order accuracy in space.[103] However, equation (4.1.4) needs reduction for efficient computer implementation. The error term in equation (4.1.4) is expected to be small since σ_j itself is small. Now transform the integration variables as

$$r'' = r' - \nu_j z \;\text{ so that }\; dr'' = dr'$$

Limits are:

$$r' = r + \nu_j z \longrightarrow r'' = r$$

$$r' = \infty \longrightarrow r'' = \infty$$

so that equation (4.1.4) can be written as

$$\begin{aligned}\psi_j(x + h, r) = e^{-\sigma_j h}\psi_j(x, r + \nu_j h) + e^{-\sigma_j h} \int_0^h dz \\ \times \sum_i \int_r^{\infty} dr''\; \overline{F}_{ji}(r + \nu_j z, r'' + \nu_j z)\; \psi_i[x, r'' + \nu_i h + (\nu_j - \nu_i)z]\end{aligned} \tag{4.1.5}$$

Recall that we are using energy independent values for the macroscopic crossections. Equation (4.1.5) includes the further assumption that

$$\sigma_j \approx \sigma_i$$

so that

$$e^{-(\sigma_j-\sigma_i)z} \approx 1$$

We seek to decouple the integrals in equation (4.1.5) while maintaining second order accuracy. We propose a solution of the form

$$\psi_j(x+h,r) = e^{-\sigma_j h}\psi_j(x, r+\nu_j h) + \sum_i e^{-\sigma_j h} \int_{r+Q_1{}^{ji}}^{\infty} \psi_i(x, r'+Q_2^{ji}) \int_0^h \overline{F}_{ji}(r+\nu_j z, r')dr'dz \qquad (4.1.6)$$

The values of Q_1^{ji} and Q_2^{ji} are chosen to minimize the per step error, and their values depend on the (j,i) combination of terms. The integration of z in equation (4.1.6) is related to the cumulative secondary particle spectrum produced by the interaction term $\overline{F}_{ji}(r,r')$. We now examine how the local truncation error per step is propagated in the numerical procedure.

4.2. Error Propagation

Errors are introduced into equation (4.1.6) through numerical interpolation of $\psi_j(x, r+\nu_j h)$ between grid points in r as well as through the values Q_1^{ji} and Q_2^{ji}. If the value $\psi_j(kh, r_i)$ is the value of the solution at the kth step and the ith grid point then

$$\psi_j(kh, r_i) = \psi_{numj}(kh, r_i) + \sum_{l=0}^{k-1} e^{-\sigma(k-l)h}\epsilon_l(h) \qquad (4.2.1)$$

where $\epsilon_l(h)$ is the error committed at the lth step. Suppose $0 \leq \epsilon_l(h) \leq \epsilon(h)$ for all values of l, then the propagated error is bounded by

$$\epsilon_{prp}(h) = \sum_{l=0}^{k-1} e^{-\sigma(k-l)h}\epsilon_l(h) \quad \leq \quad \epsilon(h)\sum_{l=0}^{k-1} e^{-\sigma(k-l)h} \tag{4.2.2}$$

Clearly,

$$\epsilon_{prp}(h) \leq \frac{\epsilon(h)}{h\sigma}\left(1 - e^{-\sigma kh}\right) \tag{4.2.3}$$

where $\epsilon(h)$ is the maximum error per step. To insure adequate error control, one requires the bound on the local relative error $\epsilon(h)$ to be on the order of $O(h^2)$. This has been demonstrated in recent studies.[104] We now examine the local relative error generated by equation (4.1.6).

4.3. Local Relative Error-Continuous Benchmark Case

In this section we will seek suitable values for Q_1^{ij} and Q_2^{ij} to maintain second order accuracy in the case of a continuously distributed incident nucleon spectrum.

We will evaluate the first order secondaries ($i = 1$) from equations (2.5.12) and (2.5.14) written in the form of equation (4.1.5).

4.3.1. Proton Flux

Using equation (4.1.5) we write (2.5.12) as

$$\psi_p^1(x+h,r) = e^{-\sigma_p h}\int_0^h dz \left[\int_r^\infty dr''\, \overline{F}_{pp}(r+z,r'+z)\psi_p^0(x,r'+h) + \int_r^\infty \overline{F}_{pn}(r+z,r'+z)\ \psi_n^0(x,r'+z)dr'\right] \tag{4.3.1.1}$$

Examine the $\overline{F}_{pp}$ and $\overline{F}_{pn}$ integrals separately as ψ^1_{pp} and ψ^2_{pn}.

$$\psi^1_{pp}(x+h,r) = e^{-\sigma_p h}\int_r^\infty dr'\psi^0_p(x,r'+h)\int_0^h \overline{F}_{pp}(r+z,r'+\gamma)dz \tag{4.3.1.2}$$

where γ is a constant to be determined which maintains $O(h^2)$ accuracy. Using equations (3.1)-(3.7) in (4.3.1.2) we get

$$\psi^1_{pp}(x+h,r) = e^{-\sigma_p\, h}\int_r^\infty dr'\delta_p\; e^{-\sigma x}e^{-\beta(r'+h+x)} \times \int_0^h k_1\; e^{-\alpha(r'+\gamma-r-z)}dz$$

define $\overline{x} \equiv x+h$

$$\psi^1_{pp}(x+h,r) = k_1\delta_p\; e^{-\sigma_p\overline{x}}\;\frac{he^{-\beta(r+\overline{x})}}{(\alpha+\beta)}\left\{\frac{e^{-\alpha\gamma}}{\alpha h}[e^{\alpha h}-1]\right\} \tag{4.3.1.3}$$

Comparison of equation (4.3.1.3) with the δ_p term in (3.9) shows that for $O(h^2)$ accuracy we need γ such that

$$\frac{e^{-\alpha\gamma}}{\alpha h}[e^{\alpha h}-1] = 1+g(h) \tag{4.3.1.4}$$

where $g(h)$ represents a polynomial expansion in powers of h which contains no dependence on powers of h less than quadratic. Recall that

$$e^{ax} = 1+ax+\frac{a^2x^2}{2!}+\frac{a^3x^3}{3!}+\ldots$$

and note that $\alpha h < h < 1$. The curly braces term in equation (4.3.1.3) can be expanded as

$$\frac{1}{\alpha h}[e^{\alpha(h-\gamma)}-e^{-\alpha\gamma}] = \frac{1}{\alpha h}\left[1+\alpha(h-\gamma)+\alpha^2\frac{(h-\gamma)^2}{2!}+\frac{\alpha^3(h-\gamma)^3}{3!}+\ldots -1+\alpha\gamma-\frac{(\alpha\gamma)^2}{2!}+\frac{(\alpha\gamma)^3}{3!}+\ldots\right] \tag{4.3.1.5}$$

This suggests a value of

$$\gamma = \frac{h}{2} \tag{4.3.1.6}$$

Substituting equation (4.3.1.6) into the equation (4.3.1.5) gives

$$\frac{1}{\alpha h}\left[e^{\alpha\frac{h}{2}} - e^{-\frac{\alpha h}{2}}\right] = \frac{1}{\alpha h}\left[1 + \frac{\alpha h}{2} + \frac{1}{2}\left(\frac{\alpha h}{2}\right)^2 + \frac{1}{3!}\left(\frac{\alpha h}{2}\right)^3 + \ldots\right.$$

$$\left. -1 + \frac{\alpha h}{2} - \frac{1}{2}\left(\frac{\alpha h}{2}\right)^2 + \frac{1}{3!}\left(\frac{\alpha h}{2}\right)^3 - \ldots\right] = \left[1 + \frac{1}{24}(\alpha h)^2 + \ldots\right]$$

showing that the choice for γ in equation (4.3.1.6) establishes second order accuracy for equation (4.3.1.3). We use γ to find Q_1^{pp} and Q_2^{pp} for equation (4.1.6). In equation (4.3.1.2) we rearrange variables using

$$r'' = r' + \frac{h}{2} \tag{4.3.1.7}$$

to obtain

$$\psi_{pp}^1(x+h, r) = e^{-\sigma_p h} \int_{r+h/2}^{\infty} dr'' \psi_p^0(x, r'' + \frac{h}{2}) \int_0^h dz \overline{F}_{pp}(r+z, r')$$

$$Q_1^{pp} = \frac{h}{2}, \qquad Q_2^{pp} = \frac{h}{2} \tag{4.3.1.8}$$

The coupled portion of equation (4.3.1.1) is

$$\psi_{pn}^1(x+h, r) = e^{-\sigma_p h} \int_0^h dz \int_r^{\infty} \overline{F}_{pn}(r+z, r' + \gamma_1)\psi_n^0(x, r' + \gamma_2) dr' \tag{4.3.1.9}$$

where γ_1 and γ_2 are constants to be determined. Applying equations (3.1)–(3.7) to (4.3.1.9) gives

$$\psi^1_{pn}(x+h,r) = e^{-\sigma_p h}\int_r^\infty dr''\delta_n\, e^{-\sigma x}e^{-\beta(r''+\gamma_2)} \times \int_0^h dz\; k_2 e^{-\alpha(r''+\gamma_1-r-z)}$$

$$= \delta_n\, k_2 e^{-\sigma_p\bar{x}}\frac{e^{-(\alpha+\beta)r}}{(\alpha+\beta)}e^{\alpha r}e^{-\beta\gamma_2-\alpha\gamma_1}\frac{[e^{\alpha h}-1]}{\alpha}$$

comparing this to the δ_n terms in equation (3.9) gives

$$\psi^1_{pn}(x+h,r) = \delta_n k_2\, e^{-\sigma_p\bar{x}}\,\frac{e^{-\beta(r+h)}}{\beta(\alpha+\beta)}\left[e^{\beta h}-1\right]\left\{\frac{\beta\, e^{\beta h}}{\left[e^{\beta h}-1\right]}\, e^{-\beta\gamma_2-\alpha\gamma_1}\,\frac{\left[e^{\alpha h}-1\right]}{\alpha}\right\} \tag{4.3.1.10}$$

We need γ_1 and γ_2 such that the expression in curly braces can be represented as unity to second order accuracy. Write the curly braces expression as

$$g(h,\gamma_1,\gamma_2) \equiv \left[\frac{\beta}{\alpha}e^{(\beta h-\beta\gamma_2-\alpha\gamma_1}\right]\left[e^{\alpha h}-1\right](e^{\beta h}-1)^{-1} \tag{4.3.1.11}$$

Minimize g with respect to h so that

$$\frac{\partial g(h,\gamma_1,\gamma_2)}{\partial h} = 0 \tag{4.3.1.12}$$

Equation (4.3.1.12) can be written in the form

$$\frac{\partial g}{\partial h} = \frac{\partial}{\partial h}[abc] = ab\frac{\partial c}{\partial h} + ac\frac{\partial b}{\partial h} + bc\frac{\partial a}{\partial h}$$
$$= \frac{\beta}{\alpha}e^{(\beta h-\beta\gamma_2-\alpha\gamma_1)}\left[e^{\alpha h}-1\right]\frac{\partial}{\partial h}(e^{\beta h}-1)^{-1}$$
$$+\frac{\beta}{\alpha}e^{(\beta h-\beta\gamma_2-\alpha\gamma_1)}\left[e^{\beta h}-1\right]^{-1}\frac{\partial}{\partial h}[e^{\alpha h}-1]$$
$$+[e^{\alpha h}-1](e^{\beta h}-1)^{-1}\frac{\partial}{\partial h}\left[\frac{\beta}{\alpha}e^{(\beta h-\beta\gamma_2-\alpha\gamma_1)}\right] = 0$$

we factor out

$$\frac{\beta}{\alpha}e^{(\beta h-\beta\gamma_2-\beta\gamma_1)}\left(e^{\beta h}-1\right)^{-1}$$

to get

$$-\beta e^{\beta h}[e^{\alpha h}-1](e^{\beta h}-1)^{-1}+\alpha e^{\alpha h}$$
$$+[e^{\alpha h}-1]\left(\beta-\beta\frac{\partial\gamma_2}{\partial h}-\alpha\frac{\partial\gamma_1}{\partial h}\right)=0$$

this can be rearranged as

$$\frac{\beta}{1-e^{-\beta h}}-\beta+\beta\frac{\partial\gamma_2}{\partial h}+\alpha\frac{\partial\gamma_1}{\partial h}=\frac{\alpha}{1-e^{-\alpha h}} \tag{4.3.1.13}$$

Let

$$\gamma_1=0 \qquad \gamma_2=h \tag{4.3.1.14}$$

Then equation (4.3.1.13) is

$$\frac{1-e^{-\beta h}}{\beta}=\frac{1-e^{-\alpha h}}{\alpha}$$

using equation (4.3.1.5), this can be expanded to give

$$h-\frac{\alpha h^2}{2}+\frac{\alpha^2 h^3}{6}-\ldots=h-\frac{\beta h^2}{2}+\frac{\beta^2 h^3}{6}-\ldots$$

To within factors of $0(h^2)$ we have the desired identity. Using equation (4.3.1.14) we write (4.3.1.9) as

$$\psi^1_{pn}(x+h,r)=e^{-\sigma_p h}\int_r^\infty \psi^0_n(x,r'+h)dr'\int_0^h dz\,\overline{F}_{pn}(r+z,r') \tag{4.3.1.15}$$

Comparing equation (4.3.1.15) with (4.1.6) gives

$$Q_1^{pn}=0 \qquad Q_2^{pn}=+h \tag{4.3.1.16}$$

4.3.2. Neutron Flux

Using equation (4.1.5) we write (2.5.14) as

$$\psi_n^1(x+h,r) = e^{-\sigma_n h}\int_0^h dz\left\{\int_r^\infty \overline{F}_{nn}(r,r')\psi_n^0(x,r')dr' + \int_r^\infty \overline{F}_{np}(r,r')\psi_p^0(x,r'+h-z)dr'\right\} \tag{4.3.2.1}$$

so that

$$\psi_{nn}^1(x+h,r) = e^{-\sigma_n h}\int_0^h dz\int_r^\infty \overline{F}_{nn}(r,r')\psi_n^0(x,r')dr' \tag{4.3.2.2}$$

using equations (3.1)–(3.7) in (4.3.2.1) gives

$$\psi_{nn}^1(x+h,r) = e^{-\sigma_n h}h\int_r^\infty k_1 e^{-\alpha(r'-r)}\delta_n e^{-\sigma_n x}e^{-\beta r'}dr'$$

$$\psi_{nn}^1(x+h,r) = k_1\delta_n e^{-\sigma_n \bar{x}}\frac{he^{-\beta r}}{(\alpha+\beta)} \tag{4.3.2.3}$$

Equation (4.3.2.2) matches exactly the exact expression for the δ_n term in equation (3.10) so no correction is necessary

$$Q_1^{nn} = 0, \qquad Q_2^{nn} = 0 \tag{4.3.2.4}$$

the coupled portion of equation (4.3.2.1) is

$$\psi_{np}^1(x+h,r) = e^{-\sigma_n h}\int_0^h dz\int_r^\infty dr'\overline{F}_{np}(r,r')\psi_p^0(x,r'+h-z)dr' \tag{4.3.2.5}$$

First move the z dependence from ψ_p^0 to $\overline{F}_{np}$ using

$$r'' = r' + h - z$$

$$\psi^1_{np}(x+h,r) = e^{-\sigma_n h} \int_0^h dz \int_{r+h-z}^{\infty} \overline{F}_{np}(r, r''-h+z)\psi^0_p(x,r'')dr''$$

Replace the $z's$ with constant γ

$$\psi^1_{np}(x+h,r) = e^{-\sigma_n h} \int_0^h dz \int_{r+h-\gamma}^{\infty} \overline{F}_{np}(r, r''-h+\gamma)\psi^0_p(x,r'')dr'' \qquad (4.3.2.6)$$

Applying equations (3.1)–(3.7) to (4.3.2.6) gives

$$\psi^1_{np}(x+h,r) = e^{-\sigma_n h} \int_0^h dz \int_{r+h-\gamma}^{\infty} k_2\, e^{-\alpha(r''-h+\gamma-r)}\delta_p\, e^{-\sigma_n \bar{x}} e^{-\beta(r''+x)} dr''$$

$$= \delta_p k_2 h\, e^{-\sigma_n \overline{x}}\, \frac{e^{-\beta(x+r)} e^{-\beta(h-\gamma)}}{(\alpha+\beta)}$$

comparison with the δ_p term in equation (3.10) gives

$$\psi^1_{np}(x+h,r) = k_2\delta_p\, e^{-\sigma\overline{x}} \frac{e^{-\beta(\overline{x}+r)}}{(\alpha+\beta)} \frac{[e^{\beta h}-1]}{\beta} \left\{ \frac{\beta h e^{\beta\gamma}}{(e^{\beta h}-1)} \right\} \qquad (4.3.2.7)$$

and we require

$$g(h,\gamma) \equiv \frac{\beta h e^{\beta\gamma}}{(e^{\beta h}-1)} = 1 + 0(h^2)$$

minimize equation (4.3.2.7) w.r.t h as

$$\frac{\partial g}{\partial h} = \frac{[e^{\beta h}-1][\beta\, e^{\beta\gamma} + \beta h\, e^{\beta\gamma}\frac{\partial(\beta\gamma)}{\partial h}] - \beta h\, e^{\beta\gamma}[\beta\, e^{\beta h}]}{[e^{\beta h}-1]^2} = 0$$

$$1 + \beta h\, \frac{\partial\gamma}{\partial h} = \frac{\beta h}{1-e^{-\beta h}} = \frac{1}{1-\frac{\beta h}{2}+0(h^2)}$$

so that

$$\left(1+\beta h\frac{\partial\gamma}{\partial h}\right)\left(1-\frac{\beta h}{2}+0(h^2)\right) = 1$$

requiring

$$\gamma = \frac{h}{2} \tag{4.3.2.8}$$

Plugging equation (4.3.2.8) into (4.3.2.6) gives

$$\psi^1_{np}(x+h,r) = e^{-\sigma_n h} \int_0^h dz \int_{r+\frac{h}{2}}^{\infty} \overline{F}_{np}\left(r, r' - \frac{h}{2}\right) \psi^0_p(x,r')dr'$$

or in the form of equation (4.1.6), letting $r'' = r' - \frac{h}{2}$

$$\psi^1_{np}(x+h,r) = e^{-\sigma_n h} \int_0^h dz \int_r^{\infty} \psi_p\left(x, r'' + \frac{h}{2}\right) \overline{F}_{np}(r, r'')dr'$$

so that

$$Q_1^{np} = 0, \qquad Q_2^{np} = \frac{h}{2} \tag{4.3.2.9}$$

The preceding analysis insures second order accuracy in the numerical marching procedure for the secondary particle production terms. In the next section we show that the error terms may be extended to higher order.

4.4 Minimized Truncation Error

In the previous section we obtained values for Q_1^{ji} and Q_2^{ji} by adjusting the function arguments in equation (4.1.5). Following the minimization analysis we compared the solution to the form required by equation (4.1.6) and therefore essentially determined the Q's by inspection.

In this section we will start directly from the form given by equation (4.1.6) and determine Q_1^{ji} and Q_2^{ji} explicitly. We will find that the resulting Q values insure third order accuracy in the production terms. This will minimize the overall second order accuracy of the scheme. Recall the approximate expression for numerical solution of $\psi_j(x,r)$ from equation (4.1.6).

Keeping only the cross terms we write for secondary fluence ψ_j^s

$$\psi_j^s(x+h,r) = \sum_i \int_{r+Q_1^{ji}}^{\infty} \psi_i[x, r' + Q_2^{ji}]dr' \times \int_0^h e^{-\sigma_{jh}} \overline{F}_{ji}(r + \nu_j z, r')dz' \tag{4.4.1}$$

For our purposes it is sufficient to consider the first step h in from the boundary at $x = 0$. Assuming that all δ's can be set to one, we write

$$\psi_p^s(h,r) = \frac{e^{-\sigma_p h}}{\alpha+\beta}\left[e^{-\beta(r+Q_1^{pp}+Q_2^{pp})}k_1 h\frac{e^{-\alpha Q_1^{pp}}}{\alpha h} \times (e^{\alpha h}-1) + e^{-\beta(r+Q_1^{pn}+Q_2^{pn})}k_2 e^{-\alpha Q_1^{pn}}\frac{(e^{\alpha h}-1)}{\alpha}\right] \tag{4.4.2}$$

$$\psi_n^s(h,r) = \frac{e^{-\sigma_{nh}}}{\alpha+\beta}\left[e^{-\beta(r+Q_1^{nn}+Q_2^{nn})}k_1 h e^{-\alpha Q_1^{nn}}) + e^{-\beta(r+Q_1^{np}+Q_2^{np})}k_2 h e^{-\alpha Q_1^{np}}\right] \tag{4.4.3}$$

The corresponding exact solutions from equations (2.5.12) and (2.5.14) using the continuous benchmark cases are given for the first generations as

$$\psi_p^{s(1)}(h,r) = \frac{e^{-\sigma_{ph}}}{\alpha+\beta}e^{-\beta(h+r)}\left[k_1 h + k_2\frac{(e^{\beta h}-1)}{\beta}\right] \tag{4.4.4}$$

$$\psi_n^{s(1)}(h,r) = \frac{e^{-\sigma_{nh}}}{\alpha+\beta}e^{-\beta r}\left[k_1 h + k_2\frac{(1-e^{-\beta h})}{\beta}\right] \tag{4.4.5}$$

The (n,p) cross terms from equations (4.4.3) and (4.4.5) compare as

$$\psi_{np}^{\text{Num}} = \frac{e^{-\sigma_{nh}}}{(\alpha+\beta)}k_2\, e^{-\beta r}\left\{h\, e^{-\beta(+Q_1+Q_2)}e^{-\alpha Q_1}\right\} \tag{4.4.6}$$

$$\psi_{np}^{\text{exact}} = \frac{e^{-\sigma_{nh}}}{(\alpha+\beta)}\, k_2\, e^{-\beta r}\left\{\frac{(1-e^{-\beta h})}{\beta}\right\} \tag{4.4.7}$$

where the superscripts on Q have been dropped for notational convenience. Note the differences between equations (4.4.6) and (4.4.7) in curly braces. Expanding the braces in equation (4.4.6) gives

$$h\, e^{-\beta Q_2 - \alpha Q_1 - \beta Q_1} = h[1 - (Q_1 + Q_2)\beta + \frac{1}{2}(Q_1 + Q_2)^2\beta^2 + \ldots] \times [1 - Q_1\alpha + \frac{1}{2}Q_1^2\alpha^2 + \ldots \tag{4.4.8}$$

Expanding the braces in equation (4.4.7) gives

$$\frac{1 - e^{-\beta h}}{\beta} = h\left[1 - \frac{1}{2}\beta h + \frac{1}{6}\beta^2 h^2 + \ldots\right] \tag{4.4.9}$$

comparing equations (4.4.8) and (4.4.9) shows that the choice of

$$Q_1 + Q_2 = \frac{1}{2}h$$

and

$$Q_1 = 0 \qquad Q_2 = \frac{1}{2}h \tag{4.4.10}$$

gives

$$\psi_{np}^{\text{num}} = \psi_{np}^{\text{exact}} - \frac{1}{24}\beta^2 h^3$$

This result shows that the choices for Q in equation (4.3.2.9) satisfy second and third order accuracy.

The (p, n) cross terms from equations (4.4.2) and (4.4.4) are

$$\psi_{np}^{\text{num}} = \frac{k_2 e^{-\sigma_p h}}{\alpha + \beta} e^{-\beta\tau}\left[e^{-\beta(Q_1+Q_2)} e^{-\alpha Q_1}\frac{(e^{\alpha h} - 1)}{\alpha}\right] \tag{4.4.11}$$

$$\psi_{pn}^{\text{exact}} = \frac{k_2 e^{-\sigma_p h}}{\alpha + \beta} e^{-\beta\tau}\left[\frac{e^{\beta h}(e^{\beta h} - 1)}{\beta}\right] \tag{4.4.12}$$

The differences between equations (4.4.11) and (4.4.12) lie in the square brackets. Expanding the bracketed terms in equation (4.4.11)

$$e^{-\beta(Q_1+Q_2)}e^{-\alpha Q_1}\frac{(e^{\alpha h}-1)}{\alpha} = e^{-\beta(Q_1+Q_2)}\frac{1}{\alpha}$$
$$\times\left[1+\alpha(h-Q_1)+\frac{1}{2}\alpha^2(h-Q_1)^2+\frac{1}{6}\alpha^3(h-Q_1)^3\right.$$
$$+\ldots-1+\alpha Q_1-\frac{1}{2}\alpha^2Q_1^2$$
$$\left.+\quad\frac{1}{6}\alpha^3Q_1^3+\ldots\right] \tag{4.4.13}$$

For

$$Q_1=\frac{h}{2} \tag{4.4.14}$$

this is

$$=\frac{e^{-\beta(Q_1+Q_2)}}{\alpha}\left(\alpha h+\frac{1}{3}\alpha^3\frac{h^3}{2^3}+\ldots\right)$$

and then for

$$Q_2=0 \tag{4.4.15}$$

$$=\left(h-\frac{\beta h^2}{2}+\frac{1}{2}\beta^2\frac{h^3}{4}+\ldots\right)\left(1+\frac{1}{48}\alpha^2h^2+\ldots\right) \tag{4.4.16}$$

and the square bracketed term in equation (4.4.12) is

$$e^{-\beta h}\frac{(e^{\beta h}-1)}{\beta}=\frac{1-1+\beta h-\frac{1}{2}\beta h^2+\ldots}{\beta}=h-\frac{1}{2}\beta h^2+\frac{1}{6}\beta^2h^3+\ldots \tag{4.4.17}$$

Equations (4.4.16) and (4.4.17) show that the choices for Q in equations (4.4.14) and (4.4.15) result in third order accuracy for the (n,p) cross terms.

Further analysis shows that the second order accurate choices for Q in the (p,p) and (n,n) terms also result in third order accuracy. The choices of Q_1^{ji} and Q_2^{ji} for second and third order accuracy are summarized in tables 2 and 3.

Equation (4.1.6) is evaluated numerically by establishing an x-grid at which $\psi_j(x_m,r)$ is evaluated where h is the distance between each successive evaluation. The integral over r' is accomplished by establishing an r-grid (and the corresponding E grid) and using[13]

$$\int_{rn}^{\infty}K(r_n,r')\psi_j(x_m,r')dr'\approx\sum_{l=n}^{\infty}K_n(r_n,\overline{r}_\ell)\int_{r_\ell}^{r_{\ell+1}}\psi_j(x_m,r')dr' \tag{4.4.18}$$

Table 1. Composition of Tissue

Element	Number Density of Nuclei (No. cm^{-3})
H	6.265×10^{22}
C	9.398×10^{21}
N	1.342×10^{21}
O	2.551×10^{22}

Table 2 - Values of Q_1 and Q_2 to Insure Second-Order Accuracy

(j,i)	(p,p)	(p,n)	(n,p)	(n,n)
Q_1	$\frac{h}{2}$	0	0	0
Q_2	$\frac{h}{2}$	h	$\frac{h}{2}$	0

Table 3 - Values of Q_1 and Q_2 to Minimize Second-Order Terms

(j,i)	(p,p)	(p,n)	(n,p)	(n,n)
Q_1	$\frac{h}{2}$	$\frac{h}{2}$	0	0
Q_2	$\frac{h}{2}$	0	$\frac{h}{2}$	0

where

$$\overline{r}_\ell = (r_\ell + r_{\ell+1})/2$$

and the series terminates at the highest ℓ value in the r-grid which is related to the maximum energy cutoff $r_{\max}$. The approximation in equation (4.4.18) is appropriate for physical processes in which the kernal K_n is a slowly varying function of r'.

Applying equation (4.4.18) to equation (4.1.6) leads to a sequence of interpolations[105] and integrations. Work performed over many years of solving for space related fluences suggests that Lagrange interpolation schemes are optimal for this class of problems.[106] We currently use third-order Lagrange with four neighboring points placed evenly on both sides of the interpolated point. Cubic splines were used in earlier work and, while more accurate in general, they are computationally expensive. They also exhibit characteristic excursions (oscillations) which can lead to unpredictable erroneous solutions.[106]

In the next chapter we apply the numerical marching scheme to space transport problems.

5. Space Radiation Applications

In Chapter 4 we developed a second order accurate numerical marching procedure for the transported fluence. Our production operator term is accurate to the third order which has the effect of miminizing the overall second order solution.

The numerical marching procedure for nucleon transport using 1-D Boltzmann equation solution has been incorporated into a computer program called BRYNTRN[13] (Baryon Transport). BRYNTRN incorporates a sophisticated database of the atomic and nucleon interactions important for high energy nucleon transport, but pion production is presently ignored. This leads to small errors in dose calculation for nucleon kinetic energy above 400 MeV. Nuclear crossection data for most types of target nuclei are included as fits to experimental data or Monte Carlo models. Fits to Bethe theory for $S_p(E)$ are included. Target fragmentation and recoil dose can be computed. The nonelastic spectra are represented as

$$\overline{F}_{ji}(E,E') = \sum_{k=1}^{3} \frac{N_k}{\alpha_k} \frac{\exp(-E/\alpha_k)}{1-\exp(-E'/\alpha_k)} + \frac{N_Q}{E'}\left\{1+\exp\left[-20(1-E/E')\right]\right\} \tag{5.1}$$

where the first term of the sum has N_1 representing the evaporation multiplicity and $N_2+N_3+N_Q$ is equal to the cascade multiplicity of Bertini.[77] The quasi elastic multiplicity N_Q was evaluated by Wilson[13] and N_2 is taken from Ranft[107] as are the α's. BRYNTRN accepts any user specified incident spectrum. For our purposes the code is setup for a slab geometry although any number of layers of varying shield type and thickness may be specified. A computational grid in space and energy is established according to user requirements. Typically the space coordinates are evenly spaced and the energy grid is stretched using a log scaling to concentrate points at low energies.

We have modified BRYNTRN to accept either the second or third order accurate Q_1^{ji} and Q_2^{ji} values in tables 2 and 3. Test cases have been run to calculate dosimetric and fluence quantities within a 30 cm tissue slab shielded by 20, 50, and 100 gm/cm^2 of Aluminum.

Cases have also been run for lead shields. The tissue constituents are given in table 1.

We have used a typical solar cosmic ray spectrum for the incident proton flux (p/cm^2) given by[104,108]

$$\phi_p(0,E) = 10^7 \exp\left[\frac{239.1 - P(E)}{P_o}\right] \frac{(E + 938.)}{P(E)} \tag{5.2}$$

This is called the Webber spectrum. E is the proton energy (MeV), ϕ_p is the proton fluence, $P(E) = \sqrt{E(E + 1876)}$ and P_0 is the proton rigidity (momentum per unit charge). In our case $P_0 = 100$ MV. Figure 13 shows the characteristic exponential attenuation of primary protons in the tissue slab. We note that in evaluating the energy absorbed in dose, the transfer of neutron kinetic energy into proton energy is treated explicitly in the formalism. That is neutrons may create protons in nuclear collisions which subsequently deposit dose. Energy expended in producing other charged particles is assumed to be in equilibrium with the local collision density.[109,110] In other words, target fragmentation dose is included but the fragments are not transported. For our chosen shield thicknesses it can be seen that the initial tissue dose ($x = 0$) varies by approximately one decade per case. Note that the dose unit[9] is the Gray (Gy) defined as the energy deposition of 1 Joule in 1 kg of material. The older unit was the Rad, defined as 100 ergs energy deposition per gram of absorber material. Therefore in Aluminum 100 Rad (Al)= 1 Gy (Al). Figures 14–16 show the secondary proton dose in tissue. This dose comes from contributions to the secondary proton fluence by both proton and neutron collisions with the tissue media. The figures compare the choices for Q_1 and Q_2 resulting from the second order parameters of table 2 and the third order parameters of table 3. The calculations of the two methods differ in the aluminum/tissue interface region. The differences widen with increasing shield thickness. The tissue dose features an initial "shoulder" followed by a monotonic decrease. The second order method preserves the dose curve shape but consistently underestimates its magnitude. Comparison of table 2 with table 3 shows that the dose differences relate to the Q_1, Q_2 values for the (p,n) term. A comparison between the magnitudes in figures 13 and 14–16 shows that, for a given case, the primary dose dominates the secondary dose. Given this result, why is

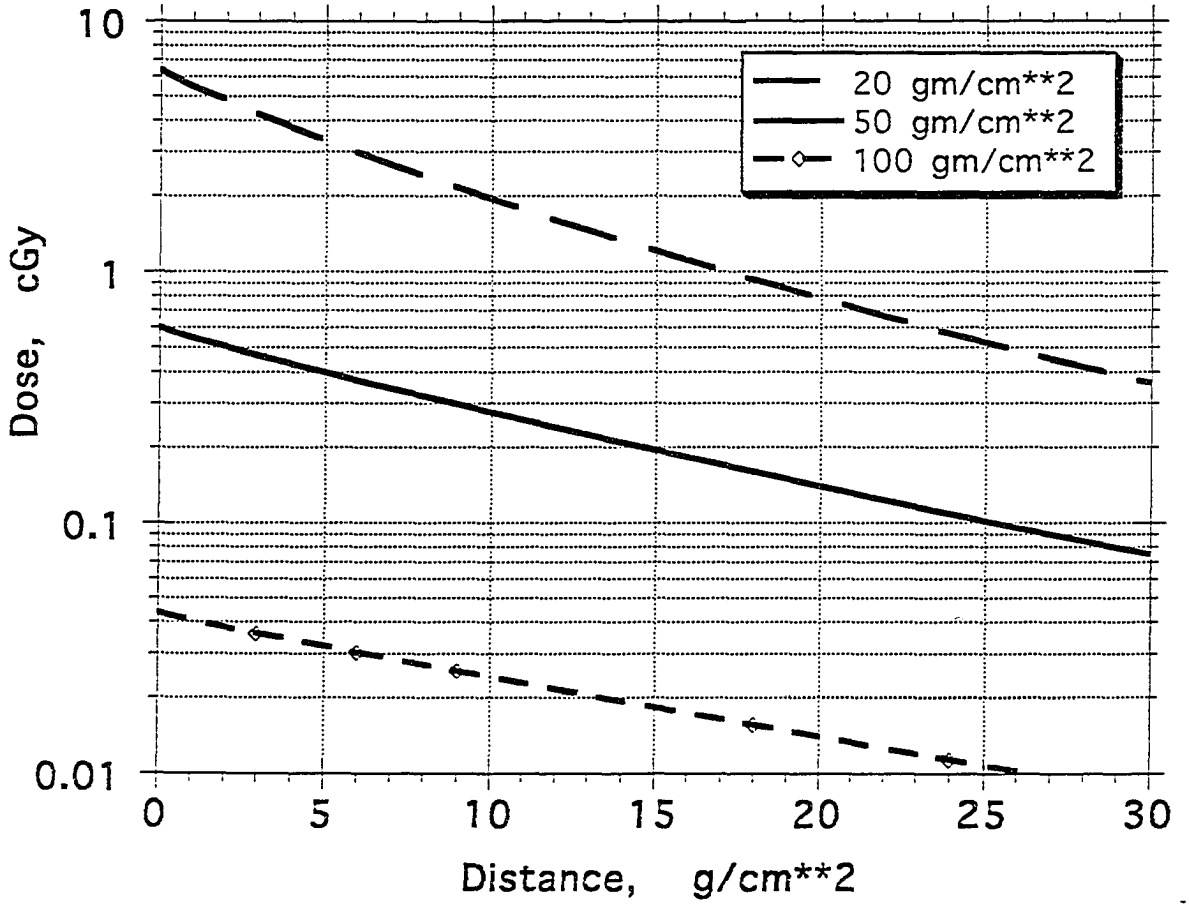

Fig. 13 Primary Proton Dose in Tissue Slab Behind Various Depths of Aluminum Shield

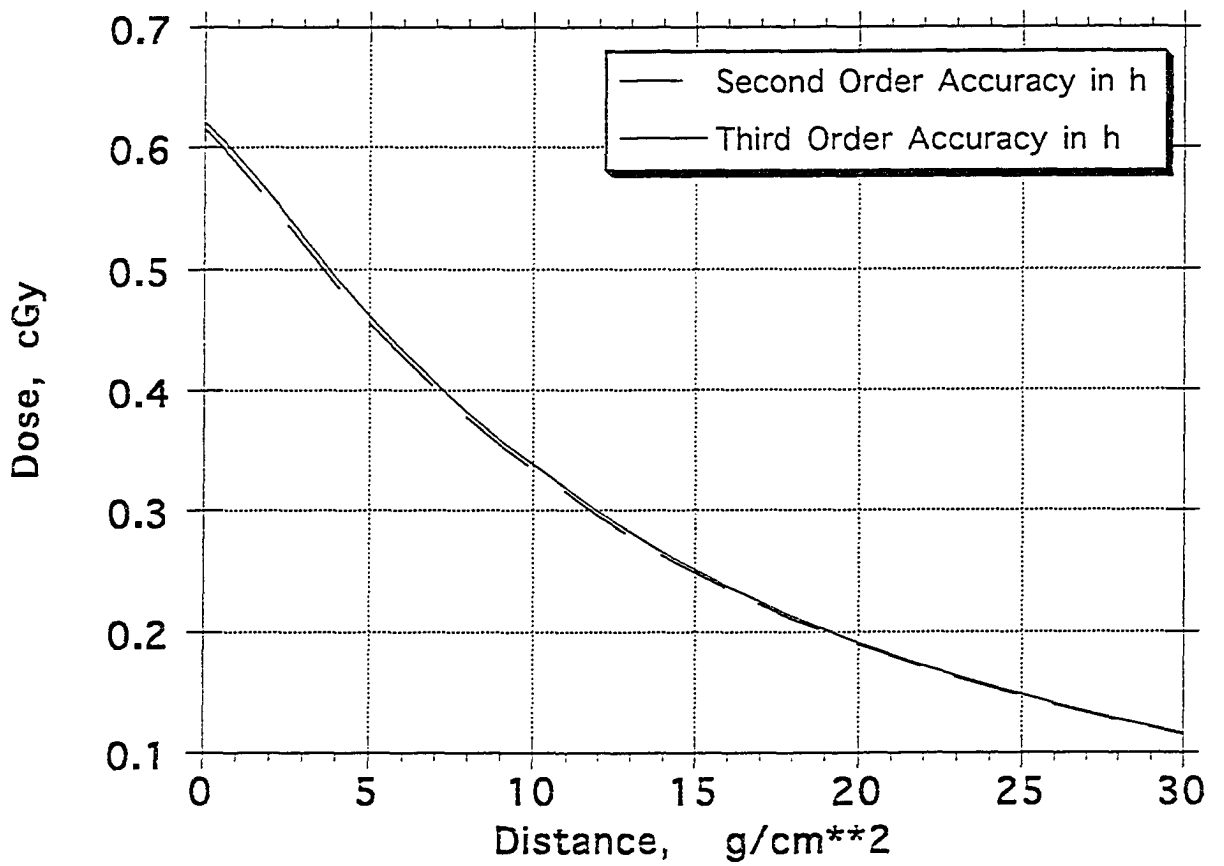

Fig. 14 Secondary Proton Dose in Tissue Slab Behind a 20 g/cm**2 Aluminum Shield

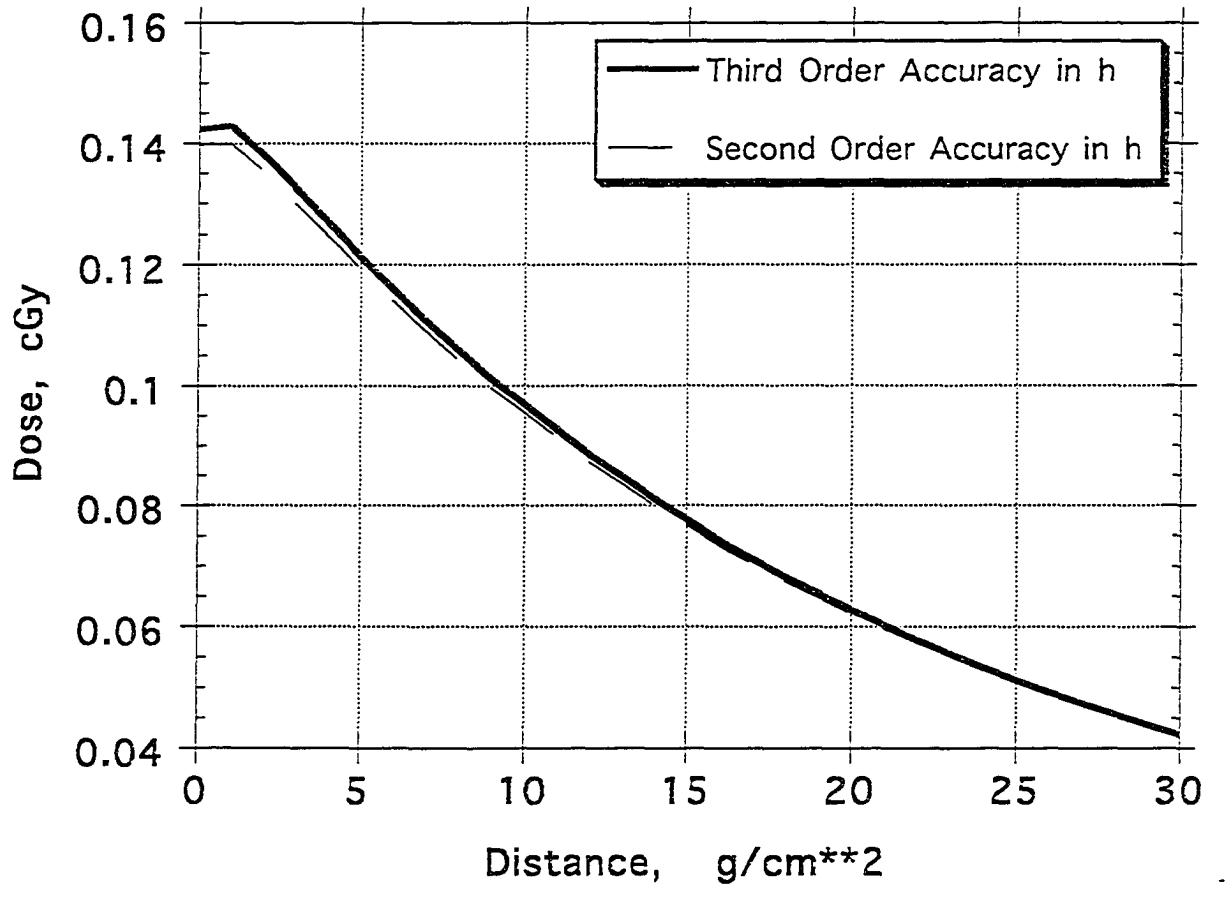

Fig. 15 Secondary Proton Dose in Tissue Slab Behind 50 g/cm**2 Aluminum Shield

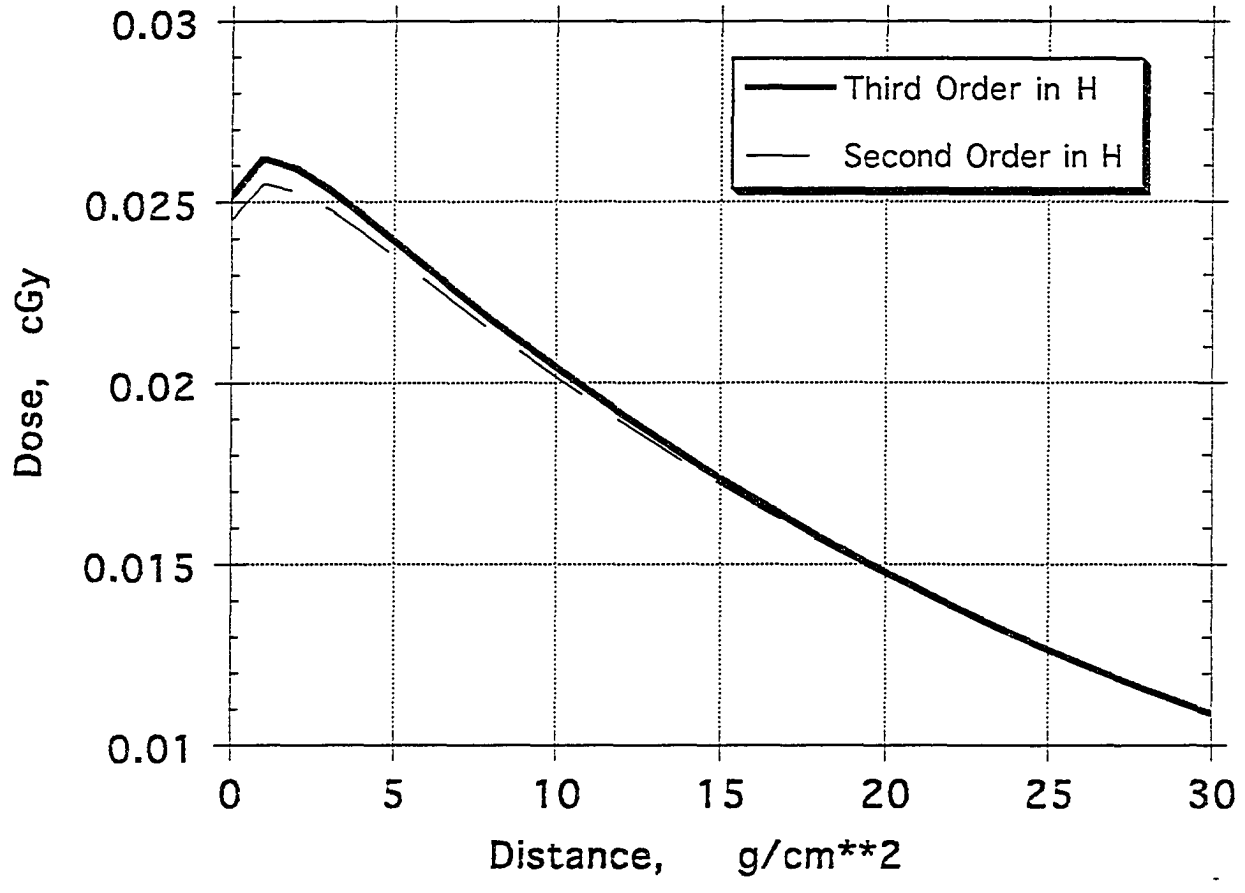

Fig. 16 Secondary Proton Dose in Tissue Slab Behind a 100 g/cm**2 Aluminum Shield

calculation of the secondary fluence considered to be important? The absorbed dose is a gross volumetric quantity which is of limited use to estimating biological exposures in humans and single-event-upset (SEU) occurrences in electronic curcuits. It is also the case that secondary fluence and, consequently the dose, becomes very important for deep penetration. Figures 13 and 14–16 show, for example, that while the ratio of primary to secondary tissue dose is about 13 for the 20 gm/cm^2 shield case it is only about two for the 100 gm/cm^2 shield. These comparisons are made at the tissue boundary. If we examine the ratio at a tissue penetration of 25 cm we find that the ratio is about 0.5. This dependence on penetration depth is related to the growth of secondary neutrons which can, in turn, repopulate the declining proton flux through nonelastic nuclear collisions. For 50 gm/cm^2 of shielding some corresponding proton spectra near the interface for the methods associated with tables 2 and 3 are shown in figures 17 and 18. The spectra are little affected at energies above 100 MeV. Rather large shifts in the spectrum are observed below 50 MeV even several centimeters from the interface. These differences clearly result from second order errors introduced by table 2 which are not present in the choice of table 3 parameters. Figure 19 illustrates these differences at a penetration depth of 2 g/cm^2 in tissue behind a 50 g/cm^2 Aluminum shield. We can gain further insight regarding the behavior of particle transport near the shield tissue interface region by plotting the low energy spectra of $\psi_p(x_m, E) = S_p(E)\phi(x_m, E)$ at selected values of x_m. Figure 20 shows ψ_p in tissue behind a 50 gm/cm^2 aluminum shield at energies 0–4 MeV. Below 1 MeV the fluence is dominated by the fluence at $x = 1$. Beyond a few MeV however the $x = 2$ and $x = 3$ spectra overtake the $x = 1$ values. The spectra for $x = 6$ are lower than all other positions for every energy value. Figures 21–22 show a similar effect for the integrand spectra of the dose equivalent DE_p where

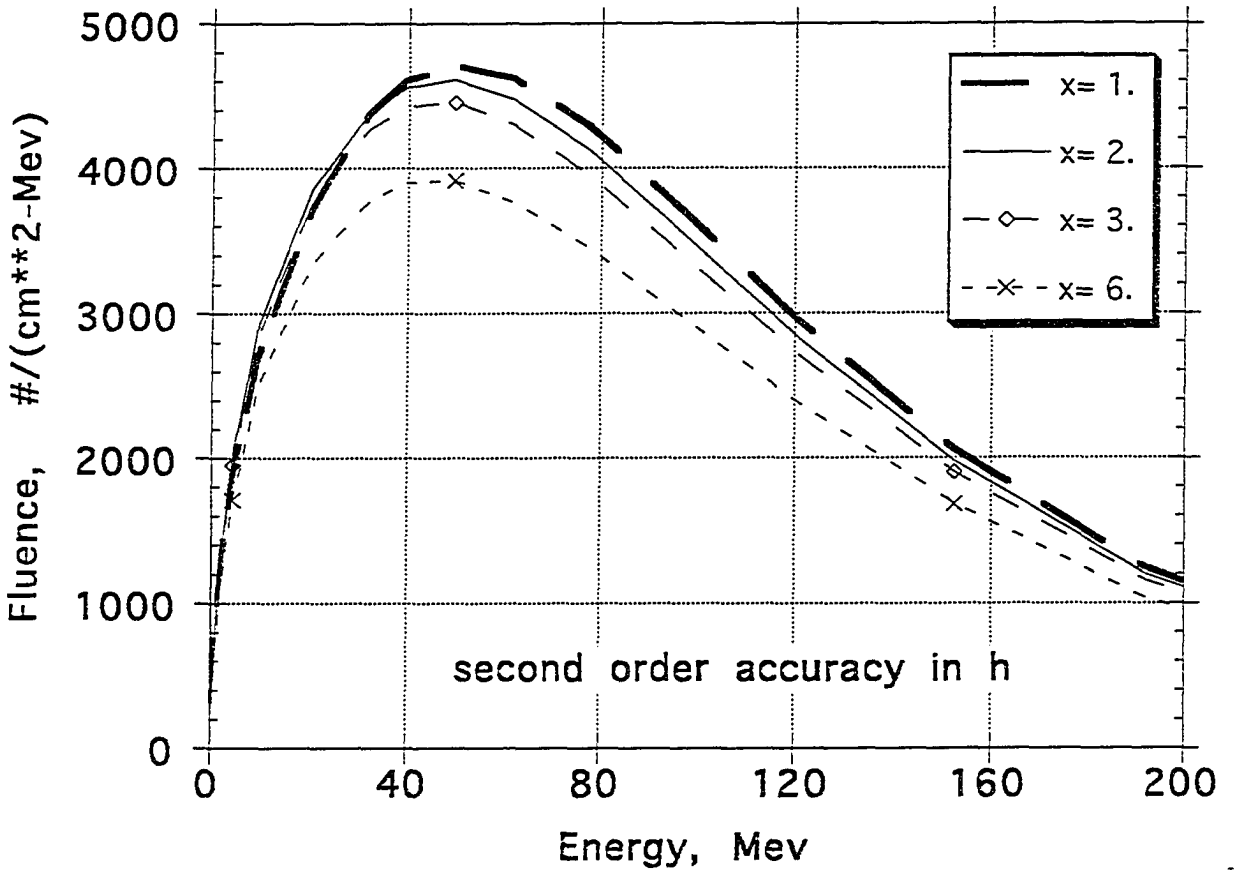

Fig. 17 Secondary Proton Fluence in Tissue Slab Behind a 50 g/cm**2 Aluminum Shield

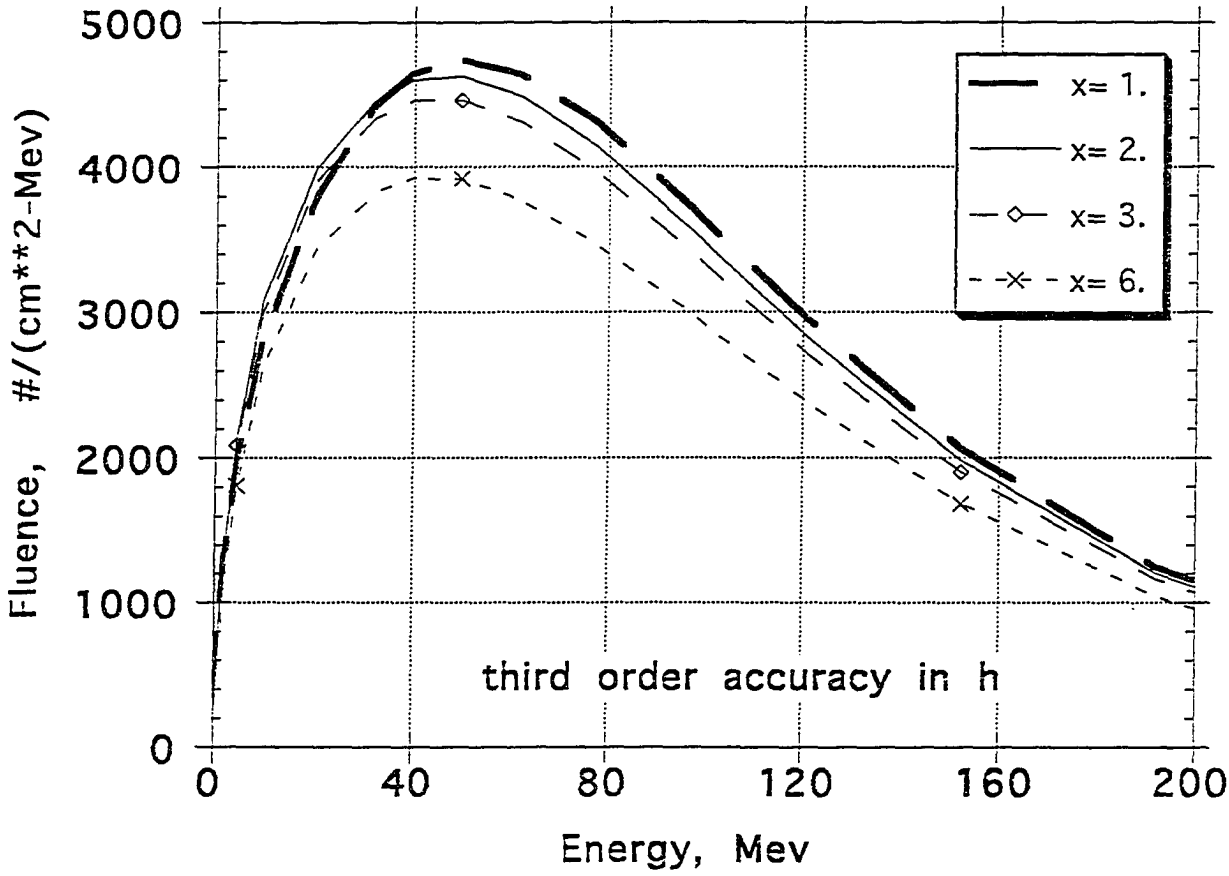

Fig. 18 Secondary Proton Fluence in Tissue Slab Behind a 50 g/cm**2 Aluminum Shield

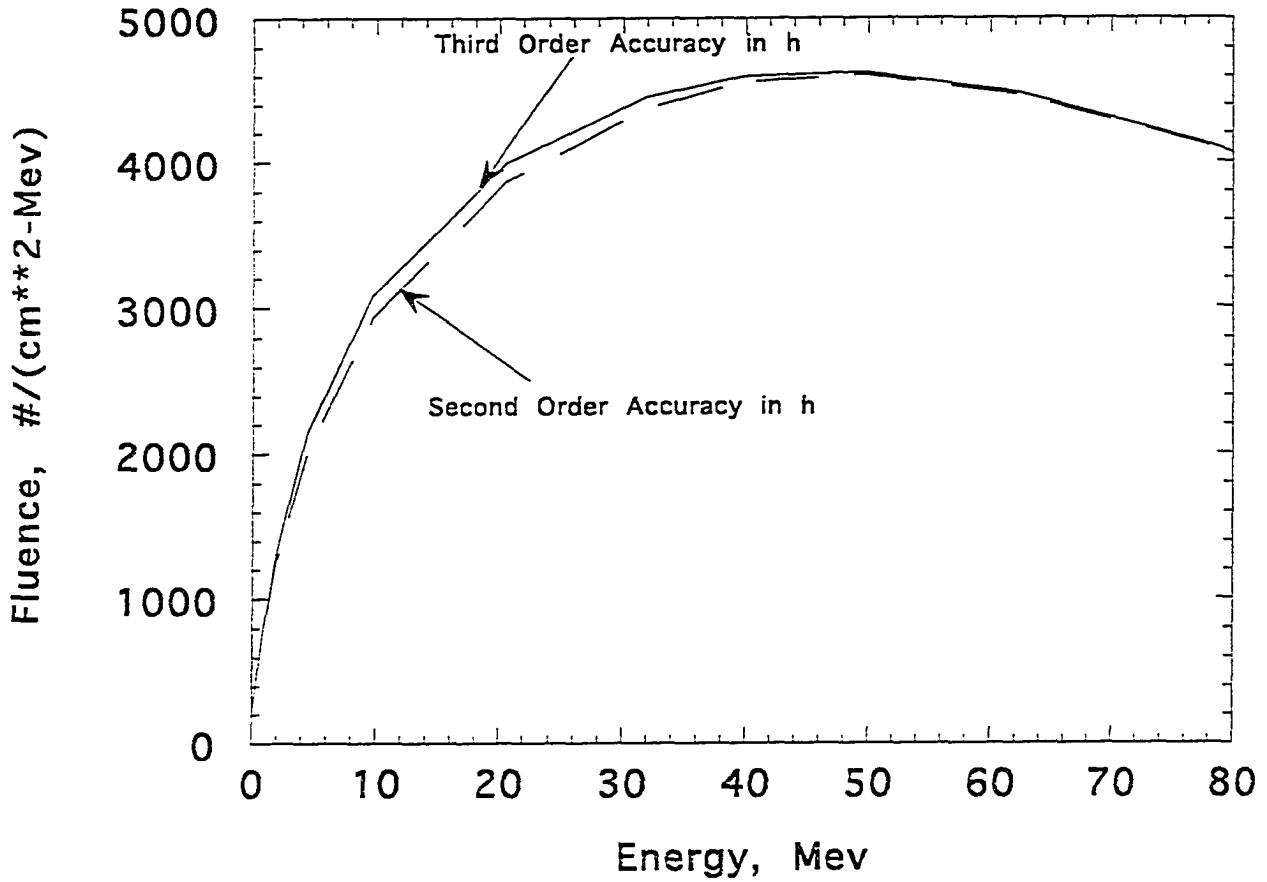

Fig. 19 Secondary Proton Fluence in Tissue at x= 2 cm(50 g/cm**2 Aluminum Shield)

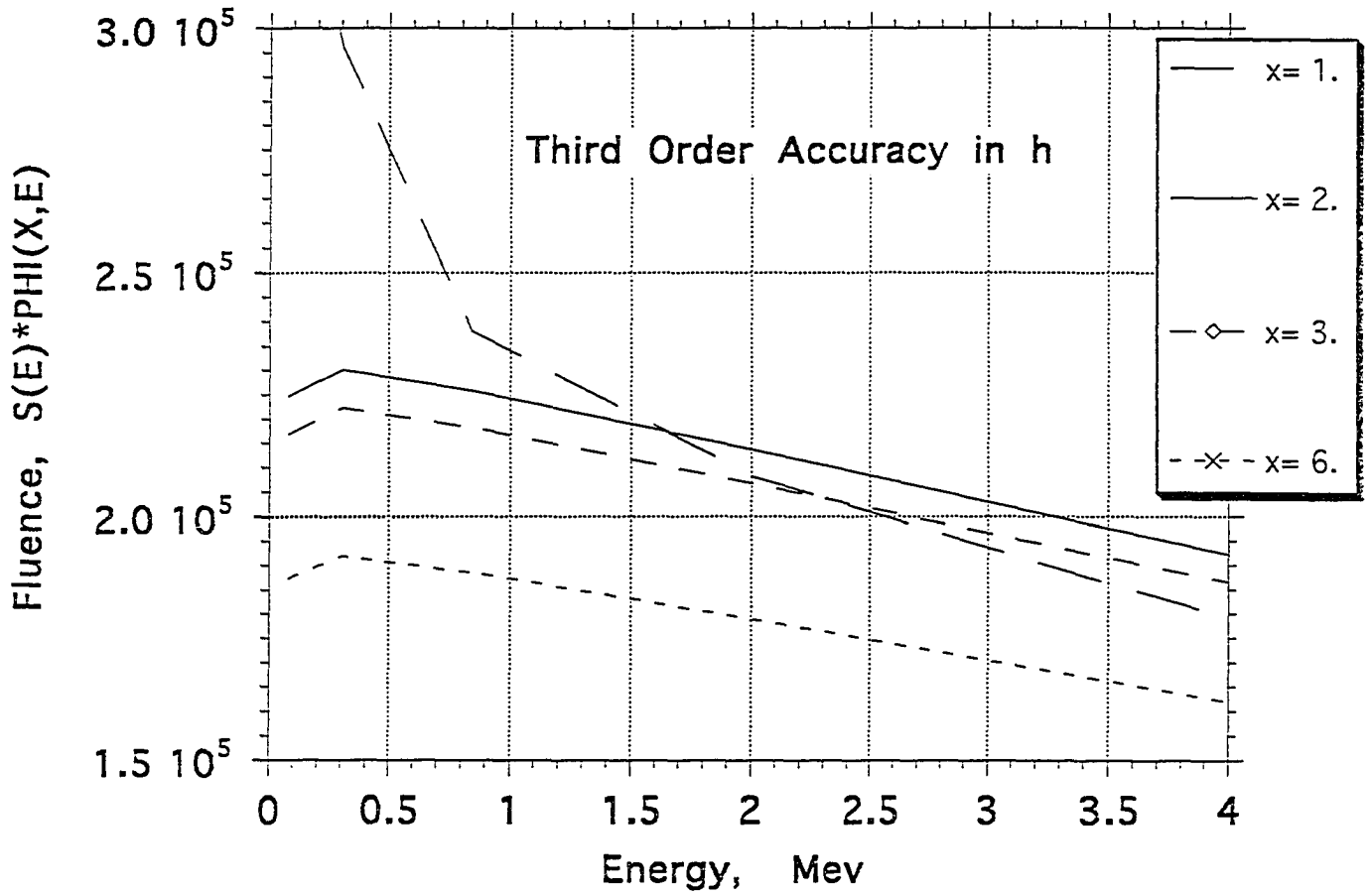

Fig. 20 Secondary Proton Fluence in Tissue Slab at various Depths Behind a 50 g/cm**2 Aluminum Shield

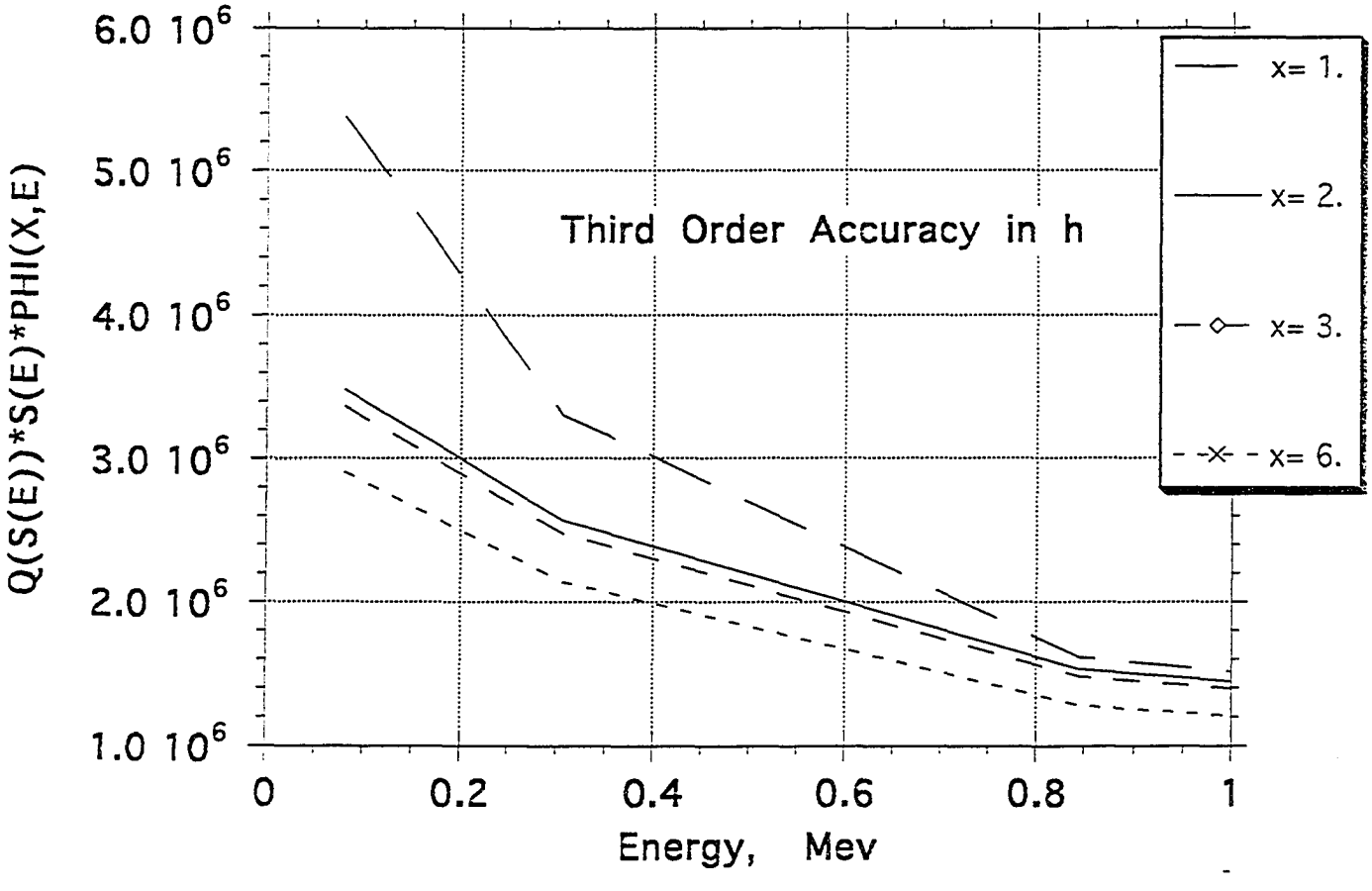

Fig. 21 Secondary Protons in Tissue Slab at Various Depths Behind a 50 g/cm**2

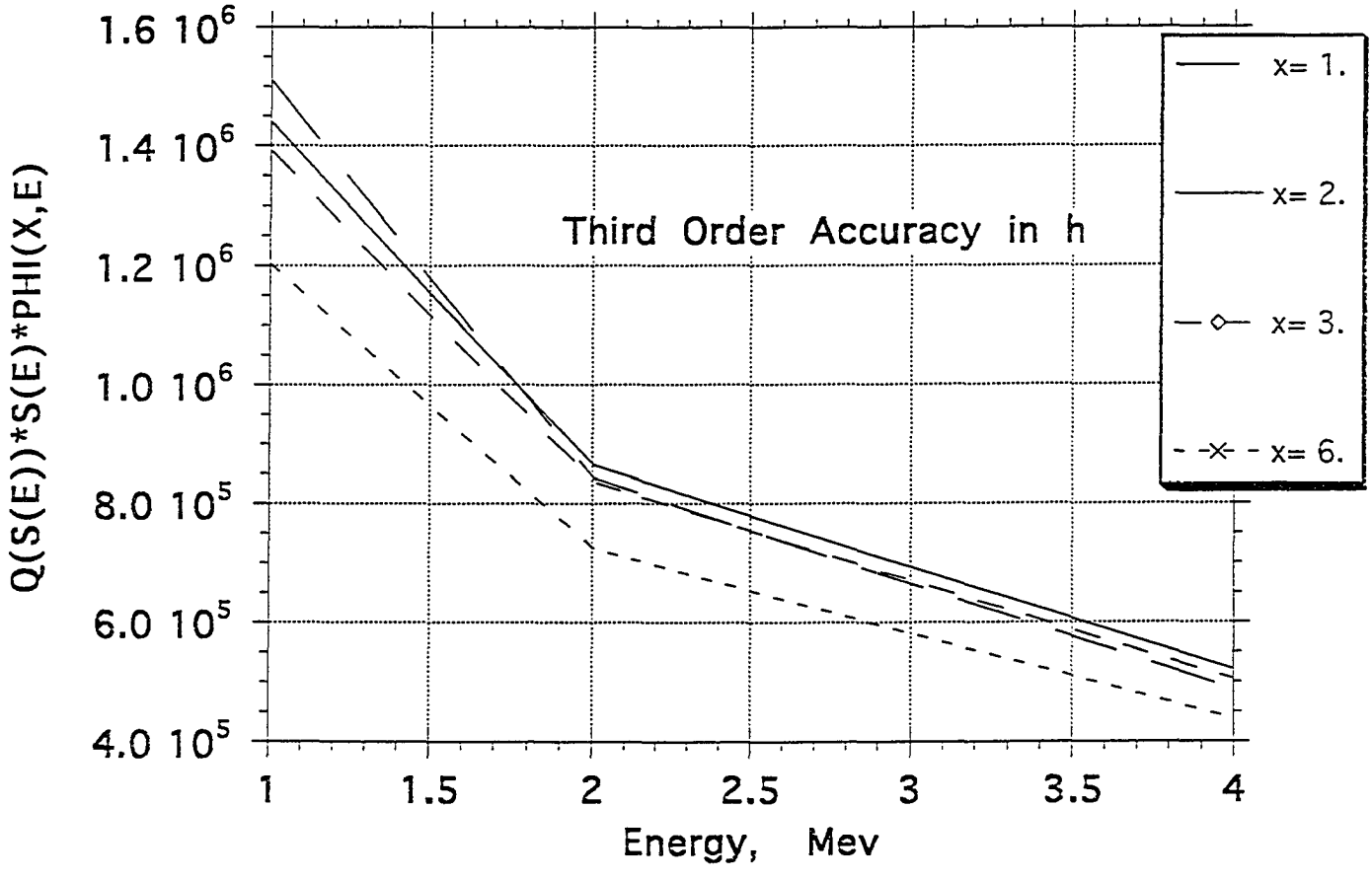

Fig. 22 Secondary Protons in Tissue Slab at Various Depths Behind a 50 g/cm**2 Aluminum Shield

$$DE_p(x,E) = \int_0^E Q\left[S_p(E)\right]\psi_P(x,E')dE'$$
$$= \int_0^E Q\left[S_p(E)\right]S_p(E')\phi(x,E')dE' \qquad (5.3)$$

The unit for dose equivalent is the Sievert. This replaces the REM unit. The conversion is 100 REM = 1 Sv. Q is the quality factor which serves as a weighing factor in human exposure. That is, the high LET portion of the spectrum is most damaging to tissue. The high values for $S_P(E)$ are at low values of E. Figure 23 shows the integrated dose equivalent in tissue behind a 50 gm/cm^2 aluminum shield. Note the absence of the shoulder seen in the dose calculation. It can also be seen that the order differences are most pronounced for tissue penetration depths $\leq$ 5 gm/cm^2. In addition to the order of accuracy in h we can also observe the effect of changing the value of h. Figure 24 shows the effect of halving spacing h from .5 to .25. We see the spectra at a tissue penetration depth of 2 gm/cm^2 behind an aluminum shield of 100 gm/cm^2. The h = .5 case under predicts the h = .25 result in the energy region $\leq$ 20 MeV.

The present solution using table 3 is compared to results of Monte Carlo calculations[111] in figures 25–27. The total dose in tissue behind the 20 g/cm^2 aluminum shield is shown in figure 25. The growing discrepancy beyond 20 g/cm^2 of tissue is due to a 400 MeV limit on the Monte Carlo spectrum (the older NTC[79] code was used for which pion production was not yet added) as can be seen by comparing the transmitted primary proton dose in figure 27. Also shown in figure 25 is the dose calculated using the Buildup-Factor[6] method with and without a 400 MeV cutoff applied. The Buildup-Factor uses a parametric equation to calculate the dose due to secondary particle generations. The secondary proton dose is shown in figure 26. Clearly the BRYNTRN results are within the statistical fluctuations of the Monte Carlo calculation. We note that Monte Carlo benchmarks[5] have been published

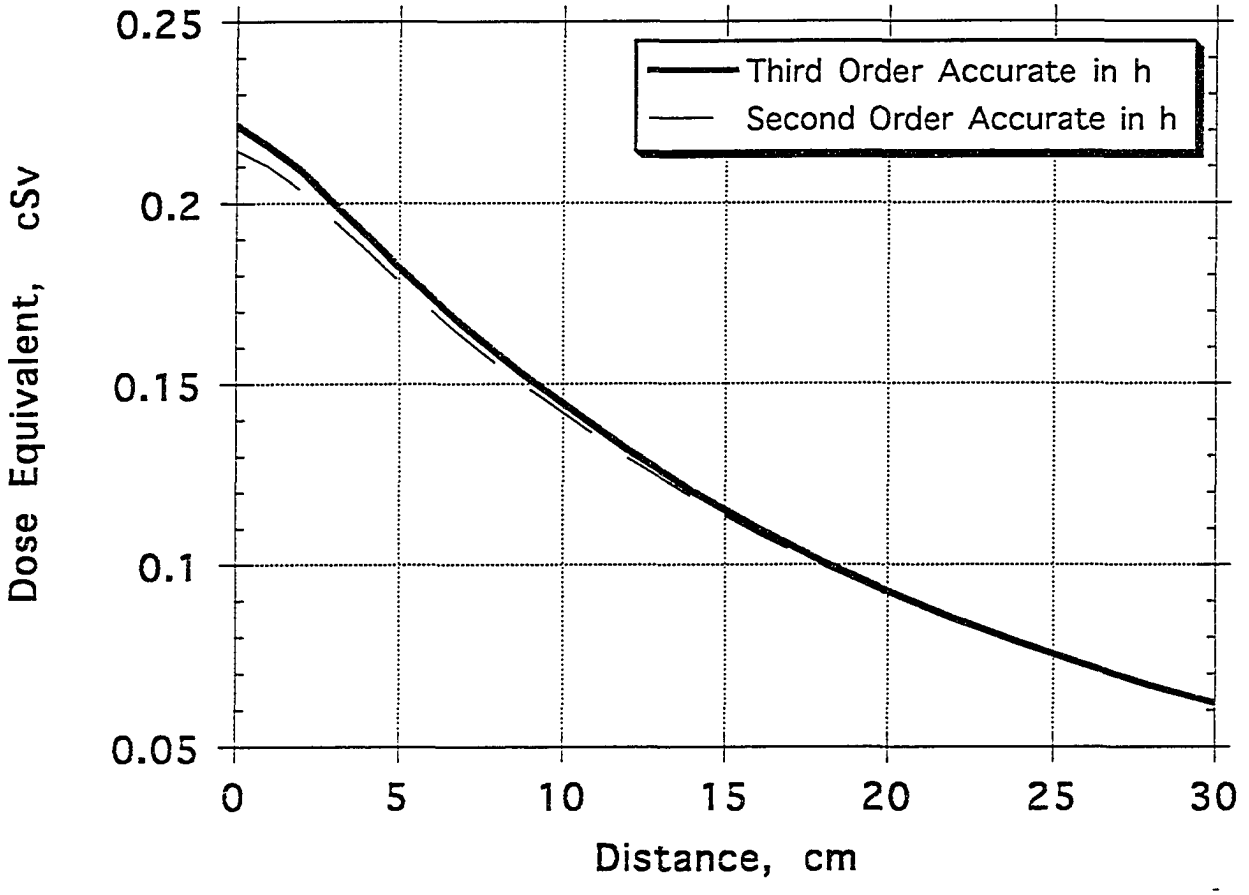

Fig. 23 Secondary Proton Dose Equivalent in Tissue Slab Behind 50 g/cm**2 Aluminum Shield

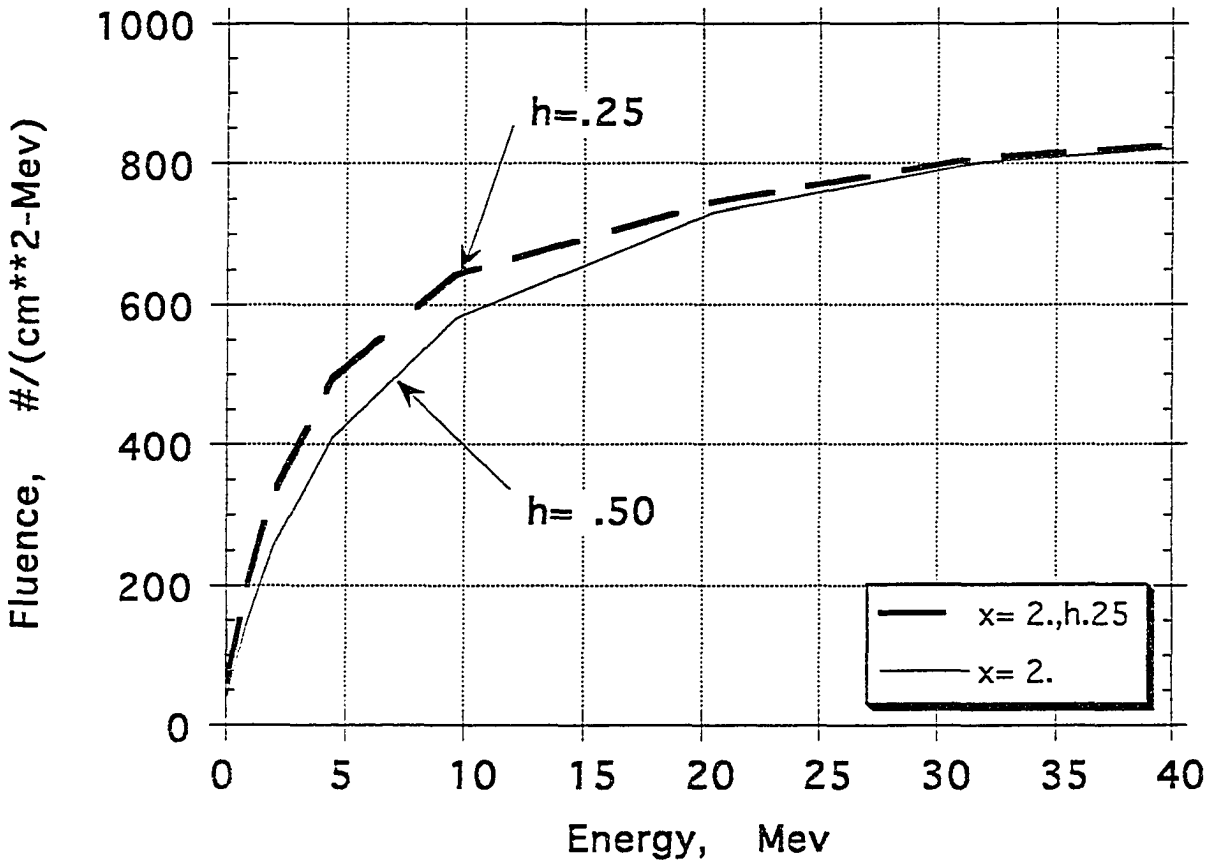

Fig. 24 Secondary Proton Fluence in Tissue Behind 100 gm/cm**2 Aluminum Shield. Third Order Accuracy in h

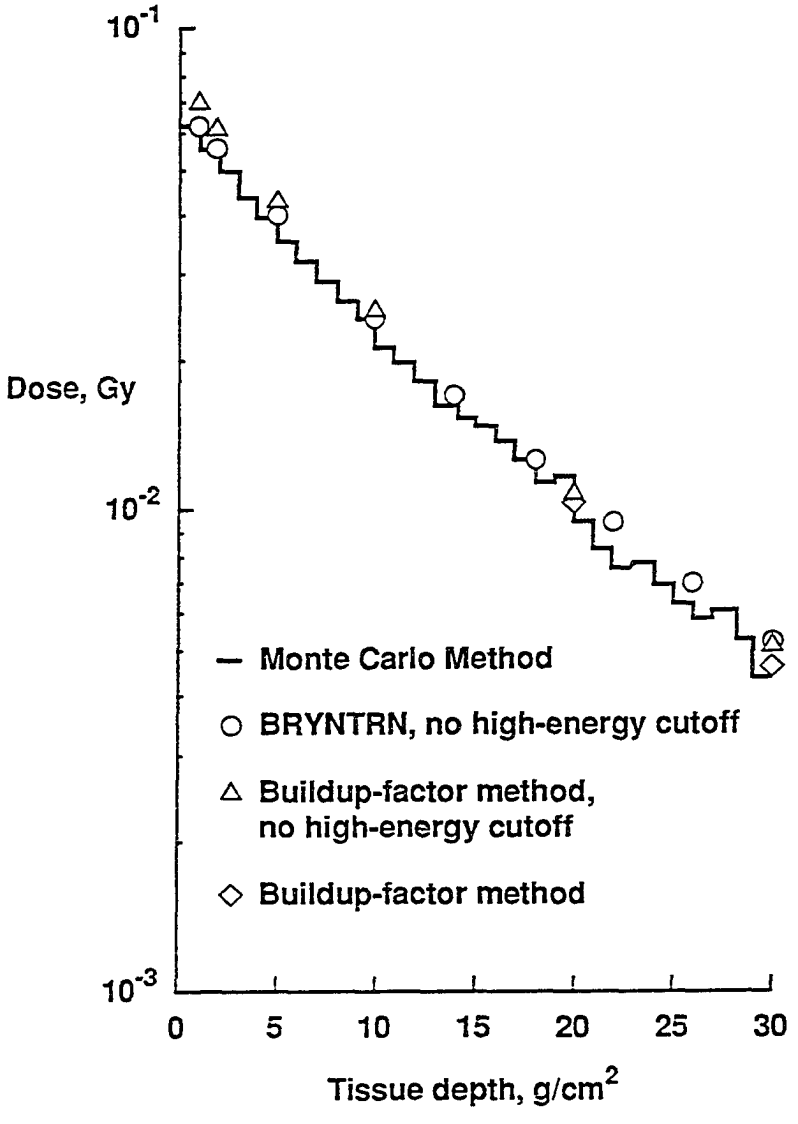

Fig 25 Total dose in tissue behind 20 g/cm^2 of aluminum shield to normal incidence of a solar flare proton spectrum of Webber form with rigidity equal to 100 MV.

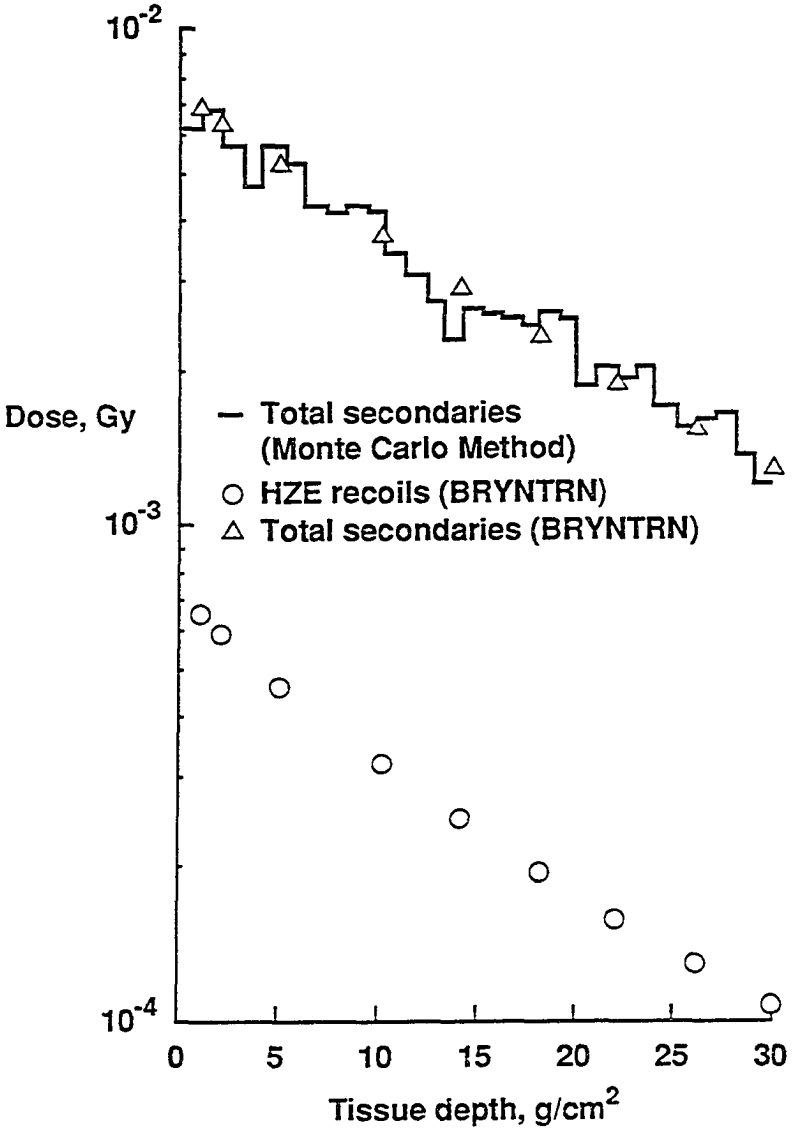

Fig 26 Total secondary and heavy ion recoil dose in tissue behind 20 g/cm^2 of aluminum shield to normal incidence of a solar flare proton spectrum of Webber form with rigidity equal to 100 MV.

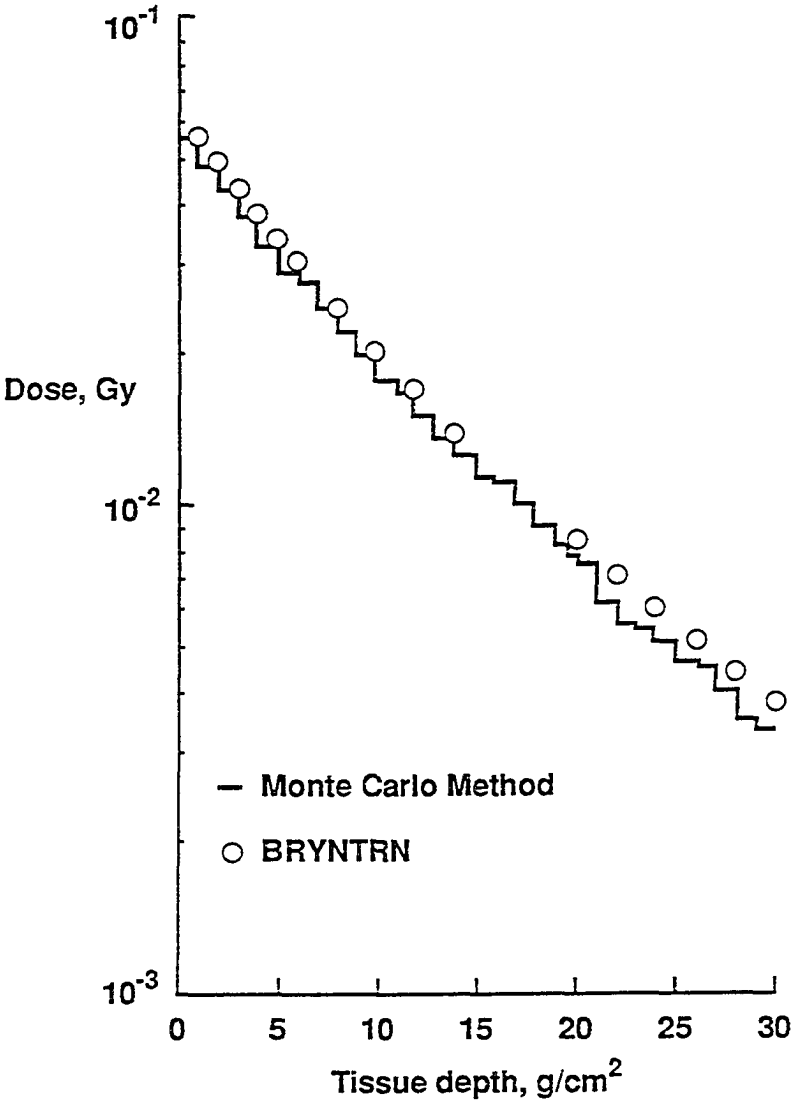

Fig 27 Primary proton dose in tissue behind 20 g/cm^2 of aluminum shield to normal incidence of a solar flare proton spectrum of Webber form with rigidity equal to 100 MV.

(This page intentionally blank)

which do not restrict incident energies to below 400 MeV. The later benchmarks, however, do not feature the slab geometry with aluminum shielding used in our analysis.

A shoulder was observed in figures 15–16. This effect may be attributed to the change in the neutron fluence as it enters the hydrogenic tissue followed by establishment of a new equilibrium between neutron and proton collisions. In figures 28 and 29 we show the integral fluence for solar cosmic rays in 100 g/cm^2 aluminum and lead shields followed by 30 cm tissue slabs. The integral fluence for nucleon type j is given by

$$I_j(x) = \int \psi_j(x,r)\, dr \tag{5.4}$$

$I_j(x)$ exhibits a rapid rise peaking between 5–10 g/cm^2. Neutron fluence is substantially greater than proton fluence, even though the incident spectrum contained no neutral particles. This is entirely due to the electronic slowing down exhibited by protons. Both particle fluences decay with penetration distance, eventually reaching their characteristic "equilibrium" spectra after which the attenuation coefficient is nearly independent of position. This phenomenon can be understood qualitatively by considering the Boltzmann equation (2.3.1) for neutron transport

$$\left[\frac{\partial}{\partial x} + \sigma_n(E)\right] \phi_n(x,E) = \hat{G}(x,E) \sim L(E)g(x) \tag{5.5}$$

where $\hat{G}(x,E)$ represents the secondary particle production term. We have represented $\hat{G}$ as a separable product in space and energy variables. This approximation is justified for neutron production which is dominated by the high energy proton flux. For high energies $S_p(E)$ is small and the nuclear mean free path is on the order of meters (in water) making $\hat{G}(x,E)$ a slow function of distance. For high energy proton collisions the energy spectra of neutron production in $\hat{G}(x,E)$ is relatively independent of penetration distance except for locations

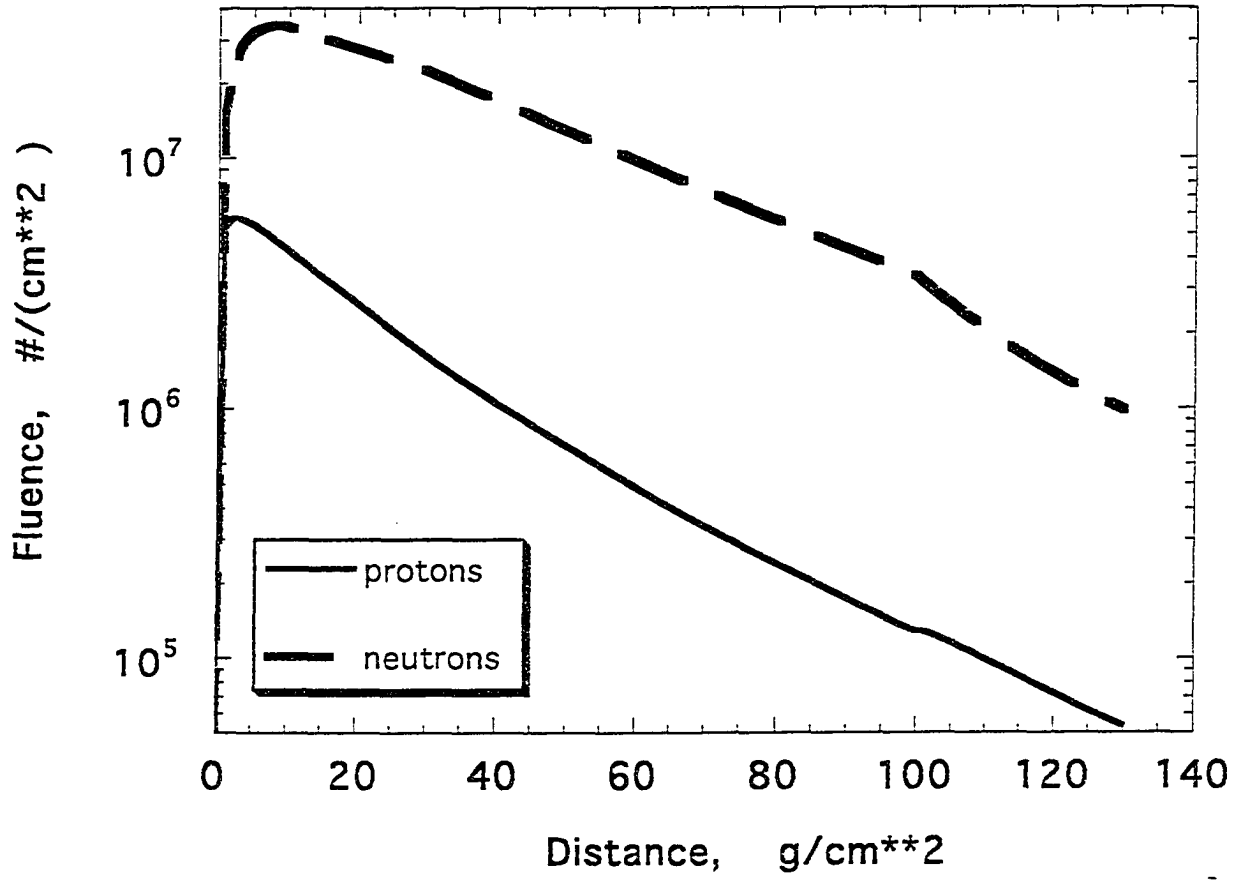

Fig. 28 Integral Fluence. 100 g/cm**2 of Aluminum Shield followed by 30 g/cm**2 Tissue

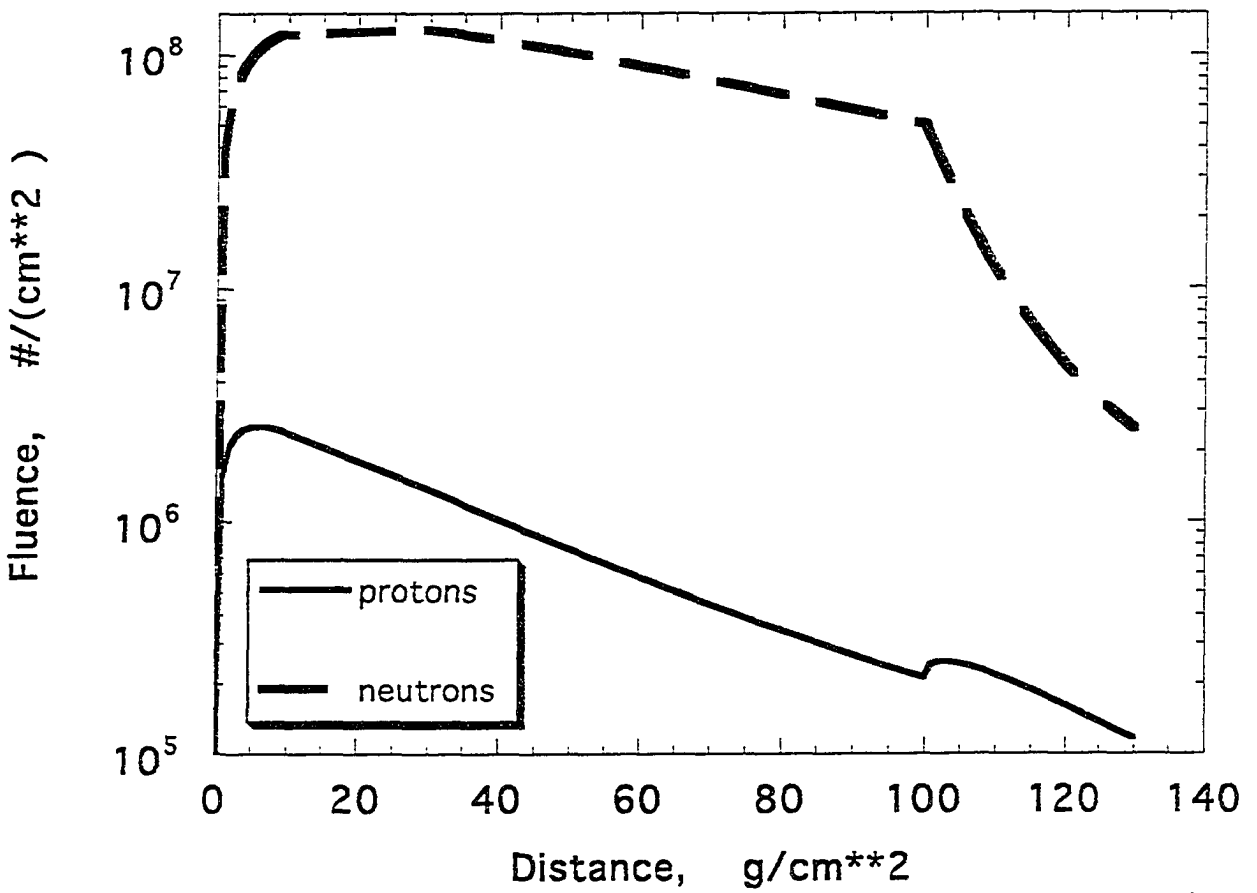

Fig. 29 Integral Fluence. 100 g/cm**2 of Lead Shield followed by 30 g/cm**2 tissue

near the incident boundary where ϕ_n grows rapidly from a zero value. Equation (5.5) has the solution

$$\phi_n(x,E) = L(E) \int_0^x e^{-\sigma(x-y)} g(y) dy \tag{5.6}$$

but since $\frac{\partial \hat{G}}{dx} \sim 0$ the solution over distances of several centimeters can be written

$$\phi_n(x,E) \sim L(E)\overline{g}\left[1 - e^{-\sigma x}\right] \tag{5.7}$$

where $\sigma x \ll 1$, for $\sigma^{-1} \ll \frac{\partial \hat{G}}{\partial x}$. On reaching the tissue slab at $x = 100$ g/cm^2, each fluence type deviates from the equilibrium shape characteristic of the shield (figs. 28 and 29). A positive "bump" is seen for protons in the transition region ($x \sim$ 100–110 g/cm^2) and a corresponding decrease is observed for neutrons. The hydrogenic tissue increases the crossection for neutrons to produce protons. After the transition region is passed, each particle fluence approaches a new "equilibrium" region and the attenuation coefficient assumes a value characteristic of the tissue. The proton bump explains the dose shoulder seen in figures 15–16. The effect of the transition region on particle fluence can be further highlighted by looking at the collision density C_j where

$$C_j(x) = \int_{\text{absorption}} \sigma_j(E)\ \phi_j(E) dE \tag{5.8}$$

Figure 30 shows $C_j(x)$ for the primary and the total secondary spectrum in 100 g/cm^2 of aluminum followed by 30 g of tissue. The secondaries build up rapidly while the primaries decay monotonically. C_j experiences an almost discontinuous decrease at the shield-tissue interface. We note that the difference between C_j and I_j is the inclusion of the slowing down term (eg. $\psi_j(x,E) = S_p(E)\phi_j(x,E)$).

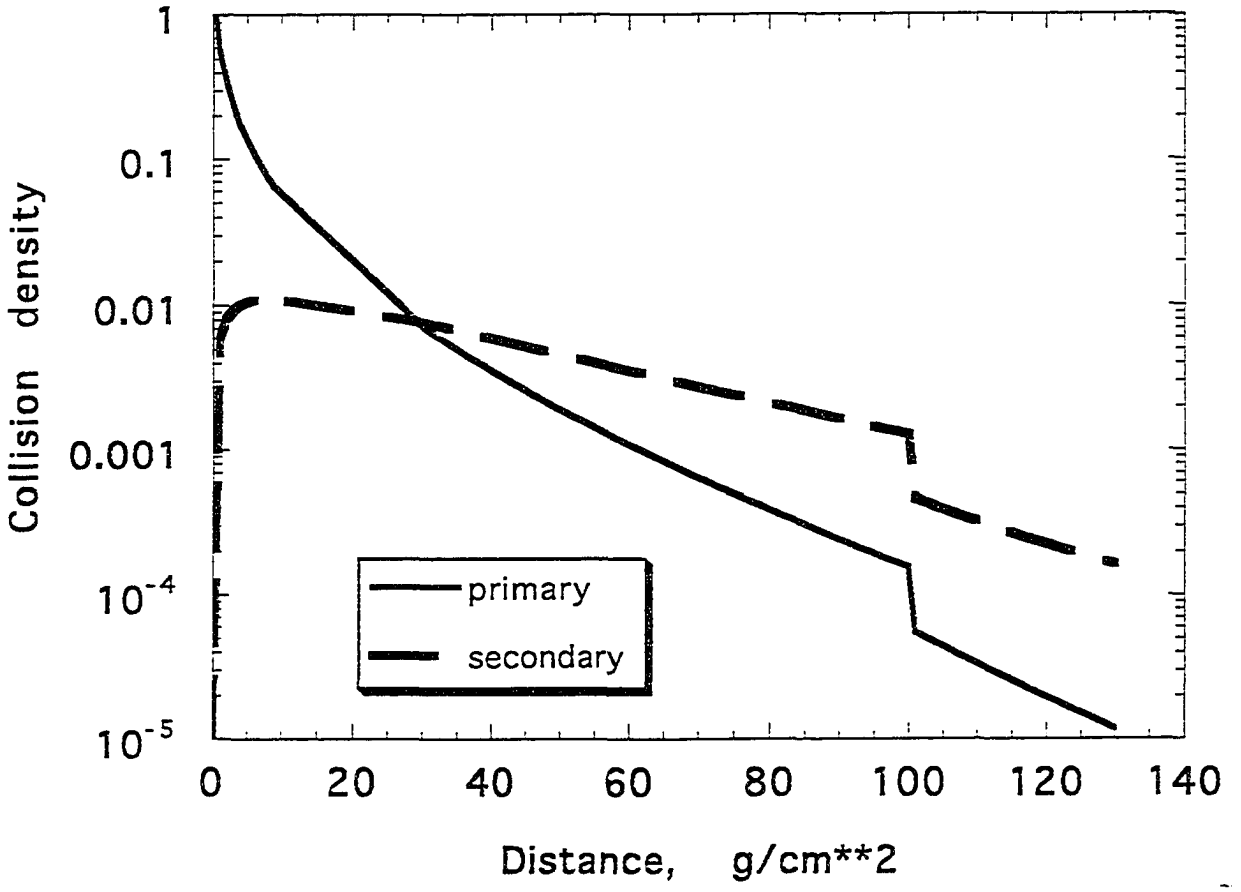

Fig. 30 Collision Density . 100 g/cm**2 Aluminum Shield followed by 30 g/cm**2 tissue

6. Summary and Future Work

In this dissertation we developed a theory for energetic nucleon transport. Our approach used the 1-D Boltzmann equation in the context of the straight-ahead approximation. We developed a numerical implementation of the solution and demonstrated that the approach is adequate for practical space shielding calculations while requiring substantially less computing power than comparable Monte Carlo codes.

In Chapter 2 we showed that the Boltzmann equation for high energy nucleon transport (eq. 2.1.19) can be developed from the kinetic theory of gases using conservation principles. The Boltzmann equation was mapped onto a set of characteristic coordinates which facilitated development of a solution based on an integrating factor. Separate solutions were obtained for proton (eq. 2.4.1) and neutron transport (eq. 2.4.2). These solutions are "coupled" in the sense that calculation of fluence for type j nucleon at position x requires knowledge of both types of nucleon fluences at position $x - z$.

We reviewed the perturbation theory approach to solution of coupled nucleon transport. We showed that the physical process of "secondary" generation nucleon production fits nicely into the mathematical development of a converging Neumann series (eq. 2.5.5). A computer program, implementing a recursive method for solution of the fluence, showed that the protons converge after a few generations of secondaries. The neutrons, however, do not converge as well since they are not attenuated by electronic slowing processes. This limitation in the application of the perturbation approach combined with the relative inefficiency of the numerical implementation led us to examine alternative approaches to computation of the nucleon fluence.

In Chapter 3 we developed a set of exact solutions for the transported nucleon fluence using analytical functions to represent the incident boundary fluence and the secondary fluence production term. This particular set of functional representations is relevant to the case of space radiation transport. We call these solutions "benchmarks" because they can be used to assess the accuracy of approximate numerical schemes.

In Chapter 4 we developed an approximate numerical scheme to evaluate the integral equation for the nucleon fluence (eq. 4.1.1). Our approach used a marching scheme to propagate the solution from the boundary to any desired penetration depth inside a slab of shield material. We proposed a scheme to decouple the double integral in the secondary production term (to reduce operation count) while maintaining second order accuracy (eq. 4.1.6). We solved the approximate form (eq. 4.1.6) using the analytical expressions for boundary fluence and production spectra from Chapter 3. We then compared these solutions with the exact benchmarks to determine the error term. We applied two minimization approaches to determine values for Q_1^{ij} and Q_2^{ij} to retain second order accuracy.

The second order accurate numerical scheme was applied to the case of space radiation transport in Chapter 5. The transport algorithm was incorporated into the BRYNTRN computer program and the effect of second and third order accurate choices of Q_1^{ij} and Q_2^{ij} was assessed. We studied the case of deep penetration into an aluminum shield followed by a tissue slab. The BRYNTRN solutions were compared with a set of HETC of Monte Carlo benchmarks and the results indicated good agreement. We found a significant change in proton dose in the interface region (i.e., <6 gm/cm^2 inside the tissue slab). This 'shoulder' effect was explained by the departure from the equilibrium neutron fluence spectra as it entered the hydrogenic tissue.

In Appendix A we developed a set of benchmarks for the case of a monoenergetic incident fluence spectra. This case is relevant to accelerator applications. We showed results comparing analytical benchmarks with BRYNTRN using selected Q values to minimize error. We found that the same Q values obtained for the continuous benchmark cases also preserve second order accuracy for the monoenergetic case.

In Appendix B we studied the problem of neutron elastic scattering. We showed that the energy grids used by BRYNTRN for nuclear fragmentation are too coarse for the small energy transfers associated with elastic scattering. We analyzed the neutron Boltzmann equation and found that the neutron fluence at position $x_0 + h$ can be described by an

energy shifted fluence at x_0. We used this relationship in the BRYNTRN program to model elastic scattering. We found that the model recovers > 95% of the elastically rescattered fluence independently of energy grid resolution. The elastic rescattering model was applied to several shield types representing light and heavy elements.

In Appendix C we developed an expression for the heavy target fragment fluence. These ions do not transport far from the collision site but deposit their energy locally. Therefore, this fluence term (eq. C.6) is important for estimating total deposited dose.

Future Considerations

Two primary areas of future work related to the transport process are the extension to three dimensions and the inclusion of pion transport. Both of these enhancements are important for deep penetration transport. The 1-D Boltzmann approach is limited to the region of applicability of the straight-ahead approximation. An upper limit for spacecraft transport is about 150 g/cm^2 but aircraft shielding may require substantially deeper penetration.

A computationally realistic approach to 3-d nucleon transport is not yet clear. We mean this is the context of a useful design tool. The HETC[81] Monte Carlo codes, of course, currently incorporate multidimensional capability.

The incorporation of pion transport into the nucleon code will improve accuracy for high energy proton interactions. The pion channel turns on at about 400 MeV for proton-proton scattering. The addition of the pions to the transport formalism is straightforward, but awaits the development of a robust reaction database for incorporation into the BRYNTRN code.

The elastic scattering model for neutrons does not account for back scatter. The neutron albedo near the boundaries is not modeled. The next step in future work with elastic scattering model should be the development of a two-stream approach to handle back scatter.

References

1. Lamkin, S. L.: A Theory for High-Energy Nucleon Transport in One Dimension, M. S. Thesis, Old Dominion University, December 1974.
2. Gaisser, T. K.: Cosmic Rays and Particle Physics. Cambridge University Press, Cambridge, 1990.
3. Allkofer, O. C.: Introduction to Cosmic Radiation. Verlag Karl Thiemig, Munich, 1975.
4. Stassinopoulos, E. G., and Raymond, J. P.: The Space Radiation Environment for Electronics. Proc. of IEEE, 76, No. 11, 1988.
5. Alsmiller, R. G., Jr.; Santoro, R. T.; Barish, J.; and Claiborne, H. C.: Shielding of Manned Space Vehicles Against Protons and Alpha Particles, ORNL-RSIC-35, 1972.
6. Wilson, J. W.; Townsend, L .W.; Schimmerling, W.; Khandelwal, G. S.; Khan, F.; Nealy, J. E.; Cucinotta, F. A.; Simonsen, Shinn, J. L.; and Norbury, J. W.: Transport Methods and Interactions for Space Radiation. NASA RP-1257, 1991.
7. Wilson, J. W., Cucinotta, F. A., and Shinn, J. L.: Cell Kinetics and Track Structure. Biological Effects and Physics of Solar and Galactic Cosmic Radiation, Part A. Edited by Swenberg, C. E. et al., Plenum Press, New York, 1993.
8. Wilson, John W.; and Townsend, Lawerence W.: Radiation Safety in Commercial Air Traffic: A Need for Further Study. *Health Phys.*, vol. 55, no. 6, Dec. 1988, pp. 1001–1003.
9. Kase, K. R. and Nelson, W. R.: Concepts of Radiation Dosimetry. Pergamon Press, New York, 1978.
10. Adams, J. H., Jr.; Silberberg, R.; and Tsao, C. H.: *Cosmic Ray Effects on Microelectronics. Part I: The Near-Earth Particle Environment.* NRL-MR-4506-PT-1, Naval Research Lab., Aug. 1981. (Available from DTIC as AD A103 897.)
11. Wilson, John W.; and Lamkin, Stanley L.: Perturbation Theory for Charged-Particle Transport in One Dimension. *Nucl. Sci. & Eng.*, vol. 57, no. 4, Aug. 1975, pp. 292–299.

12. Foelsche, Trutz; Mendell, Rosalind B.; Wilson, John W.; and Adams, Richard R.: *Measured and Calculated Neutron Spectra and Dose Equivalent Rates at High Altitudes: Relevance to SST Operations and Space Research.* NASA TN D-7715, 1974.

13. Wilson, John W.; Townsend, Lawrence W.; Nearly, John E.; Chun, Sang Y.; Hong, B. S.; Buck, Warren W.; Lamkin, S. L.; Ganapol, Barry D.; Khan, Ferdous; and Cucinotta, Francis A.: *BRYNTRN: A Baryon Transport Model.* NASA TP-2887, 1989.

14. Wilson, J. W.; Chun, S. Y., Badavi, F. F., Townsend, L. W.; and Lamkin, S. L.: HZETRN: A Heavy Ion/Nucleon Transport Code for Space Radiations. NASA TP-3146, 1991.

15. Lamkin, S. L.; Khandelwal, G. S.; Shinn, J. L.; and Wilson, J. W.: Space Proton Transport in One Dimension. *Nucl. Sci. and Eng.*, vol. 116, no. 4, Apr. 1994, p291.

16. Townsend, Lawrence W.; Nealy, John E.; Wilson, John W.; and Atwell, William: Large Solar Flare Radiation Shielding Requirements for Manned Interplantary Mission. *J. Spacecr. & Rockets*, vol. 26, no. 2, Mar./Apr. 1989, pp. 126–128.

17. Wilson, John W.: *Analysis of the Theory of High-Energy Ion Transport.* NASA TN D-8381, 1977.

18. Alsmiller, R. G., Jr.: High-Energy Nucleon Transport and Space Vehicle Shielding. *Nucl. Sci. & Eng.*, vol. 27, no. 2, Feb. 1967, pp. 158–189.

19. Peters, B., 1958: The Nature of Primary Cosmic Radiation. *Progress in Cosmic Ray Physics*, J. G. Wilson, ed., Interscience Publ., Inc., pp. 191–242.

20. Dye, D. L.; and Noyes, J. C., 1960: Biological Shielding for Radiation Belt Particles. *J. Astronaut. Sci.*, vol. VII, no. 3, pp. 64–70.

21. Bradt, H. L., and Peters, B.: *Phys. Rev.*, 74, 1828, 1948.

22. Stehn, John R.; Goldberg, Murrey D.; Magurno, Benjamin A.; and Wiener-Chasman, Renate: Neutron Cross Sections. *Volume 1, Z = 1 to 20. BNL 325. Second ed.*, Suppl. No. 2, (Physics—TID-4500, 32nd ed.), Sigma Center, Brookhaven National Lab. Associated Univ., Inc., May 1964.

23. Bobchenko, B. M.; Buklei, A. E.; Viasov, A. V.; Vorob'ev, I.I.; Vorob'ev, L. S.; Goryainov, N. A.; Grishuk, Yu. G.; Gushchin, O. B.; Druzhinin, B. L.; Zhurkin, V. V.; Zavrazhnov, G. N.; Kosov, M. V.; Leksin, G. A.; Stolin, V. L.; Surin, V. P.; Fedorov, V. B.; Fominykh, B. A.; Shvartsman, B. B.; Shevchenko, S. V.; and Shuvalov, S. M.: Measurement of Total Inelastic Cross Sections for Interaction of Protons With Nuclei in the Momentum Range From 5 to 9 GeV/c and for Interaction of π^- Mesons With Nuclei in the Momentum Range From 1.75 to 6.5 GeV/c. *Soviet J. Nucl. Phys.*, vol. 30, no. 6, Dec. 1979, pp. 805–813.

24. Hughes, Donald J.; and Schwartz, Robert B.: Neutron Cross Sections, *BNL 325, Second ed.*, Brookhaven National Lab., July 1, 1958.

25. Guzik, T. G.; Wefel, J. P.; Crawford, H. J.; Greiner, D. E.; Lindstrom, P. J.; Schimmerling, W.; and Symons, T. J. M.: Implications of New Measurements of $^{16}O + p \rightarrow {}^{12,13}C, {}^{14,15}N$ for the Abundances of C, N. Isotopes at the Cosmic Ray Source. *19th International Cosmic Ray Conference, OG Sessions*, Volume 2, NASA CP-2376, 1985, pp. 80–83. (Available as OG 4.3-2).

26. Lock, W. O.; and Measday, D. F.: *Intermediate Energy Nuclear Physics.* Methuen & Co. Ltd. (London), 1970.

27. Goldberger, M. L., 1948: The Interaction of High Energy Neutrons and Heavy Nuclei. *Phys. Review*, vol. 74, no. 10, pp. 1269–1277.

28. Gross, Franz: New Theory of Nuclear Forces—Relativistic Origin of the Repulsive Core. *Phys. Review D*, vol. 10, no. 1, July 1, 1974, pp. 223–242.

29. Fernbach, S.: Nuclear Radii as Determined by Scattering of Neutrons. *Reviews Modern Phys.*, vol. 30, no. 2, pt. 1, Apr. 1958, pp. 414–418.

30. Siemens, P. J.; and Jensen, A. S.: Elements of Nuclei, Many-Body Physics with the Strong Interaction. Addison-Wesley Publishing Co., Inc., 1987.

31. Ginzburg, V. L.; and Syrovatskii, S. I. (H. S. H. Massey, transl., and D. Ter Haar, ed.), 1964: *The Origin of Cosmic Rays.* Macmillan Co.

32. Curtis, S. B.; Doherty, W. R.; and Wilkinson, M. C., 1969: *Study of Radiation Hazards to Man on Extended Near Earth Missions.* NASA CR-1469.

33. Wilson, John W.: Environmental Geophysics and SPS Shielding. *Workshop on the Radiation Environment of the Satellite Power System*, Walter Schimmerling and Stanley B. Curtis, eds., LBL-8581 (Contract W-7405-ENG-48), Univ. of California, Sept. 15, 1978, pp. 33–116.

34. Khan, F.: Nuclear Fragmentation Energy and Momentum Transfer Distributions in Relativistic Heavy-Ion Collisions. Ph.D. Diss., Old Dominion University, 1989.

35. Wilson, John W.; and Badavi, F. F.: Methods of Galactic Heavy Ion Transport. *Radiat. Res.*, vol. 108, 1986, pp. 231-237.

36. Wilson, J. W.; Townsend, L. W.; and Badavi, F. F.: Galactic HZE Propagation Through the Earth's Atmosphere. *Radiat. Res.*, vol. 109, no. 2, Feb. 1987, pp. 173–183.

37. Wilson, J. W.; Townsend, L. W.; Lamkin, S. L.; and Ganapol, B. D.: A closed-Form Solution to the HZE Propagation. *Radia. Res.*, 122, p. 223, 1990.

38. Allkofer, O. C.; and Heinrich, W., 1974: Attenuation of Cosmic Ray Heavy Nuclei Fluxes in the Upper Atmosphere by Fragmentation. *Nuclear Phys. B*, vol. B71, no. 3, pp. 429–438.

39. Nealy, John E.; Wilson, John W.; and Townsend, Lawrence W.: *Solar-Flare Shielding With Regolith at a Lunar Base Site.* NASA TP-2869, 1989.

40. Nealy, John E.; Wilson, John W.; and Townsend, Lawrence W.: *Preliminary Analyses of Space Radiation Protection for Lunar Base Surface Systems.* SAE Tech. Paper Ser. 891487, July 1989.

41. Nealy, John E.; Simonsen, Lisa C.; Sauer, Herbert H.; Wilson, John W.; and Townsend, Lawrence W.: *Space Radiation Dose Analysis for Solar Flare of August 1989.* NASA TM-4229, 1990.

42. Ganapol, Barry D.; Townsend, Lawrence W.; Lamkin, Stanley L.; and Wilson, John W., 1991: *Benchmark Solutions for the Galactic Heavy-Ion Transport Equations With Energy and Spatial Coupling.* NASA TP-3112.

43. Wilson, John W.; and Townsend, L. W., 1988: A Benchmark for Galactic Cosmic-Ray Transport Codes. *Radiat. Res.*, vol. 114, no. 2, pp. 201–206.

44. Wilson, John W.; Lamkin, Stanley L.; Farhat, Hamidullah; Ganapol, Barry D.; and Townsend Lawrence W., 1989a: *A Hierarchy of Transport Approximations for High Energy Heavy (HZE) Ions.* NASA TM-4118.

45. Townsend, L. W., and Wilson, J. W.: Interaction of Space Radiation with Matter. Proceedings of 41st Congress of International Astronautical Federation, 1990. IAF/IAA-90-543.

46. Simpson, J. A.: Elemental and Isotopic Composition of the Galactic Cosmic Rays. Annual Reviews of Nuclear and Particle Science, 32, 323, 1983.

47. Wilson, J. W., and Khandelwal, G. S.: Proton Dose Approximation in Arbitrary Convex Geometry. *Nucl. Tech.*, 23, p. 298, 1974.

48. Wilson, J. W., Nealy, J. E., Qualls, G., Atwell, W., Shinn, J. L., and Simonsen, L. C.: Exposure Fluctuations of Astronauts due to Orientation. NASA TP-3364, 1993.

49. Dye, David L., 1962: Space Proton Doses at Points Within the Human Body. *Proceedings of the Symposium on the Protection Against Radiation Hazards in Space*, Book 2, TID-7652, United States Atomic Energy Commission, pp. 633–661.

50. Walske, M. C.; and Bethe, H. A.: Asymptotic Formula for Stopping Power of K-Electrons. *Phys. Review*, vol. 83, 1951, pp. 457–458.

51. Khandelwal, G. S.: Shell Corrections for K and L Electrons. *Nuclear Phys.*, vol. A116, no. 1, 1968, pp. 97–111.

52. Khandelwal, G. S.: Stopping Power of K and L Electrons. *Phys. Rev. A*, vol. 26, Third Series, no. 5, 1982, pp. 2983–2986.

53. Xu, Y. J., Khandelwal, G. S., and Wilson, J. W.: Proton Stopping Cross Sections of Liquid Water. *Phys. Rev. A*, vol. 32, Third Series, no. 1, 1985, pp. 629–632.

54. Khandelwal, G. S. and Merzbacher, E.: Stopping Power of M Electrons. *Phys. Rev.*, vol. 144, 1966, p. 349.

55. Wilson, J. W.; and Kamaratos, E.: Mean Excitation Energy for Molecules of Hydrogen and Carbon. *Phys. Lett.*, vol. 85A, no. 1, Sept. 7, 1981, pp. 27–29.

56. Andersen, H. H.; and Ziegler, J. F.: *Hydrogen Stopping Powers and Ranges in All Elements.* Pergamon Press, Inc., c.1977.

57. Janni, Joseph F.: *Calculations of Energy Loss, Range, Pathlength, Straggling, Multiple Scattering, and the Probability of Inelastic Nuclear Collisions for 0.1- to 1000-Mev Protons.* AFWL-TR-65-150, U.S. Air Force, Sept. 1966. (Available from DTIC as AD 643 837).

58. Bichsel, Hans: Passage of Charged Particles Through Matter. *American Institute of Physics Handbook, Second ed.*, Dwight E. Gray, ed., McGraw-Hill Book Co., Inc., 1963, pp. 8-20–8-47.

59. Ziegler, J. F.: *Helium Stopping Powers and Ranges in All Elemental Matter.* Pergamon Press, c.1977.

60. Wilson, J. W.; Chang, C. K.; Xu, Y. J.; and Kamaratos, E.: Ionic Bond Effects on the Mean Excitation Energy for Stopping Power. *J. Appl. Phys.*, vol. 53, no. 2, Feb. 1982, pp. 828–830.

61. Matteson, S.; Powers, D.; and Chau, E. K. L.: Physical-State Effect in the Stopping Cross Section of H_2O Ice and Vapor for 0.3 to 2.0 MeV α Particles. *Phys. Review*, ser. A, vol. 15, no. 3, Mar. 1977, pp. 856–864.

62. Wilson, J. W.; and Xu, Y. J.: Metallic Bond Effects on Mean Excitation Energies for Stopping Power. *Phys. Lett.*, vol. 90A, no. 5, July 12, 1982, pp. 253–255.

63. Northcliffe, L. C.; and Schilling, R. F.: Range and Stopping-Power Tables for Heavy Ions. *Nucl. Data*, Sect. A, vol. 7, no. 3–4, Jan. 1970, pp. 233–463.

64. Janni, Jospeh F., 1982a: Proton Range-Energy Tables, 1 keV–10 GeV —Energy Loss, Range, Path Length, Time-of-Flight, Straggling, Multiple Scattering, and Nuclear Interaction Probability. Part 1. For 63 Compounds. *At. Data & Nuclear Data Tables*, vol. 27, nos. 2/3, pp. 147–339.

65. Janni, Jospeh F., 1982b: Proton Range-Energy Tables, 1 keV–10 GeV —Energy Loss, Range, Path Length, Time-of-Flight, Straggling, Multiple Scattering, and Nuclear Interaction Probability. Part 2. For Elements $1 \leq Z \leq 92$. *At. Data & Nuclear Data Tables*, vol. 27, nos. 4/5, pp. 341–529.

66. Silberberg, R.; Tsao, C. H.; and Shapiro, M. M.; Semiempirical Cross Sections, and Applications to Nuclear Interactions of Cosmic Rays. *Spallation Nuclear Reactions and Their Applications*, B. S. P. Shen and M. Merker, eds., D. Reidel Publ. Co., c.1976, pp. 49–81.

67. Heckman, H. H.: *Heavy Ion Fragmentation Experiments at the Bevatron.* NASA CR-142589, 1975.

68. Feshbach, H.; and Huang, K.: Fragmentation of Relativistic Heavy Ions. *Phys. Lett.*, vol. 47B, no. 4, Nov. 26, 1973, pp. 300–302.

69. Townsend, Lawrence W.; and Wilson, John W.: *Tables of Nuclear Cross Sections for Galactic Cosmic Rays—Absorption Cross Sections.* NASA RP-1134, 1985.

70. Serber, R.: Nuclear Reactions at High Energies. *Phys. Review*, vol. 72, no. 11, Dec. 1, 1947, pp. 1114–1115.

71. Wilson, J. W.: Composite Particle Reaction Theory. Ph.D. Diss., College of William and Mary, 1975.

72. Goldhaber, A. S.: Statistical Models of Fragmentation Processes. *Phys. Lett.*, vo. 53B, no. 4, Dec. 23, 1974, pp. 306–308.

73. Cocconi, G.; Cocconi-Tongiorgi, V.; and Widgoff, M., 1950: Cascades of Nuclear Disintegrations Induced by the Cosmic Radiation. *Phys. Review*, vol. 79, second ser., no. 5, pp. 768–780.

74. Chatterjee, A.; Tobias, C. A.; and Lyman, J. T., 1976: Nuclear Fragmentation in Therapeutic and Diagnostic Studies With Heavy Ions. *Spallation Nuclear Reactions and Their Applications*, B. S. P. Shen and M. Merker, eds., D. Reidel Publ. Co., pp. 169–191.

75. Alsmiller, R. G., Jr.; Armstrong, T. W.; and Coleman, W. A.: The Absorbed Dose and Dose Equivalent From Neutrons in the Energy Range 60 to 3000 MeV and Protons in the Energy Range 400 to 3000 MeV. *Nucl. Sci. & Eng.*, vol. 42, no. 3, Dec. 1970, pp. 367–381.

76. *MECC-7 Intranuclear Cascade Code. 500-MeV Protons on 0-16. I4C Analysis Codes* (Programmed for H. W. Bertini). Available from Radiation Shielding Information Center, Oak Ridge National Lab., 1968.

77. Bertini, Hugo W.; Guthrie, Miriam P.; and Culkowski, Arline H.: *Nonelastic Interactions of Nucleons and π-Mesons With Complex Nuclei at Energies Below 3 GeV.* ONRL-TM-3148, U.S. Atomic Energy Commission, Mar. 28, 1972.

78. Platzman, Robert L.: On the Primary Processes in Radiation Chemistry and Biology. *Symposium on Radiobiology—The Basic Aspects of Radiation Effects on Living Systems*, James J. Nickson, ed., John Wiley & Sons, Inc., c.1952, pp. 97–116.

79. Kinney, W. E.: The Nucleon Transport Code, NTC. QRNL-3610, 1964.

80. Coleman, W. A.; and Armstrong, T. W.: The Nucleon-Meson Transport Code, NMTC. ORNL-460b, 1970.

81. Chandler, K. C.; and Armstrong, T. W.: Operating Instructions for the High-Energy Nucleon-Meson Transport Code HETC, ORNL-4744, 1972.

82. Lambiotte, J. J.; Wilson, J. W.; and Filippas, T. A.: PROPER-3C, A Nucleon Pion Transport Code. NASA TM X-2158, 1971.

83. Metropolis, N.; Bivins, R.; Storm, M.; Turkevich, Anthony; Miller, J. M.; and Friedlander, G., 1958: Monte Carlo Calculations on Intranuclear Cascades. I. Low-Energy Studies. *Phys. Review*, vol. 110, second ser., no. 1, pp. 185–203.

84. Schaefer, Hermann J., 1959: *Radiation and Man in Space.* Volume 1 of *Advances in Space Science*, Frederick I. Ordway III, ed., Academic Press, Inc., pp. 267–339.

84a. Foelsche, T.: Estimate of the Specific Ionization Caused by Heavy Cosmic Ray Primaries in Tissue or Water. *J. Astronaut. Sci.*, vol. VI, no. 4, pp. 57–62, 1959.

85. Bertini, H. W., 1962: Monte Carlo Calculations for Intranuclear Cascades. *Proceedings of the Symposium on the Protection Against Radiation Hazards in Space*, Book 2, TID-7652, United States Atomic Energy Commission, pp. 433–522.

86. Gloeckler, G.; and Jokipii, J. R., 1969: Physical Basis of the Transport and Composition of Cosmic Rays in the Galaxy. *Phys. Review Lett.*, vol. 22, no. 26, pp. 1448–1453.

87. Lezniak, J. A., 1979: The Extension of the Concept of the Cosmic-Ray Path-Length Distribution to Nonrelativistic Energies. *Astrophys. & Space Sci.*, vol 63, no. 2, pp. 279–293.

88. Wilson, John W.; Townsend, Lawrence W.; Chun, Sang Y.; Buck, Warren W.; Khan, Ferdous; and Cucinotta, Frank: *BRYNTRN: A Baryon Transport Computer Code—Computation Procedures and Data Base.* NASA TM-4037, 1988.

89. Reif, F.: Fundamentals of Statistical and Thermal Physics. McGraw-Hill, Inc., New York, 1965.

90. Chen, F. F.: Introduction to Plasma Physics and Controled Fusion, 2nd edition. Plenum Press, New York, 1984.

91. Tritton, D. J.: Physical Fluid Dynamics. Van Nostrand Reinhold Company, London, 1977.

92. Williams, M. M. R.: The Slowing Down and Thermalization of Neutrons. North-Holland Publishing Company, Amsterdam, 1966.

93. Pomraning, G. C.: A Method of Solution for Particle Transport Problems. NASA CR-GA-6497, July 1965.

94. Alsmiller, R. G.; Irving, D. C.; and Moran, H. S.: The Validity of the Straightahead Approximation in Space Vehicle Shielding Studies. *Nucl. Sci. and Eng.*, 32, p. 56, 1968.

95. Alsmiller, R. G., Jr.; Irving, D. C.; Kinney, W. E.; and Moran, H. S., 1965: The Validity of the Straightahead Approximation in Space Vehicle Shielding Studies. *Second Symposium on Protection Against Radiatons in Space*, Arthur Reetz, Jr., ed., NASA SP-71, pp.177–181.

96. Purcell, E. J.: Calculus with Analytic Geometry. Meredith Publishing Co., New York, 1965.

97. Arfken, G.: Mathematical Methods for Physicists, 2 ed., Academic Press, New York, 1970.

98. Courant, R.; and Hilbert, D.: Methods of Mathematical Physics. Interscience Publishers, New York, 1953.

99. Matthews, J.; and Walker, R. L.: Mathematical Methods of Physics. W. A. Benjamin, Inc., New York, 1965.

100. Wright, H. A.; Anderson, V. E., Turner, J. E.; Neufeld, J.; and Synder, W. S.: *Health Physics*, 16, p. 13, 1969.

101. Turner, J. E.; Wright, H. A.; and Grossen, J. H.: *Health Phys.*, 18, p. 82, 1970.

102. Wilson, John W.; Townsend, Lawrence W.; Ganapol, Barry; Chun, Sang Y.; and Buck, Warren W.: Charged-Particle Transport in One Dimension. *Nucl. Sci. & Eng.*, vol 99, no. 3, July 1988, pp. 285–287.

103. Hildebrand, F. B.: Introduction to Numercial Analysis, 2nd edition. Dover Publications, New York, 1974.

104. Shinn, J. L.; Wilson, J. W.; Weyland, M.; and Cucinotta, F. A.: Improvements in Computational Accuracy of BRYNTRN (A Baryon Transport Code). NASA TP-3093, 1991.

105. Dahlquist, G., and Bjorck, A.: Numerical Methods. Prentice-Hall, Englewood Cliffs, 1974.

106. Press, W. H.; Tenkolsky, S. A., Vetterling, W. T.; and Flannery, B. P.: Numercial Recipes in FORTRAN, 2nd edition. Cambridge University Press, Cambridge, 1992.

107. Ranft, J.: The FLUKA and KASPRO Hadronic Cascade Codes. *Computer Techniques in Radiation Transport and Dosimetry*, Walter R. Nelson and Theodore M. Jenkins, eds., Plenum Press, c1980, pp. 339–371.

108. King, Joseph H.: Solar Proton Fluences for 1977–1983 Space Missions. *J. Spacecr. & Rockets*, vol. 11, no. 6, June 1974, pp. 401–408.

109. Wilson, J. W.; Townsend, L. W.; and Khan, F.: *Health Phys.*, 57, p. 717, 1989.

110. Shinn, J. L.; and Wilson, J. W.: *Health Phys.*, 61, p. 415, 1991.

111. Scott, W. Wayne; and Alsmiller, R. G., Jr.: *Comparisons of Results Obtained With Several Proton Penetration Codes.* ORNL-RSIC-17, U.S. At. Energy Commission, July 1967.

112. Wilson, John W.; Townsend, Lawrence W.; Ganapol, Barry D.; and Lamkin, Stanley L.: Methods for High Energy Hadronic Beam Transport. *Trans. American Nucl. Soc.*, vol. 56, June 1988, pp. 271-272.

Appendix A. Benchmark Transport Case for Monoenergetic Incident Spectra

In Chapter 3 we derived expressions for ψ_p and ψ_n in the case where functional forms can be used to simulate the incident fluence as a continuously distributed energy spectrum. That case is important for the cosmic ray environment. However, accelerator generated particles generally feature a narrow energy band. In this appendix we derive a benchmark case which can be used to study monoenergetic incident spectra, appropriate for accelerator radiations. The Boltzmann solution for coupled proton-neutron transport from equations 2.4.1 and 2.4.2, using constant crossections σ, is

$$\psi_n(x,r) = e^{-\sigma_n x}\psi_n(0,r) + \int_0^x dz\, e^{-\sigma_n z} \sum_j \int_r^\infty \overline{F}_{nj}(r,r')\psi_j(x-z,r')dr' \tag{A.1}$$

$$\psi_p(x,r) = e^{-\sigma_p x}\psi_p(0,r+x) + \int_0^x dz\, e^{-\sigma_p z} \sum_j \int_{r+z}^\infty \overline{F}_{pj}(r+z,r')\psi_j(x-z,r')dr' \tag{A.2}$$

Assume a form for the production spectra as:

$$\begin{aligned} \overline{F}_{pp}(r,r') &= \overline{F}_{nn} = C\, e^{-\alpha(r'-r)} \\ \overline{F}_{pn}(r,r') &= \overline{F}_{np} = C\, e^{-\alpha(r'-r)} \end{aligned} \tag{A.3}$$

Also assume a monoenergetic beam. Let r_0 represent the range for a proton with the specified incident energy of the monoenergetic projectiles. P_0 and N_0 are incident proton and neutron fluences.

$$P_0(x,r) = e^{-\sigma_p x}\, \hat{\delta}_p(r_0 - r - x)\delta_p \tag{A.4}$$

$$N_0(x,r) = e^{-\sigma_n x}\, \hat{\delta}_n(r_0 - r)\delta_n \tag{A.5}$$

where $\hat{\delta}$ is the Dirac delta and δ_j is the Kronecker delta. The perturbation expansion for the flux gives, using equation 2.5.5,

$$\psi_n(x,r) = N_0(x,r) + N_1(x,r) + N_2(x,r) + \ldots \tag{A.6}$$

$$\psi_p(x,r) = P_0(x,r) + P_1(x,r) + P_2(x,r) + \ldots \tag{A.7}$$

N_0 and P_0 are substituted for ψ in the integral production term to calculate N_1 and P_1. Let $\psi_P^0 \equiv P_0, \psi_n^0 \equiv N_0$. Removing subscripts from the σ's for notational convenience we write

$$\begin{aligned}
P_1(x,r) &= \int_0^x dz\, e^{-\sigma z} \left\{ \int_{r+z}^{\infty} \overline{F}_{pp}(r+z,r')\psi_p^0(x-z,r')dr' + \int_{r+z}^{\infty} \overline{F}_{pn}(r+z,r')\psi_n^0(x-z,r')dr' \right\} \\
&= \int_0^x dz\, e^{-\sigma z} \left\{ \int_{r+z}^{\infty} C\, e^{-\alpha(r'-(r+z))} e^{-\sigma(x-z)}\, \delta_p\hat{\delta}_p(r_0 - r' - (x-z))dr' \right. \\
&\quad \left. + \int_{r+z}^{\infty} C\, e^{-\alpha(r'-(r+z))}\, e^{-\sigma(x-z)} \delta_n\hat{\delta}_n(r_0 - r') \right\} \\
&= \int_0^x dz\, e^{-\sigma z} \int_{r+z}^{\infty} dr' C\, e^{-\alpha[r'-(r+z)]}\, e^{-\sigma(x-z)} \left\{ \delta_p\hat{\delta}_p(r_0 - r' - x + z) + \delta_n\hat{\delta}_n(r_0 - r') \right\}
\end{aligned}$$

$$P_1(x,r) = \int_0^x dz\, e^{-\sigma z}\, e^{-\sigma x + \sigma z} \int (\ldots)$$

$$P_1(x,r) = \int_0^x dz C e^{-\sigma x} \int_{r+z}^{\infty} dr' e^{-\alpha(r'-r-z)} \left\{ \delta_p\hat{\delta}_p(r_0 - r' - x + z) + \delta_n\hat{\delta}_n(r_0 - r') \right\} \tag{A.6}$$

Note limits on r':

let $r'' = r' - z \qquad dr'' = dr'$

lower $r' = r + z \rightarrow r'' = r$

$$P_1(x,r) = \int_0^x dz C e^{-\sigma x} \int_r^{\infty} dr''\, e^{-\alpha(r''-r)} \left\{ \delta_p\hat{\delta}_p(r_0 - r'' - x) + \delta_n\hat{\delta}_n(r_0 - r'' - z) \right\} \tag{A.7}$$

Integrating over the dirac deltas in equation (A.7)

$$= \int_0^x dz\ C\ e^{-\sigma x} \left\{ e^{-\alpha[(r_0-x)-r]}\delta_p + e^{-\alpha[(r_0-z)-r]}\delta_n \right\}$$

$$= \int_0^x dz\ C\ e^{-\sigma x} \left\{ e^{-\alpha(r_0-x-r)}\delta_p + e^{-\alpha(r_0-z-r)}\delta_n \right\}$$

$$= C\ x\ ^{-\sigma x}\ e^{-\alpha(r_0-x-r)}\delta_p + C\ e^{-\sigma x} \int_0^x dz\ e^{\alpha(r+z-r_0)}\delta_n \qquad \text{(A.8)}$$

let

$$z' = z - r_0 + r$$

$$dz' = dz$$

$$z = 0 \rightarrow z' = r - r_0$$

$$z = x \rightarrow z' = x - r_0 + r$$

$$\int_{r-r_0}^{x-r_0+r} dz'\ e^{\alpha z'} = \delta_n \frac{e^{\alpha z'}}{\alpha}\Big|_{r-r_0}^{x-r_0+r}$$

$$= \frac{\delta_n}{\alpha}\left[e^{\alpha(x-r_0+r)} - e^{\alpha(r-r_0)}\right]$$

$$= \frac{\delta_n}{\alpha}\left[e^{\alpha x}\ e^{\alpha(r-r_0)} - e^{\alpha(r-r_0)}\right]$$

$$= \frac{\delta_n}{\alpha}\ e^{\alpha(r-r_0)}\left[e^{\alpha x} - 1\right]$$

so equation (A.8) becomes

$$P_1(x,r) = C\ x\ e^{-\sigma x}\ e^{-\alpha(r_0-x-r)}\delta_p + C\ e^{-\sigma x}\frac{\delta_n}{\alpha}\ e^{\alpha(r-r_0)}[e^{\alpha x} - 1] \qquad \text{(A.9)}$$

$$P_1(x,r) = C\ e^{-\sigma x}\ e^{\alpha(r-r_0)}\left[x\Theta(r_0 - x - r)\delta_p\ e^{\sigma x} + \frac{\delta_n}{\alpha}\Theta(r_0 - r)(e^{\alpha x} - 1)\right]$$

or

$$P_1(x,r) = C\ e^{-\sigma x}\ e^{\alpha(r_0-r-x)}\left[x\delta_p\Theta(r_0-x-r)+\frac{\delta_n}{\alpha}\theta(r_0-r)\left(1-e^{-\alpha x}\right)\right] \qquad \text{(A.10)}$$

where Θ is the Heavyside step function. Now solve for N_1

$$\begin{aligned}
N_1(x,r) &= \int_0^x dz\ e^{-\sigma z}\int_r^\infty \sum_j \overline{F}_{nj}(r,r')\psi_j(x-z,r')dr' \\
&= \int_0^x dz\ e^{-\sigma z}\int_r^\infty dr'\left\{C\ e^{-\alpha(r'-r)}e^{-\sigma(x-z)}\delta_n\hat{\delta}_n(r_0-r')\right. \\
&\quad \left. + C\ e^{-\alpha(r'-r)}\ e^{-\sigma(x-z)}\delta_p\hat{\delta}_p(r_0-r'-x+z)\right\} \\
&= \int_0^x dz\ e^{-\sigma z}C\int_r^\infty dr' e^{-\alpha(r'-r)}\ e^{-\sigma(x-z)}\left[\delta_n\hat{\delta}_n(r_0-r')+\delta_p\hat{\delta}_p(r_0-r'-x+z)\right] \\
&= \int_0^x dz\ C\ e^{-\sigma x}\int_r^\infty dr'\ e^{-\alpha(r'-r)}\left[\delta_n\hat{\delta}_n(r_0-r')+\delta_p\hat{\delta}_p(r_0-r'-x+z)\right] \qquad \text{(A.11)}
\end{aligned}$$

Let

$$r'' = r' - r \qquad dr'' = dr'$$

$$r' = r \rightarrow r'' = 0$$

$$N_1 = \int_0^x dz\ C\ e^{-\sigma x}\int_0^\infty dr''\ e^{-\alpha r''}\left[\delta_n\hat{\delta}_n(r_0-r''-r)+\delta_p\hat{\delta}_p(r_0-r''-r-x+z)\right]$$

$$N_1 = \int_0^x dz\ C\ e^{-\sigma x}\left[e^{-\alpha(r_0-r)}\delta_n + e^{-\alpha(r_0-x+z')}\delta_p\right] \qquad \text{(A.12)}$$

$$\begin{aligned}
N_1(x,r) &= C\ e^{-\sigma x}\left[x\ e^{-\alpha(r_0-r)}\delta_n + \int_0^x dz e^{-\alpha(r_0-r-x)}e^{-\alpha z}\delta_p\right] \\
&= C\ e^{-\sigma x}\left[x\ e^{-\alpha(r_0-r)}\delta_n + \delta_p\ e^{-\alpha(r_0-r)}e^{\alpha x}\frac{e^{-\alpha z}}{-\alpha}\Big|_0^x\right] \\
&= C\ e^{-\sigma x}e^{-\alpha(r_0-r)}\left[x\delta_n - \delta_p\ e^{-\alpha x}\left(\frac{e^{-\alpha x}}{\alpha}-\frac{1}{\alpha}\right)\right]
\end{aligned}$$

$$N_1(x,r) = C\, e^{-\sigma x}\, e^{-\alpha(r_0-r)} \left[x\delta_n + \frac{\delta_p}{\alpha}\left(e^{\alpha x} - 1\right)\right]$$

$$N_1(x,r) = C\, e^{-\sigma x}\, e^{-\alpha(r_0-r-x)} \left[x\delta_n\, e^{-\alpha x} + \frac{\delta_p}{\alpha}\left(1 - e^{-\alpha x}\right)\right] \tag{A.13}$$

Now need second order terms $P_2(x,r)$ and $N_2(x,r)$.

$$P_2(x,r) = \int_0^x dz\, e^{-\sigma z} \left\{ \int_{r+z}^{\infty} \overline{F}_{pp}(r+z,r')P_1(x-z,r')dr' + \int_{r+z}^{\infty} \overline{F}_{pn}(r+z,r')N_1(x-z,r')dr' \right\} \tag{A.14}$$

Note that we assume $\overline{F}_{pn} = \overline{F}_{np} = \overline{F}_{nn} = \overline{F}_{pp}$ and write P_1 and N_1 from equations (A.9) and (A.13) to get

$$P_1(x,r) = \underbrace{\delta_p\, x\, C\, e^{-\sigma x} e^{-\alpha(r_0-r-x)}}_{I_1} + \underbrace{\frac{\delta_n\, C\, e^{-\sigma x}}{\alpha}\left[e^{-\alpha(r_0-r-x)} - e^{-\alpha(r_0-r)}\right]}_{I_2} \tag{A.15}$$

$$N_1(x,r) = \underbrace{\frac{\delta_p\, e^{-\sigma x} C}{\alpha}\left[e^{-\alpha(r_0-r-x)} - e^{-\alpha(r_0-r)}\right]}_{I_3} + \underbrace{\delta_n\, x\, e^{-\sigma x} C\, e^{-\alpha(r_0-r)}}_{I_4} \tag{A.16}$$

Solve term by term.

$$P_2^{I_1}(x,r) = \int_0^x dz\, e^{-\sigma z} \int_{r+z}^{\infty} C\, e^{-\alpha(r'-z-r)}\delta_p(x-z)\, C\, e^{-\sigma(x-z)}\, e^{-\alpha(r_0-r'-x-z)}dr'$$

but upper limit is not really ∞ but $r_0 - x$ for secondaries, limited by primaries range.

$$P_2^{I_1} = \int_0^x dz\, C^2(x-z)\delta_p\, e^{-\sigma x} \int_{r+z}^{r_0-x} e^{-\alpha(r_0-r-x)}dr'$$

Let

$$r'' = r' - z \rightarrow dr'' = dr'$$

$$r' = r + z \rightarrow r'' = r$$

$$r' = r_0 - x \rightarrow r'' = r_0 - x - z$$

so upper bound or r'' is still $r_0 - x$

$$P_2^{I_1} = \int_0^x dz\ C^2(x-z)\delta_p\ e^{-\sigma x} \int_r^{r_0-x} e^{-\alpha(r_0-r-x)} dr''$$

$$= \int_0^x dz\ C^2(x-z)\delta_p\ e^{-\sigma x}\ e^{-\alpha(r_0-r-x)}(r_0-r-x)$$

$$= C^2(r_0-r-x)\delta_p\ e^{-\sigma x} e^{-\alpha(r_0-r-x)} \int_0^x (x-z)dz$$

Let

$$z' = x - z \rightarrow dz' = -dz$$

$$z = 0 \rightarrow z' = x$$

$$z = x \rightarrow z' = 0$$

$$P_2^{I_1} = C^2\delta_p \frac{x^2}{2}\ e^{\sigma x}(r_0-r-x)\ e^{-\alpha(r_0-r-x)} \tag{A.17}$$

$$P_2^{I_2} = \int_0^x dz\ e^{-\sigma z} \int_{r+z}^{\infty} dr'\ C\ e^{-\alpha(r'-z-r)} \frac{\delta_n C}{\alpha}\ e^{-\sigma(x-z)} \left[e^{-\alpha(r_0-r'-x+z)} - e^{-\alpha(r_0-r')}\right]$$

$$= \frac{\delta_n C^2}{\alpha}\ e^{-\sigma x} \int_0^x dz \int_r^{r_0-x} dr'\ e^{-\alpha(-z-r)} \left[e^{-\alpha(r_0-x+z)} - e^{-\alpha r_0}\right]$$

$$= \frac{\delta_n C^2}{\alpha}\ e^{-\sigma x} \int_0^x dz \int_r^{r_0-x} dr' \left[e^{-\alpha(-z-r+r_0-x+z)} - e^{-\alpha(-z-r+r_0)}\right]$$

$$= \frac{\delta_n C^2}{\alpha}\ e^{-\sigma x} \int_0^x dz(r_0-x-r) \left[e^{-\alpha(r_0-r-x)} - e^{-\alpha(r_0-r-z)}\right]$$

$$P_2^{I_2} = \frac{\delta_n C^2}{\alpha}\ e^{-\sigma x}(r_0-x-r) \left[xe^{-\alpha(r_0-r-x)} - \int_0^x dz\ e^{-\alpha(r_0-r-z)}\right]$$

let

$$z' = r_0 - r - z$$

$$dz' = dz$$

$$z = 0 \rightarrow z' = r_0 - r$$

$$z = x \rightarrow z' = r_0 - r - x$$

$$-\left[-\int_{r_0-r}^{r_0-r-x} dz'\, e^{-\alpha z'}\right]$$

$$= -\left[-\frac{\left[e^{-\alpha z'}\right]}{-\alpha}\right]$$

$$= -\left[\frac{1}{\alpha}\left[e^{-\alpha(r_0-r-x)} - e^{-\alpha(r_0-r)}\right]\right]$$

$$P_2^{I_2} = \frac{\delta_n C^2}{\alpha^2}\, e^{\alpha x}(r_0 - x - r)\left[\alpha x\, e^{-\alpha(r_0-r-x)} - e^{-\alpha(r_0-r-x)} + e^{-\alpha(r_0-r)}\right]$$

$$P_2^{I_2} = \frac{\delta_n C^2}{\alpha^2}\, e^{\alpha x}(r_0 - x - r)\left[(\alpha x - 1)\, e^{-\alpha(r_0-r-x)} + e^{-\alpha(r_0-r-x)}\right] \qquad \text{(A.18)}$$

Note I_2 and I_3 are the same except for replacement of δ_n by δ_p so using equations (A.15) and (A.16)

$$P_2^{I_2} + P_2^{I_3} = \frac{(\delta_n + \delta_p)C^2}{\alpha^2}\, e^{-\sigma x}(r_0 - x - r)\left[(\alpha x - 1)\, e^{-\alpha(r_0-r-x)} + e^{-\alpha(r_0-r)}\right] \qquad \text{(A.19)}$$

From equation (A.16) we get the last term

$$P_2^{I_4} = \int_0^x dz\, e^{-\alpha z} \int_{r+z}^{\infty} dr'\, C\, e^{-\alpha(r'-z-r)}\delta_n(x-z)\, e^{-\sigma(x-z)}\, C\, e^{-\alpha(r_0-r')}$$

$$= \delta_n\, C^2\, e^{-\sigma x} \int_0^x dz(x-z)\, e^{-\alpha(r_0-r-z)} \int_r^{r_0-z} dr'$$

$$= \delta_n\, C^2\, e^{-\sigma x}(r_0 - r - x)\, e^{-\alpha(r_0-r)} \int_0^x (x-z)\, e^{\alpha z} dz$$

$$P_2^{I_4} = \delta_n\, C^2\, e^{-\sigma x}(r_0 - r - x)\, e^{-\alpha(r_0-r)}\frac{1}{\alpha^2}\left[-1 - \alpha x + e^{\alpha x}\right] \tag{A.20}$$

Combining terms we write the second order perturbation term from equations (A.17), (A.19), and (A.20)

$$\begin{aligned} P_2 &= P_2^{I_1} + P_2^{I_2} + P_2^{I_3} + P_2^{I_4} \\ &= C^2\delta_p\frac{x^2}{2}\, e^{-\alpha x}(r_0 - r - x)e^{-\alpha(r_0-r-x)} \\ &\quad + \frac{(\delta_n + \delta_p)}{\alpha^2}C^2 e^{-\sigma x}(r_0 - r - x)e^{-\alpha(r_0-r-x)}\left[(\alpha x - 1) + e^{-\alpha x}\right] \\ &\quad + \delta_n\frac{C^2}{\alpha^2}\, e^{-\sigma x}(r_0 - r - x)e^{-\alpha(r_0-r-x)}\left[-e^{-\alpha x}(\alpha x + 1) + 1\right] \end{aligned} \tag{A.21}$$

Let

$$M \equiv C^2\, e^{-\alpha x}(r_0 - r - x)e^{-\alpha(r_0-r-x)} \tag{A.22}$$

$$\begin{aligned} P_2 = M \bullet \Bigg[\delta_p\frac{x^2}{2} + \frac{\delta_n + \delta_p}{\alpha^2}\left\{(\alpha x - 1) + e^{-\alpha x}\right\} \\ + \frac{\delta_n}{\alpha^2}\left\{1 - e^{-\alpha x}(\alpha x + 1)\right\}\Bigg] \end{aligned} \tag{A.23}$$

or

$$P_2 = M \bullet \left[\delta_p\left\{\frac{x^2}{2} + \frac{1}{\alpha^2}\left(\alpha x - 1 + e^{-\alpha x}\right)\right\} + \delta_n\frac{x}{\alpha}(1 - e^{-\alpha x})\right] \tag{A.24}$$

The expression for second order neutrons can be written

$$\begin{aligned} N_2(x,r) = \int_0^x dz\, e^{-\sigma z}\Bigg\{\int_r^\infty \overline{F}_{np}(r,r')P_1(x-z,r')dr' \\ + \int_r^\infty \overline{F}_{nn}(r,r')N_1(x-z,r')dr'\Bigg\} \end{aligned}$$

Again noting our assumptions that $\overline{F}_{pp} = \overline{F}_{nn} = \overline{F}_{pn} = \overline{F}_{np}$ we write

$$N_1 + P_1 = I_1 + I_2 + I_3 + I_4$$

using equations (A.9) and (A.13) we write

$$N_1 + P_1 = \underbrace{\delta_p x C\ e^{-\sigma x} e^{-\alpha(r_0-r-x)}}_{I_1} + \underbrace{\frac{(\delta_n+\delta_p)C}{\alpha} e^{-\alpha x}\left[e^{-\alpha(r_0-r-x)} - e^{-\alpha(r_0-r)}\right]}_{I_2+I_3}$$

$$+ \underbrace{\delta_n x C\ e^{-\sigma x}\ e^{-\alpha(r_0-r)}}_{I_4} \tag{A.25}$$

or

$$= xC\ e^{-\sigma x} e^{-\alpha(r_0-r-x)}\left[\delta_p + \delta_n e^{-\alpha x}\right]$$
$$+ \frac{(\delta_n+\delta_p)}{\alpha}\ C\ e^{-\sigma x}\ e^{-\alpha(r_o-r-x)}\left[1 - e^{-\alpha x}\right] \tag{A.26}$$

$$N_2^{I_1} = \int_0^x dz\ e^{-\sigma z} \int_r^\infty C\ e^{-\alpha(r'-r)} \delta_p(x-z) C\ e^{-\sigma(x-z)}\ e^{-\alpha(r_0-r'-x+z)} dr'$$

$$= \int_0^x dz\ e^{-\sigma x}\ C^2 \delta_p(x-z) \int_r^{r_0-x} dr'\ e^{\alpha(r_0-r-x+z)}$$

where upper limit $r_0 - x$ has been imposed

$$= \int_0^x dz\ e^{-\sigma x} C^2 \delta_p(x-z)\,(r_0-r-x) e^{-\alpha(r_0-r-x+z)}$$

$$= \delta_p C^2 e^{-\sigma x}(r_0-r-x)\ e^{-\alpha(r_0-r-x)} \int_0^x dz(x-z)e^{-\alpha z}$$

$$= \delta_p C^2 e^{-\sigma x}(r_0-r-x) e^{-\alpha(r_0-r-x)}\left[-\frac{1}{\alpha^2} + \frac{e^{-\alpha x}}{\alpha^2} + \frac{\alpha x}{\alpha^2}\right]$$

$$N_2^{I_1} = \frac{\delta_p C^2 e^{-\sigma x}}{\alpha^2}(r_0-r-x)\ e^{-\alpha(r_0-r-x)}\left[-1 + \alpha x + e^{-\alpha x}\right] \tag{A.27}$$

$$N_2^{I_2+I_3}(x,r) = \int_0^x dz\, e^{-\sigma z} \int_r^\infty C\, e^{-\alpha(r'-r')}\ \frac{(\delta_n+\delta_p)}{\alpha}\ C\, e^{-\sigma(x-z)}\left[e^{-\alpha(r_0-r'-x+z)}\ - e^{-\alpha(r_0-r')}\right]$$

$$= \int_0^x dz \, \frac{(\delta_p + \delta_n)}{\alpha} \, C^2 \, e^{-\sigma x} \int_r^{r_0 - x} dr' \, e^{+\alpha r} \left[e^{-\alpha(r_0 - x + z)} - e^{-\alpha r_0} \right]$$

$$= \int_0^x dz \, \frac{(\delta_p + \delta_n)}{\alpha} \, C^2 \, e^{-\sigma x} \, (r_0 - x - r) e^{-\alpha(r_0 - r)} \left[e^{-\alpha(z-x)} - 1 \right]$$

$$= \frac{(\delta_p + \delta_n)}{\alpha} \, C^2 \, e^{-\sigma x} \, (r_0 - x - r) e^{-\alpha(r_0 - r)} \int_0^x dz \left[e^{-\alpha(z-x)} - 1 \right] \tag{A.28}$$

$$N_2^{I_2 + I_3} = \frac{(\delta_p + \delta_n)}{\alpha^2} \, C^2 \, e^{-\sigma x} \, (r_0 - x - r) e^{-\alpha(r_0 - r)} \left[e^{\alpha x} - (\alpha x + 1) \right] \tag{A.29}$$

$$N_2^{I_4}(x, r) = \int_0^x dz \, e^{-\sigma z} \int_r^{\infty} C \, e^{-\alpha(r' - r)} \, \delta_n(x - z) C \, e^{-\sigma(x - z)} \, e^{-\alpha(r_0 - r')} dr'$$

$$= \int_0^x dz \, C^2 \delta_n \, e^{-\sigma x} (x - z) \int_r^{r_0 - x} e^{-\alpha(r_0 - r)} dr'$$

$$= \int_0^x dz \, C^2 \, \delta_n \, e^{-\sigma x} (x - z)(r_0 - x - r) e^{-\alpha(r_0 - r)}$$

$$= C^2 \, \delta_n \, e^{-\sigma x} (r_0 - x - r) e^{-\alpha(r_0 - r)} \int_0^x (x - z) dz$$

$$N_2^{I_4} = C^2 \, \delta_n \, e^{-\sigma x} (r_0 - x - r) e^{-\alpha(r_0 - r)} \, \frac{x^2}{2} \tag{A.30}$$

Combining terms we write the second order neutrons using equations (A.27), (A.29), and (A.30) as

$$N_2(x, r) = \frac{\delta_p \, C^2 \, e^{-\sigma x}}{\alpha^2} \, (r_0 - r - x) e^{-\alpha(r_0 - r - x)} \left[-1 + \alpha x + e^{-\alpha x} \right]$$

$$+ \frac{(\delta_p + \delta_n)}{\alpha^2} \, C^2 \, e^{-\sigma x} \, (r_0 - r - x) e^{-\alpha(r_0 - r - x)} \left[1 - e^{-\alpha x} (\alpha x + 1) \right]$$

$$+ \frac{\delta_n \, C^2}{2} \, e^{-\sigma x} \, (r_0 - x - r) e^{-\alpha(r_0 - r - x)} x^2 \, e^{-\alpha x} \tag{A.31}$$

$$N_2(x,r) = C^2\, e^{-\sigma x}(r_0 - r - x)e^{-\alpha(r_0-r-x)} \left[\frac{\delta_p}{\alpha^2}(-1+\alpha x + e^{-\alpha x}) + \frac{(\delta_p+\delta_n)}{\alpha^2}\left[1 - e^{-\alpha x}(\alpha x+1)\right] + \frac{\delta_n}{2}\, x^2\, e^{-\alpha x}\right]$$

Recalling the definition for M from equation (A.22)

$$N_2 = M \bullet \left[\frac{\delta_p}{\alpha^2}\left((\alpha x - 1) + e^{-\alpha x}\right) + \frac{(\delta_p+\delta_n)}{\alpha^2}\left[1 - e^{-\alpha x}(\alpha x+1)\right] + \frac{\delta_n}{2}\, x^2\, e^{-\alpha x}\right] \tag{A.32}$$

The total second order fluence from equations (A.24) and (A.32) can be written

$$P_2 + N_2 = M \bullet \left[\frac{(2\delta_p+\delta_n)}{\alpha^2}\left\{(\alpha x - 1) + e^{-\alpha x}\right\} + \frac{(\delta_p+2\delta_n)}{\alpha^2}\left\{1 - e^{-\alpha x}(\alpha x+1)\right\} + \frac{(\delta_p+\delta_n\, e^{-\alpha x})}{2}\,\frac{x^2}{2}\right] \tag{A.33}$$

Summary

$$P_0(x,r) = e^{-\sigma x}\hat{\delta}_p(r_0 - r - x)\delta_p \tag{A.34}$$

$$N_0(x,r) = e^{-\sigma x}\hat{\delta}_n(r_0 - r - x)\delta_n \tag{A.35}$$

Let

$$G(x,r) \equiv C\, e^{-\sigma x}\, e^{-\alpha(r_0-r-x)} \tag{A.36}$$

$$P_1(x,r) = G(x,r)\left[x\delta_p + \frac{\delta_n}{\alpha}\left(1 - e^{-\alpha x}\right)\right] \tag{A.37}$$

$$N_1(x,r) = G(x,r)\left[x\delta_n\, e^{-\alpha x} + \frac{\delta_p}{\alpha}\left(1 - e^{-\alpha x}\right)\right] \tag{A.38}$$

Let

$$H(x,r) = C(r_0 - r - x) \tag{A.39}$$

$$P_2(x,r) = G(x,r)H(x,r)\left[\delta_p \frac{x^2}{2} + \frac{(\delta_n + \delta_p)}{\alpha^2}\left\{(\alpha x - 1) + e^{-\alpha x}\right\} + \frac{\delta_n}{\alpha^2}\left\{1 - e^{-\alpha x}(\alpha x + 1)\right\}\right] \tag{A.40}$$

$$N_2(x,r) = G(x,r)H(x,r)\left[\frac{\delta_p}{\alpha^2}\left\{(\alpha x - 1) + e^{-\alpha x}\right\} + \frac{(\delta_p + \delta_n)}{\alpha^2}\left\{1 - e^{-\alpha x}(\alpha x + 1)\right\} + \delta_n \frac{x^2}{2} e^{-\alpha x}\right] \tag{A.41}$$

Results

The analytical benchmarks obtained in this appendix have been compared with BRYNTRN runs for 100 MeV monoenergetic protons incident on a water slab.[112] Figure 31 shows a qualitative surface plot of the analytic secondary proton flux $\psi_p^s(x,E)$. The production spectrum is obtained from the quasi-elastic approximation

$$F(E,E') = C \exp\left[-\alpha(E' - E)\right]$$

where the constant $C = \alpha\sigma$. In BRYNTRN we approximate the secondary production term

$$\overline{F}(r + z, r_0 - x + z)$$

with

$$\overline{F}(r + z, r_0 - x + Q)$$

where Q is a constant. Using the same kind of error minimization analysis we applied to the continuous case in Chapters 3 and 4, we can find an optimum value for Q in the monoenergetic case.

Figure 32 shows the BRYNTRN flux for a value of $Q = 0$ and figure 33 plots the error as the difference between BRYNTRN and the analytical benchmark. Figure 34 shows this BRYNTRN flux for a value of $Q = h$, where h is the step size for the numerical marching

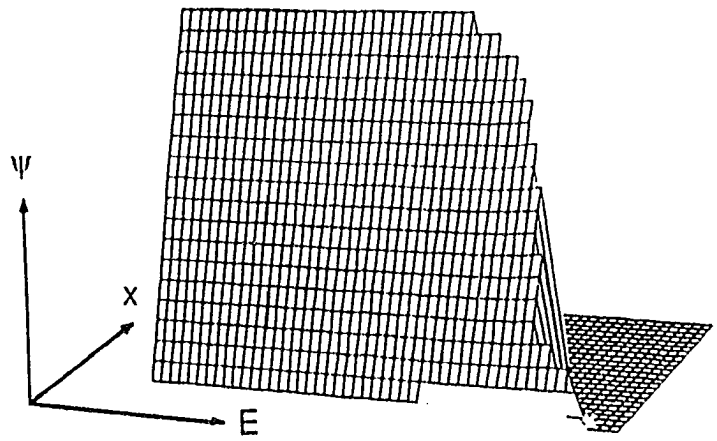

Figure 31 Analytic solution of proton-scaled flux for monoenergetic beam of incident protons of 100 MeV.

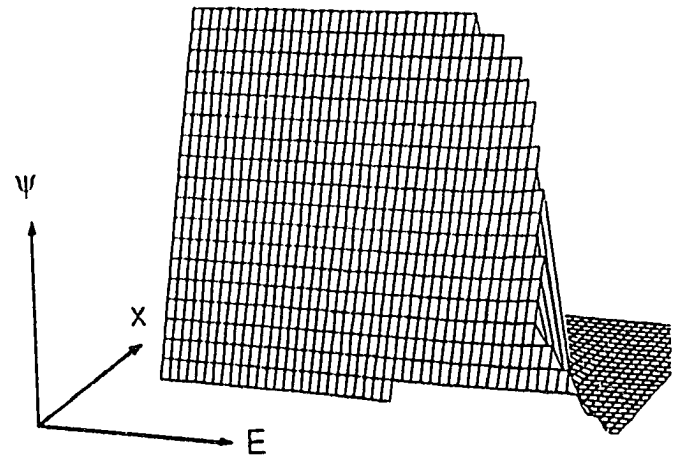

Figure 32 Numerical solution with $Q = 0$ of proton-scaled flux for monoenergetic beam of incident protons of 100 MeV.

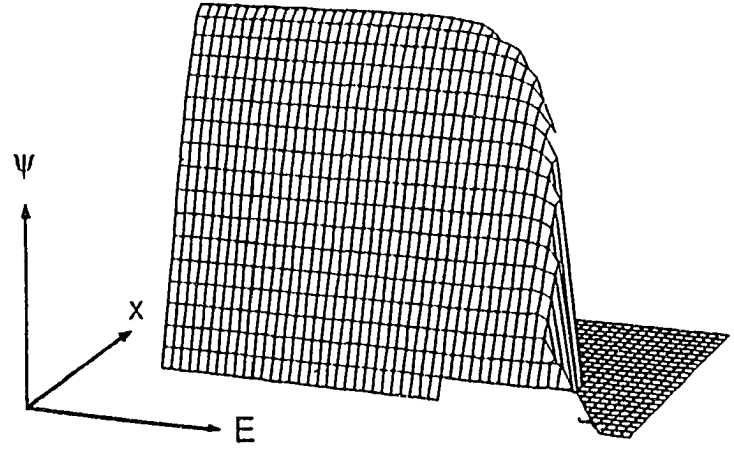

Figure 34 Numerical solution with $Q = h$ of proton-scaled flux for monoenergetic beam of incident protons of 100 MeV.

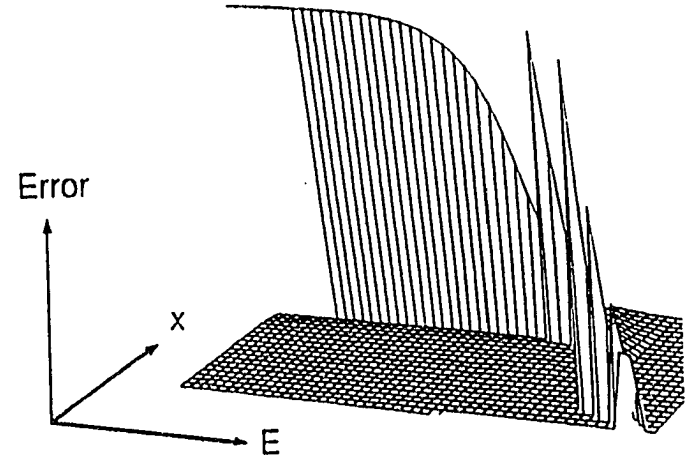

Figure 33 Numerical solution with $Q = 0$ of error in proton-scaled flux.

scheme. The error plot in figure 35 shows this Q value to be a better choice than $Q = 0$. Comparing figures 33 and 35 shows the sensitivity error of the choice of Q. We expect the optimum Q value to lie between these two choices.

The minimized value, based on our analysis method, is $Q = \frac{1}{2}h$ (see table 3). The flux for this case is shown in figure 36 and the corresponding error plot is displayed in figure 37. We see that this choice does, indeed, provide significantly better error behavior than either $Q = 0$ or $Q = h$.

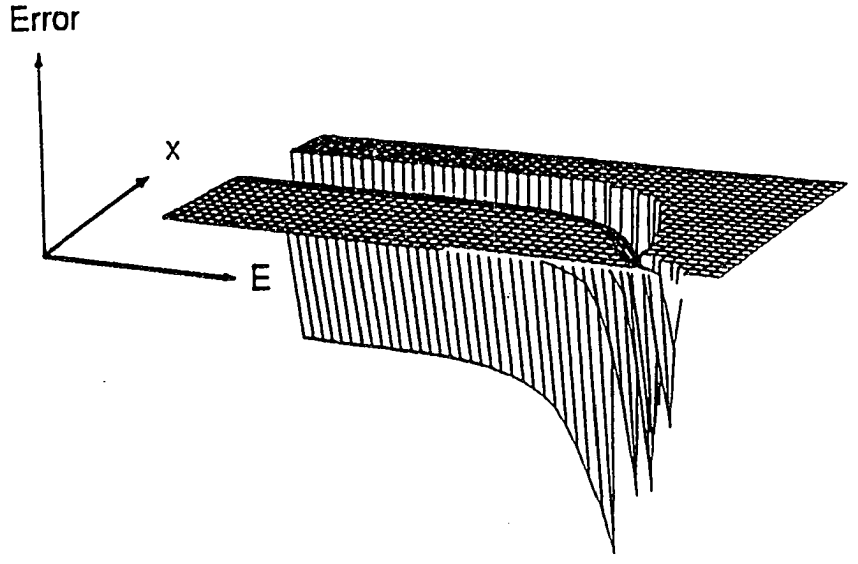

Figure 35 Error in proton-scaled flux solution with $Q = h$.

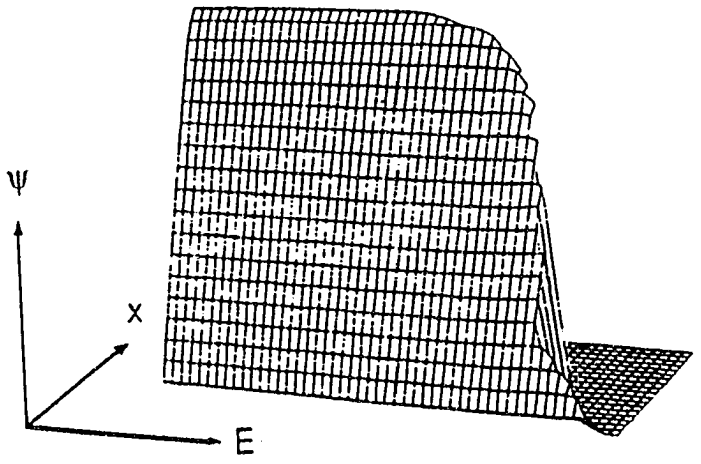

Figure 36 Numerical solution with $Q = h/2$ of proton-scaled flux for monoenergetic beam of incident protons of 100 MeV.

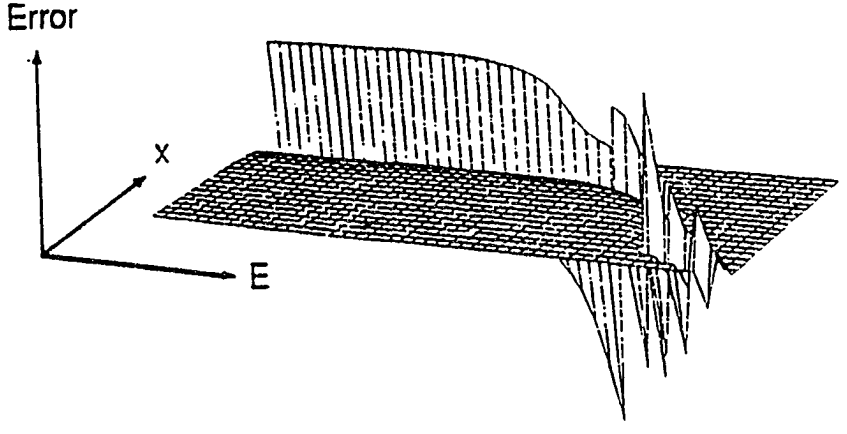

Figure 37 Front view of error in proton-scaled flux solution with $Q = h/2$.

Appendix B. NEUTRON ELASTIC SCATTERING

Successful utilization of the BRYNTRN code in space transport simulation is limited by space and energy grid resolution requirements. The numerical operation count associated with calculation of the particle production kernel scales with the square of the number of energy grid points. This limitation is not generally important for nuclear fragmentation processes since large energy transfer processes are involved and coarse grid resolution is acceptable. Elastic scattering, however, is particularly sensitive to energy resolution. The energy transfer between a projectile nucleon and a heavy target nucleus (e.g., Aluminum) is kinematically limited to a narrow range. Without suitable resolution, particles are not conserved using the transport model. The colliding particle is subtracted from the beam as desired but the secondaries due to elastic scattering are unresolved and therefore not added back into the beam. This problem is less important for proton transport since the mean free nuclear path is long compared to 'stopping' processes. Neutrons, on the other hand, are not degraded by electronic processes and penetrate deeply into the target material. Elastically scattered neutrons do not, of course, produce new particles. However, most elastic collisions do not deflect the projectile neutron sufficiently to remove it from the beam. In this context the straight ahead approximation is thought of as a small element of solid angle narrowly defined about the forward scattering direction. These 'rescattered' projectile neutrons should be added back into the particle flux term as secondaries. In this chapter we will develop a physically motivated method for estimating secondary production due to neutron elastic scattering processes using a relatively coarse energy grid.

We first provide an estimate of the resolution needed to capture secondary production due to elastic scattering. We consider a beam of incident neutrons incident on an aluminum slab. These primaries are distributed in energy using a Webber spectrum.[104,108] The maximum energy is 500 MeV. All interaction processes, other than the elastic channel, are turned off

so no fragmentation created secondaries will be produced. Tables 4–9 shows the integral particle spectrum for primaries and secondaries as function of penetration depth.

$$\Phi(x) = \int_0^{E_{\max}} \phi(x, E)\, dE$$

The energy grid is uniformly spaced. Results are shown for grids containing 30, 100, 500, 1000, 2000, and 3000 points. The 30 and 100 point grids recover essentially no 'rescattered' secondary neutrons. The 500 point grid produces some particles but the 1000 point grid recovers an order of magnitude more secondaries. The change in secondary production at 1 g/cm^2 between 2000 points and 3000 points is about 30% which indicates a movement towards convergence. Table 10 indicates particle conservation at 1 g/cm^2 for 500–3000 points. Dividing the sum of primaries and secondaries by the incident flux shows that the error ranges from 6% at 500 points to $< 2\%$ at 3000 points. The cost of this extra effort is shown in table 11. To propagate the 3000 point case 1 g/cm^2 into Aluminum requires approximately 10,000 cpu seconds on a CRAY-2 and 40 million words of storage. We seek a correction term which will resolve elastic scattering using 100 points or less. Our approach will consider an asymptotic analysis of the production kernel to estimate the required correction. In the next section we outline the elastic scattering process.

Elastic Scattering of Neutrons

Elastic scattering channels operate over the entire range of nucleon-target interaction energies. The incident particle is considered to be a plane wave. Two body nucleon-nucleon interactions are modeled using wave functions for the bound nucleus. Elastic scattering results in no change of the state for the nucleus. The interaction scattering crossection is modeled by using the Born term of the optical model.[6]

$$\begin{aligned} \frac{d\sigma_I}{dq^2} &= C \exp(-2bq^2) |F_A(q^2)|^2 \\ &\approx C \exp(-2bq^2) \exp\left(\frac{-2a^2q^2}{3}\right) \end{aligned} \tag{B.1}$$

Table 4. Primary and Rescattered Integrated Neutron Fluence as a Function of Penetration Depth in Aluminum Slab Using the BRYNTRN Code. Uniformly Spaced Energy Grid with 30 Points

x, g/cm^2	Fluence, #/cm^2	
	Primary	Rescattered
0	.8010E10	0
1	.7473E10	0
2	.6950E10	0
3	.6485E10	0
4	.6030E10	0
5	.5626E10	0

Table 5. Primary and Rescattered Integrated Neutron Fluence as a Function of Penetration Depth in Aluminum Slab Using the BRYNTRN Code. Uniformly Spaced Energy Grid with 100 Points

x, g/cm^2	Fluence, #/cm^2	
	Primary	Rescattered
0	.9477E10	0
1	.8845E10	.8000E-1
2	.8274E10	.1180E0
3	.7758E10	.1545E0
4	.7289E10	.1661E0
5	.6862E10	.1894E0

Table 6. Primary and Rescattered Integrated Neutron Fluence as a Function of Penetration Depth in Aluminum Slab Using the BRYNTRN Code. Uniformly Spaced Energy Grid with 500 Points

x, g/cm^2	Fluence, #/cm^2	
	Primary	Rescattered
0	.1033E11	0
1	.9794E10	.7955E7
2	.9289E10	.1542E8
3	.8815E10	.2243E8
4	.8368E10	.2901E8
5	.7949E10	.3516E8

Table 7. Primary and Rescattered Integrated Neutron Fluence as a Function of Penetration Depth in Aluminum Slab Using the BRYNTRN Code. Uniformly Spaced Energy Grid with 1000 Points

x, g/cm^2	Fluence, #/cm^2	
	Primary	Rescattered
0	.1040E11	0
1	.9808E10	.7775E8
2	.9257E10	.1504E9
3	.8745E10	.2181E9
4	.8269E10	.2813E9
5	.7825E10	.3401E9

Table 8. Primary and Rescattered Integrated Neutron Fluence as a Function of Penetration Depth in Aluminum Slab Using the BRYNTRN Code. Uniformly Spaced Energy Grid with 2000 Points

x, g/cm^2	Fluence, #/cm^2	
	Primary	Rescattered
0	.1042E11	0
1	.9880E10	.2054E9
2	.9368E10	.3984E9
3	.8888E10	.5796E9
4	.8436E10	.7497E9

Table 9. Primary and Rescattered Integrated Neutron Fluence as a Function of Penetration Depth in Aluminum Slab Using the BRYNTRN Code. Uniformly Spaced Energy Grid with 3000 Points

x, g/cm^2	Fluence, #/cm^2	
	Primary	Rescattered
0	.1043E11	0
1	.9896E10	.2723E9

Table 10. Particle Conservation as a Function of Energy Grid Mesh Density Using BRYNTRN to Elastically Scatter Neutrons in Aluminum.

1 g/cm^2 Penetration Depth

Energy Points	Incident Fluence	Primary and Rescatter at 1 g/cm^2	Conservation Ratio
500	.1033E11	.9802E10	.949
1000	.1040E11	.9886E10	.951
2000	.1042E11	.1009E11	.968
3000	.1043E11	.1024E11	.981

Table 11. Run Time Requirements For BRYNTRN Elastic Scattering Simulations as Function of Energy Grid Mesh Density Using CRAY-2 Computer

Energy Points	CRAY CPU Seconds	ΔE
30	3	16.7 MeV
500	77	1.0 MeV
1000	422	0.5 MeV
2000	2122	0.25 MeV
3000	9833	0.167 MeV

where $\vec{q}$ is the momentum transfer and $F_A(q^2)$ the nucleon form factor, and where b is the slope parameter given by (in units of GeV^{-2})

$$b = \begin{cases} 3 + 14\exp\left(\frac{-E'}{200}\right) \text{ [for } pp\text{]} \\ 3.5 + 30\exp\left(\frac{-E'}{200}\right) \text{ [for } pn\text{]} \end{cases} \tag{B.2}$$

E' is the initial energy of the nucleon in the lab frame and has units of MeV. a is the nuclear rms radius (in Fermi) given by

$$a = \sqrt{a_C^2 - 0.64} \tag{B.3}$$

where the rms charge radius (in Fermi) is

$$a_c = \begin{cases} 0.84 & (A_T = 1) \\ 2.17 & (A_T = 2) \\ 1.78 & (A_T = 3) \\ 1.63 & (A_T = 4) \\ 2.4 & (6 \leq A_T \leq 14) \\ 0.82A_T^{1/3} + 0.58 & (A_T \geq 16) \end{cases} \tag{B.4}$$

A_T is target mass. The nuclear form factor is the Fourier transform of the nuclear-matter distribution.

Let

$$B \equiv \frac{2mc^2 b}{10^6} \tag{B.5}$$

where mc^2 is the nucleon rest energy (938 MeV).

The energy transferred to the scattered nucleon is kinematically limited to

$$\alpha E' < E \leq E' \tag{B.6}$$

where

$$\alpha \equiv \frac{(A_T - 1)^2}{(A_T + 1)^2} \tag{B.7}$$

The nucleon spectrum is

$$f(E, E') = \frac{a_1 \exp\{-a_1(E' - E)\}}{1 - e^{-a_2 E'}} \tag{B.8}$$

where

$$\begin{cases} a_1 \equiv 4A_T mc^2 \left(B + \frac{a^2}{3}\right) \\ a_2 \equiv (1-\alpha)a_1 \end{cases} \tag{B.9}$$

so the secondary scattering term is given by

$$F(E,E') = \sigma_n(E')f(E,E') \tag{B.10}$$

where $\sigma_n(E')$ gives the total scattering crossection of the particles produced at E' due to elastic rescattering. Recall that the Boltzmann equation for neutron transport is

$$\begin{aligned} \left[\frac{\partial}{\partial x} + \sigma_n(E')\right] \phi_n(x,E) &= \int_E^\infty F(E,E')\phi_n(x,E')dE' \\ &\equiv G(x,E) \end{aligned} \tag{B.11}$$

Instead of transforming to x, r space and using $\psi(x,r)$, we will stay in x, E space and use $\phi(x,E)$. Use the integrating factor $e^{\sigma(E)x}$ so B.11 becomes

$$\begin{aligned} d\left[\phi_n e^{\sigma x}\right] &= e^{\sigma x'} G(x',E)dx' \\ e^{\sigma(E)x}\phi_n(x,E) - \phi_n(0,E) &= \int_0^x e^{\sigma(E)x'}dx' \int_E^\infty F(E,E')\phi_n(x,E')dE' \end{aligned} \tag{B.12}$$

so that

$$\begin{aligned} \phi_n(x,E) &= \phi_n(0,E)\, e^{-\sigma(E)x} \\ &\quad + \int_0^x dz e^{-\sigma(E)z}dz \int_E^\infty F(E,E')\phi_n(x-z,E')dE' \end{aligned} \tag{B.13}$$

We need an expression for $\phi(x,E)$ and $F(E,E')$.

Recall the perturbation analysis that led to equation 35. We can write B.13 as

$$\phi_n^i(x,E) = \int_0^x dz e^{-\sigma_n(E)z} \int_E^\infty F_{nn}(E,E')\phi_n^{i-1}(x-z,E')dE' \tag{B.14}$$

with primaries given by

$$\phi_n^0(x,E) = e^{-\sigma(E)x}\phi_n^0(0,E) \tag{B.15}$$

Using the functional form equation (B.8) for the elastic scattering kernel and letting $\phi_n^0(0,E) = \exp[-\beta E]$ we get the first order secondary fluence as

$$\phi_n^1(x,E) = \int_0^x dz e^{-\sigma_n z} \int_E^{E/\alpha} \frac{a_1 \sigma_n(E') e^{-a_1(E'-E)}}{1-e^{-a_2 E'}} e^{-\sigma_n(x-z)} e^{-\beta E'} dE' \tag{B.16}$$

Assuming σ_n is $\sim$ constant, we can write

$$\phi_n^1(x,E) = \sigma_n a_1 e^{-\sigma_n x} e^{a_1 E} x \int_E^{E/\alpha} \frac{e^{-(a_1+B)E'}}{1-e^{-a_2 E'}} dE' \tag{B.17}$$

Consider case where $e^{-a_2 E'} \ll 1$.

$$\phi_n^1(x,E) \sim \sigma_n a_1 e^{-\sigma_n x} e^{a_1 E} x \left. \frac{e^{-(a_1+\beta)E'}}{-(a_1+\beta)} \right]_E^{E/\alpha}$$

$$= (\ldots) \frac{1}{-(a_1+\beta)} \left[e^{-(a_1+\beta)E/\alpha} - e^{-(a_1+\beta)E} \right]$$

$$= \frac{(\ldots)}{-(a_1+\beta)} e^{-(a_1+\beta)E} \left[e^{-(a_1+\beta)E(\frac{1-\alpha}{\alpha})} - 1 \right] \tag{B.18}$$

For

$$\left[(a_1+B)E(\frac{1-\alpha}{\alpha}) \right] \gg 1$$

$$\phi_n^1(x,E) = \frac{\sigma_n a_1 x}{(a_1+\beta)} e^{-\sigma_n x} e^{-\beta E} \tag{B.19}$$

The second order term is

$$\phi_n^2(x,E) = \int_o^x dz e^{-\sigma_n z} \int_E^{e/\alpha} \sigma_n \frac{a_1 e^{-a_1(E'-E)}}{1-e^{-a_2 E'}} \left[\frac{a_1}{(a_1+\beta)} \right] x e^{-\sigma_n(x-z)} e^{-\beta E'} dE'$$

$$= \left[\frac{a_1 \sigma_n}{a_1+\beta} \right]^2 \frac{x^2}{2} e^{-\sigma_n x} e^{-\beta E} \tag{B.20}$$

to all orders we get

$$\phi_n(x,E) = e^{-\sigma_n x} \left[1 + \frac{a_1 \sigma_n x}{(a_1+\beta)} + \frac{1}{2} \left[\frac{a_1 \sigma_n x}{(a_1+\beta)} \right]^2 + \ldots \right] e^{-\beta E}$$

$$= \exp\left[\frac{a_1\sigma_n x}{(a_1+\beta)}\right] e^{-\sigma_n x} e^{-\beta E}$$

$$= \exp\left[-\sigma_n x\left(1-\frac{a_1}{(a+\beta)}\right)\right] e^{-\beta E} \tag{B.21}$$

but

$$1-\frac{a_1}{a_1+\beta} = \frac{\beta}{a_1+\beta} \sim \frac{\beta}{a_1}$$

$$\phi_n(x,E) \approx e^{\frac{-\sigma_n \beta x}{a_1}} e^{-\beta E}$$

$$\phi_n(x,E) = e^{-\beta(E+\delta E_0)} = \phi(0, E+\delta E) \tag{B.22}$$

where

$$\delta E_0 = \frac{\sigma_n x}{a_1}$$

As the average energy a_1 increases, δE_o decreases so for large values of E

$$\phi_n(x,E) \approx \phi(0,E)$$

which means that elastic scattering disappears at high energy. This means that the elastic scattering process at penetration depth x can be represented as an energy shift in the flux at the boundary. This result is, strictly speaking, applicable only to high energy scattering but provides insight for development of a mechanism to accommodate the entire energy range. The physical picture of elastic scattering in the straight ahead approximation (which we impose for 1-D transport) says that the scattered beam is confined to a narrow cone in the forward direction. Physically, this approximation holds for high kinetic energy. Each scattering interaction changes the incident energy by a small amount so that the beam flux can be represented as the incident beam, shifted downwards in energy by a term related to the distance traveled. This result provides a basis for the development of a correction turn for elastic scattering which is relatively insensitive to energy grid resolution.

Our approach describes the rescattering kernel by a set of discrete energy shifts. We know that

$$F(E,E') \equiv \sigma_n(E') f(E,E')$$

where σ_n is restricted here to the elastic scattering contribution. We wish to write the spectral distribution function as

$$f(E,E') = \sum_i f(E,E+\overline{Q}_i)\delta(E-E'+\overline{Q}_i) \tag{B.23}$$

where $\overline{Q}_i$ represents the required energy shift. The procedure for determining the required number of i terms is not completely clear. We know that the spectral behavior of the energy shift varies with projectile energy. At low kinetic energy the spectra is represented by a flat step function whose width varies with energy. At higher energies the spectra are sharply peaked about some particular value of energy transfer.

We do require that

$$\sum_i \overline{Q}_i f_i = \overline{Q} \tag{B.24}$$

and that f satisfy the normalization condition

$$\sum_i \frac{f_i}{G} = 1 \tag{B.25}$$

where G is a normalization constant. We can compute $\overline{Q}(E)$ as

$$\overline{Q}(E) = \frac{\int_0^{(\frac{1-\alpha}{\alpha})E} f(E+Q)QdQ}{\int_0^{(\frac{1-\alpha}{\alpha})E} f(E,E+Q)dQ} \tag{B.26}$$

consider the elastic scattering model represented by a single energy transfer for each scattering event. Then

$$\begin{aligned}\left[\frac{\partial}{\partial x}+\sigma_n(E)\right]\phi_n(x,E) &= \int_E^\infty \sigma_n(E')f(E,E')\phi_n(x,E')dE' \\ &\approx \int_E^\infty \sigma_n(E')\delta(E-E'+\overline{Q})\phi(x,E')dE' \\ &= \sigma_n(E+\overline{Q})\phi_n(x,E+\overline{Q})\end{aligned} \tag{B.27}$$

This model has the distinct advantage that 'rough' particle conservation is assured. However, the correct spectral distribution is not assured. The fluence is given as

$$\phi_n(x,E) = e^{-\sigma_n(E)x}\phi_n(0,E) + \sigma_n(E+\overline{Q})xe^{-\sigma_n(E)x}\phi_n(0,E+\overline{Q}) \tag{B.28}$$

where the second term on the rhs represents the rescattered secondaries. $\overline{Q}$ can be obtained from equation (B.26). Using the analytical expression (B8) for $f(E,E')$ and noting that $Q \ll E$ we can calculate $\overline{Q}$ to be approximately

$$\overline{Q}(E) = \frac{1}{a_1}\left[\frac{1-a_2E\exp[-a_2E]}{1-\exp[-a_2E]}\right] \tag{B.29}$$

To demonstrate the particle conserving character of our model we consider the case where

$$\sigma_n(E) = \sigma_n = \text{const}$$

$$\phi(0,E) = e^{-\beta E}$$

Then the fluence at x is given as

$$\begin{aligned}\phi_n(x,E) = {} & e^{-\sigma_n x}e^{-\beta E} + \sigma_n x e^{-\sigma x}e^{-(E+\overline{Q})} \\ & + \frac{1}{2}(\sigma_n x)^2 e^{-\sigma_n x}e^{-\beta(E+2\overline{Q})} + \ldots\end{aligned} \tag{B.30}$$

and the integrated fluence is

$$\begin{aligned}\int_0^\infty \phi_n(x,E)dE = {} & \int_0^\infty \phi_n(0,E)dE\left[e^{-\sigma_n x} + \sigma_n x\, e^{-\sigma_n x}e^{-\beta\overline{Q}}\right. \\ & \left. + \frac{1}{2}(\sigma x)^2\, e^{-\sigma_n x}e^{-2\beta\overline{Q}} + \ldots\right]\end{aligned} \tag{B.31}$$

For $\exp[-\beta\overline{Q}] \ll 1$ this gives

$$\sim \int_0^\infty \phi_n(0,E)dE\left[e^{-\sigma_n x}\{1+\sigma_n x + \frac{1}{2}(\sigma_n x)^2 + \ldots\}\right]$$

$$= \int_0^\infty \phi_n(0,E)dE\left[e^{-\sigma_n x + \sigma_n x}\right]$$

so that

$$\int_0^\infty \phi_n(x,E)dE \sim \int_0^\infty \phi_n(0,E)dE \tag{B.32}$$

We now have a particle preserving model for neutron elastic rescattering which is not intrinsically dependent on grid resolution. We apply this model to nucleon transport in the next section.

Results

In this section we apply the elastic rescattering model (B.28) and (B.29) in the BRYNTRN transport code. (B.28) is incorporated as a correction term for coarse grids (i.e., ≤ 100 energy points) which we have previously shown to be incapable of resolving the small energy transfers associated with elastic scattering. We will consider the case of neutrons normally incident on an aluminum slab. The incident neutron spectrum is specified by the Webber spectrum defined in equation (92). All particle scattering processes are deactivated except for elastic scattering. The energy grid is distributed logarithmically between $E_{\min} = 0.1$ MeV and $E_{\max} = 500$ MeV. Our test case uses 100 energy points. Twenty five points are distributed in the energy range below 10 MeV.

Table 12 illustrates the dependence of $\sigma_n(E)$ on energy for elastic scattering from aluminum. The crossection at 1 MeV is 2.5 times greater than at 50 MeV and a factor of approximately 6 greater than at 100 MeV.

Figure 38 shows the integrated fluence $\Phi(x) = \int_0^\infty \phi(x,E)dE$. The primaries exhibit the expected exponential decay as $\exp[-\sigma_n x]$. The rescattered neutrons grow at a rate that largely offsets the particle loss due to decay of the primaries. Figure 39 shows ratio $\Phi(x)/\Phi(0)$. The total number of neutrons is conserved to within one percent at a penetration depth of 10 g/cm^2. At 30 g/cm^2 the difference is about 3%. Some of this disagreement is due to numerical truncation error and some is due to the physical process of low energy neutron thermalization. Table 13 illustrates the effect of truncation error. The ratio $\Phi(x)/\Phi(0)$ is given for three values of integration step size h. For a deep penetration depth of 30 g/cm^2

Table 12. Elastic Scattering Cross Section for Neutrons Incident on Aluminum Target

E, MeV	$\sigma_n(E)$
0.01	.078
1	.069
5	.048
10	.028
15	.024
20	.024
50	.023
100	.014
200	.001

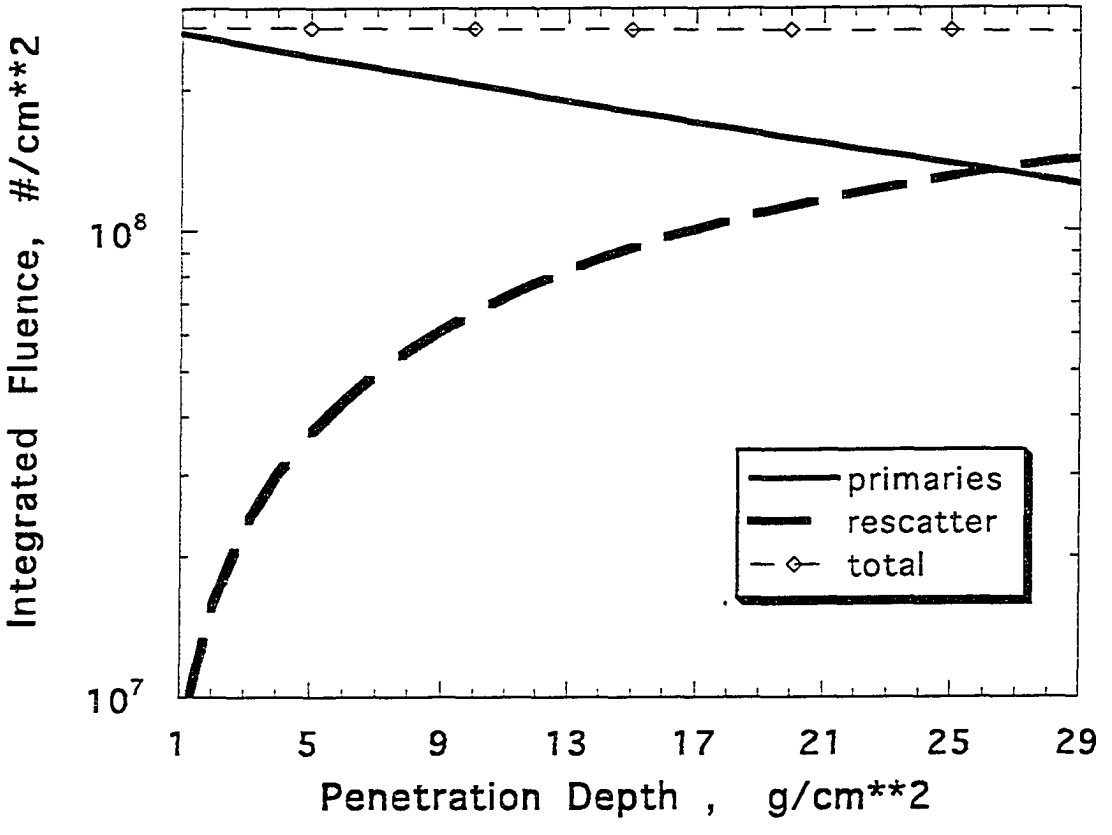

Fig. 38 Integrated Fluence. Elastically Scattered Neutrons in Aluminum Slab

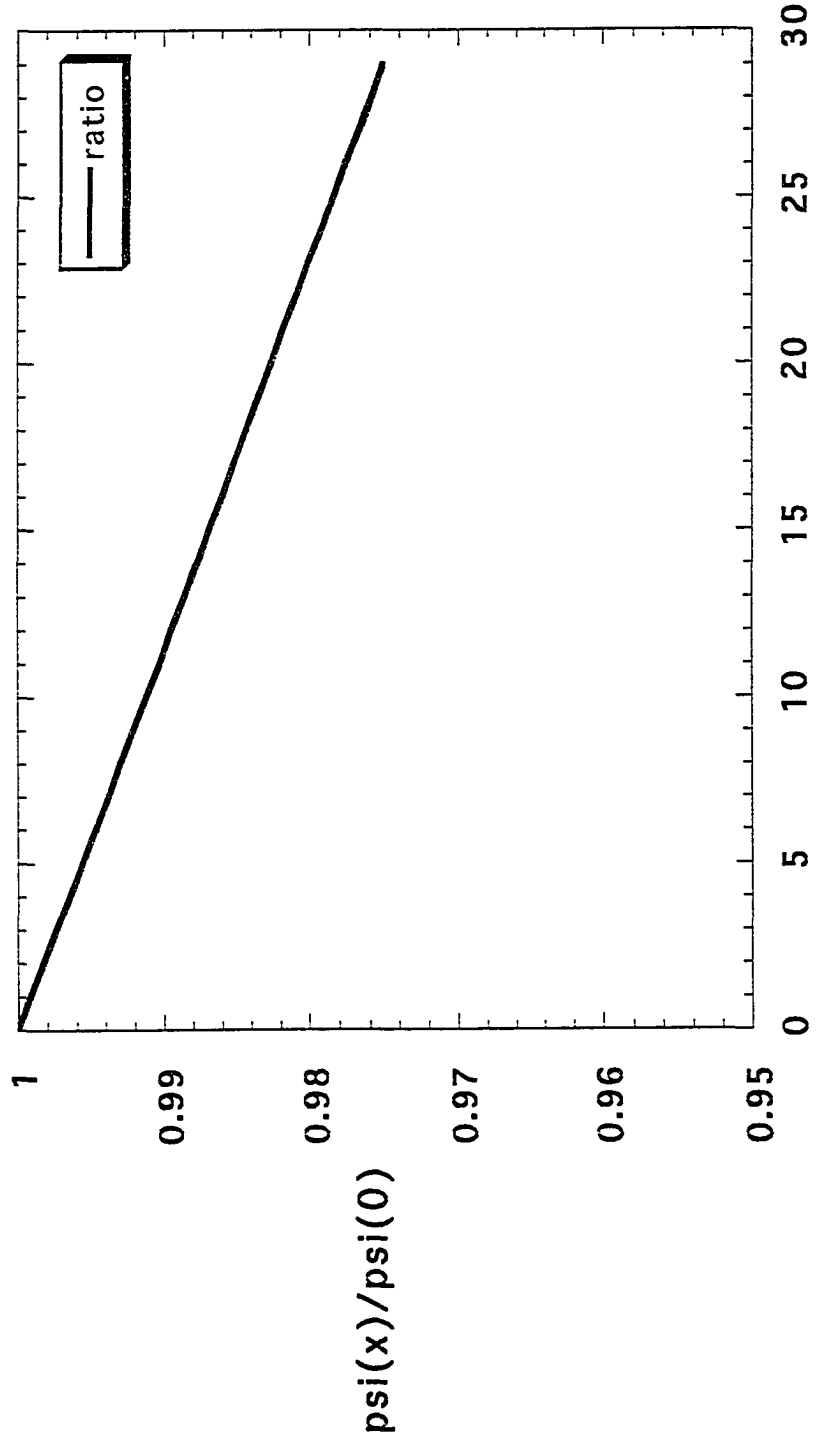

Fig. 39 Convergence Ratio. Elastically Scattered Neutrons in Aluminum.

Table 13. Integrated Spectrum Ratio $\Phi(x)/\Phi(0)$ as a Function of Step Size h. Logarithmically spaced E Grid with 100 Points.

x, g/cm^2	$\Phi(k)/\Phi(0)$		
	$h = .5$	$h = .25$	$h = .125$
1	.999	.999	.999
10	.991	.993	.993
20	.983	.985	.987
30	.975	.979	.981

the ratio changes by .5% from .975 to .979 as h is halved in value from .5 to .25. Halving h again to a value of .125 only changes the result by only .2%.

A set of runs were also performed using a 50 point energy grid in order to assess the effect of mesh density on the rescattering model. This grid distributes 8 energy points between 0–1 MeV and 24 points between 0–10 MeV. The 100 point energy grid distributed 14 points between 0-1 MeV and 27 points between 0–10 MeV. Table 14 illustrates the ratio $\Phi(x)/\Phi(0)$ for the 50 point energy grid. We see that, interestingly, the coarser 50 point grid provides the same convergence as the 100 point grid at all three values of h.

Figure 40 shows the integrated fluence for neutrons incident on a lead slab. The primary decay, and consequent growth of rescattered neutrons, is relatively slower than in Aluminum. In Aluminum the rescattered fluence surpasses the primary fluence at a depth of 27 g/cm^2. The primary fluence in lead is still significantly greater than the rescattered term even at a penetration depth of 29 g/cm^2.

Figure 41 shows the convergence ratio $\Phi(x)/\Phi(0)$ for neutrons in lead. Comparing figures 39 and 41 demonstrates that convergence in lead is better than in Aluminum. At a penetration depth of 29 g/cm^2 the convergence in lead is .996 compared with .975 in Aluminum. This result is related to the dependence of α (Eq. (B.7)) on target mass. As A_T increases, α approaches one and the kinematically allowed energy transfer due to elastic scattering approaches zero.

Figure 42 shows the spectral behavior of the neutron fluence in Aluminum at three penetraton depths (1, 10, and 29 g/cm^2). This includes the sum of the primary and rescattered terms. We observe a monotonic decay with increasing energy. The low energy behavior displays the 1/v [v = velocity] behavior characteristics of elastic scattering. We see that the spectra do not change as a function of penetration depth. However the separated spectra for the primary and rescattererd fluences do change with penetration depth. Figures 43 and 44 show the primary spectra for neutrons in Aluminum. The spectra for $E \leq 50$ MeV decays rapidly with increasing penetration depth. The curve for 29 g/cm^2

Table 14. Integrated Fluence as a Function of Penetration Depth for 500 MeV Neutrons Incident on an Aluminum Slab. Elastic Scattering Only.

50 Point Energy Grid

x, g/cm^2	$h = .5$ $\Phi(x)/\Phi(0)$	$h = .25$ $\Phi(x)/\Phi(0)$	$h = .125$ $\Phi(x)/\Phi(0)$
1	.999	.999	.999
10	.991	.993	.993
20	.983	.985	.987
30	.975	.979	.981

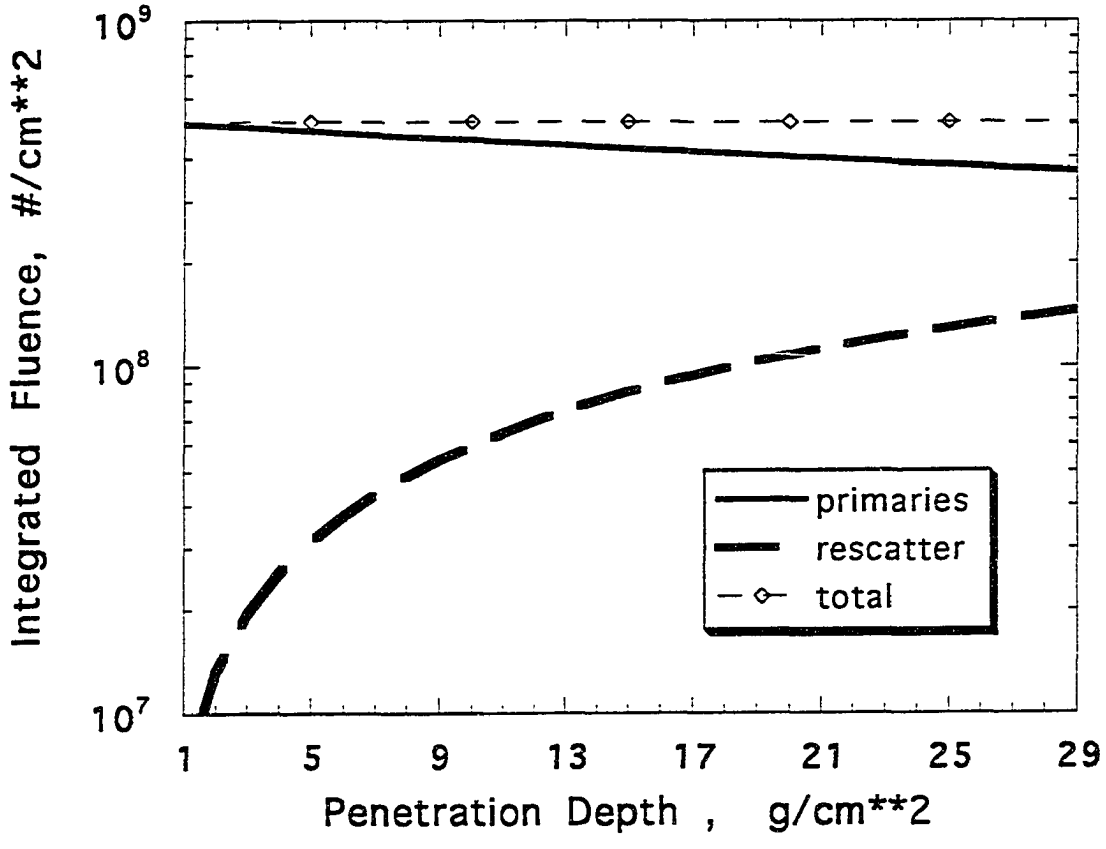

Fig. 40 Integrated Fluence. Elastically Scattered Neutrons in Lead Slab

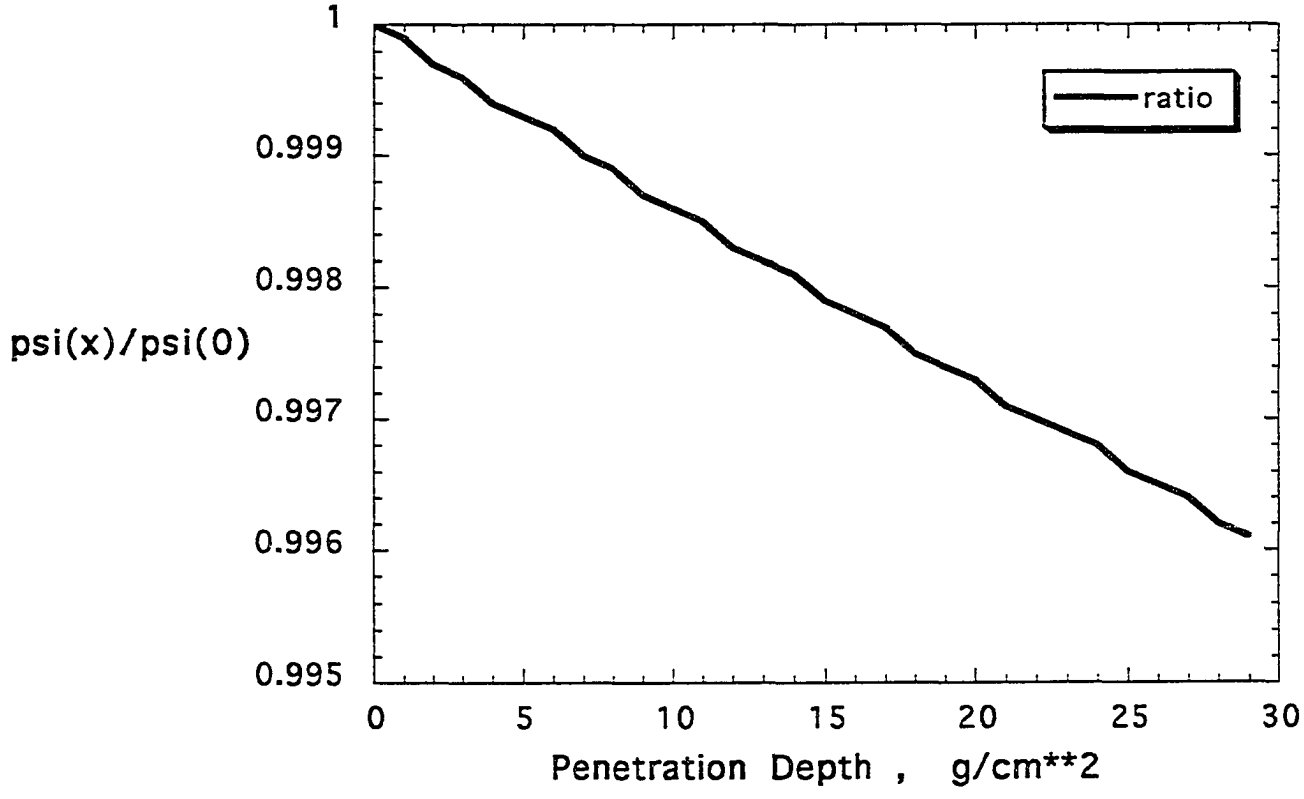

Fig. 41 Convergence Ratio. Elastically Scattered Neutrons in Lead.

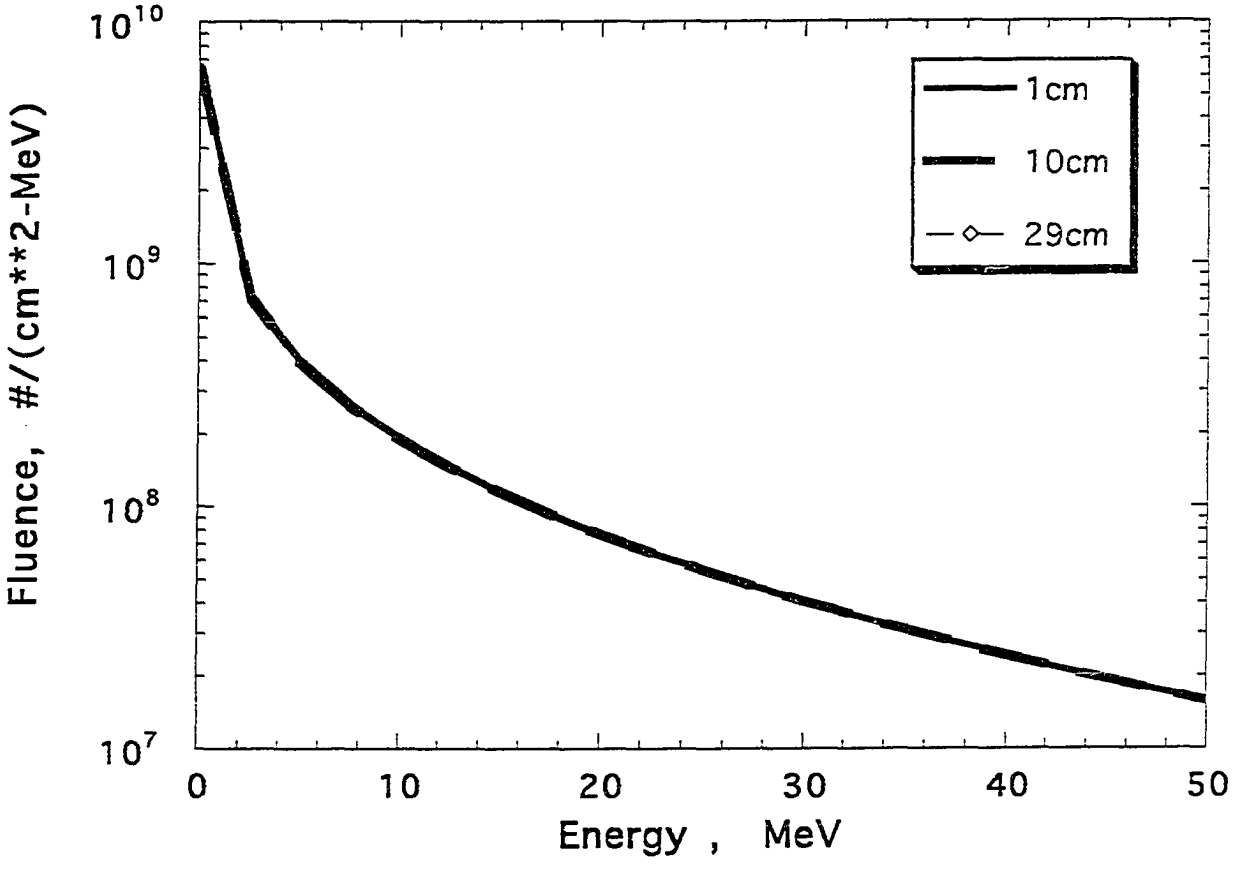

Fig. 42 Total Neutron Fluence as a Function of Energy for Several Penetration Depths. Neutrons Incident on Aluminum Slab.

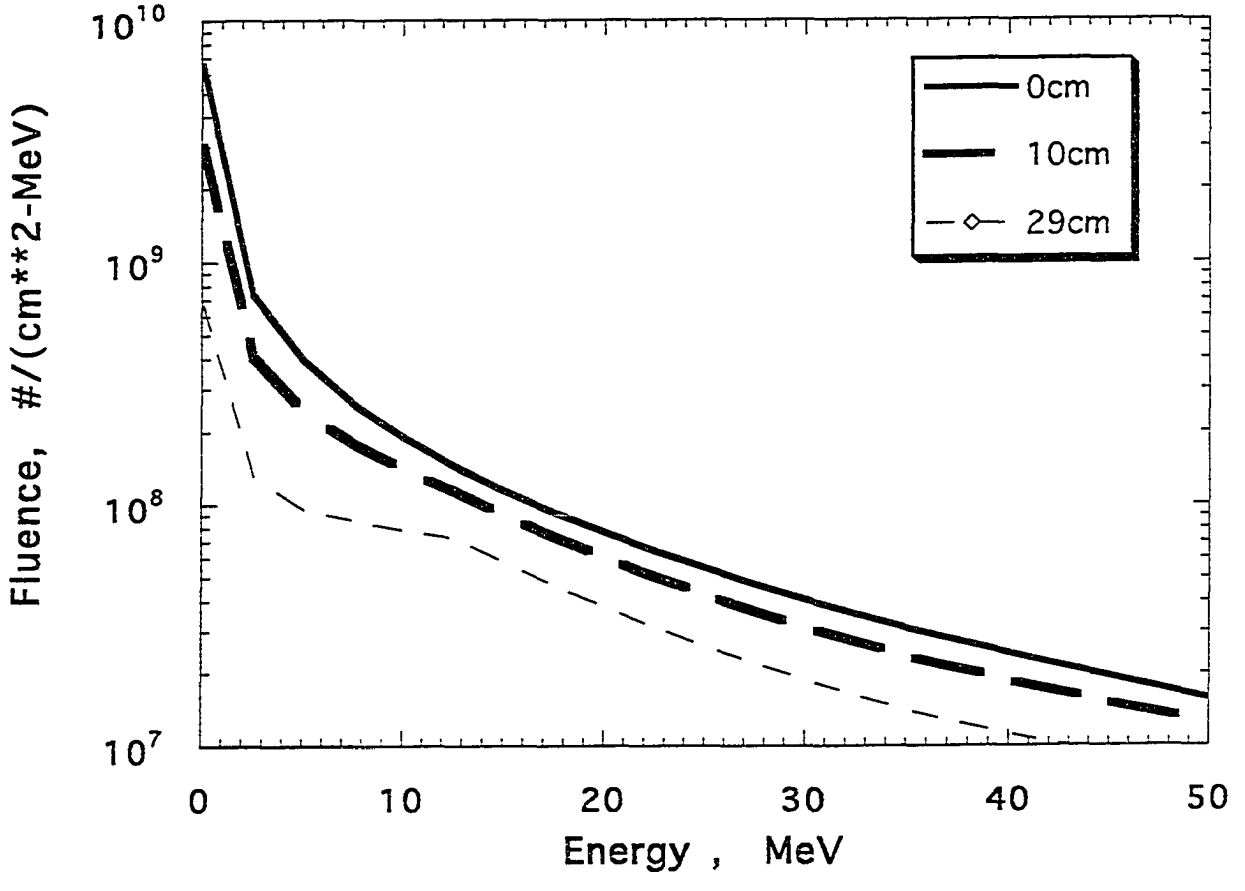

Fig. 43 Primary Neutron Fluence as a Function of Penetration Depth. Neutrons Incident on Aluminum Slab.

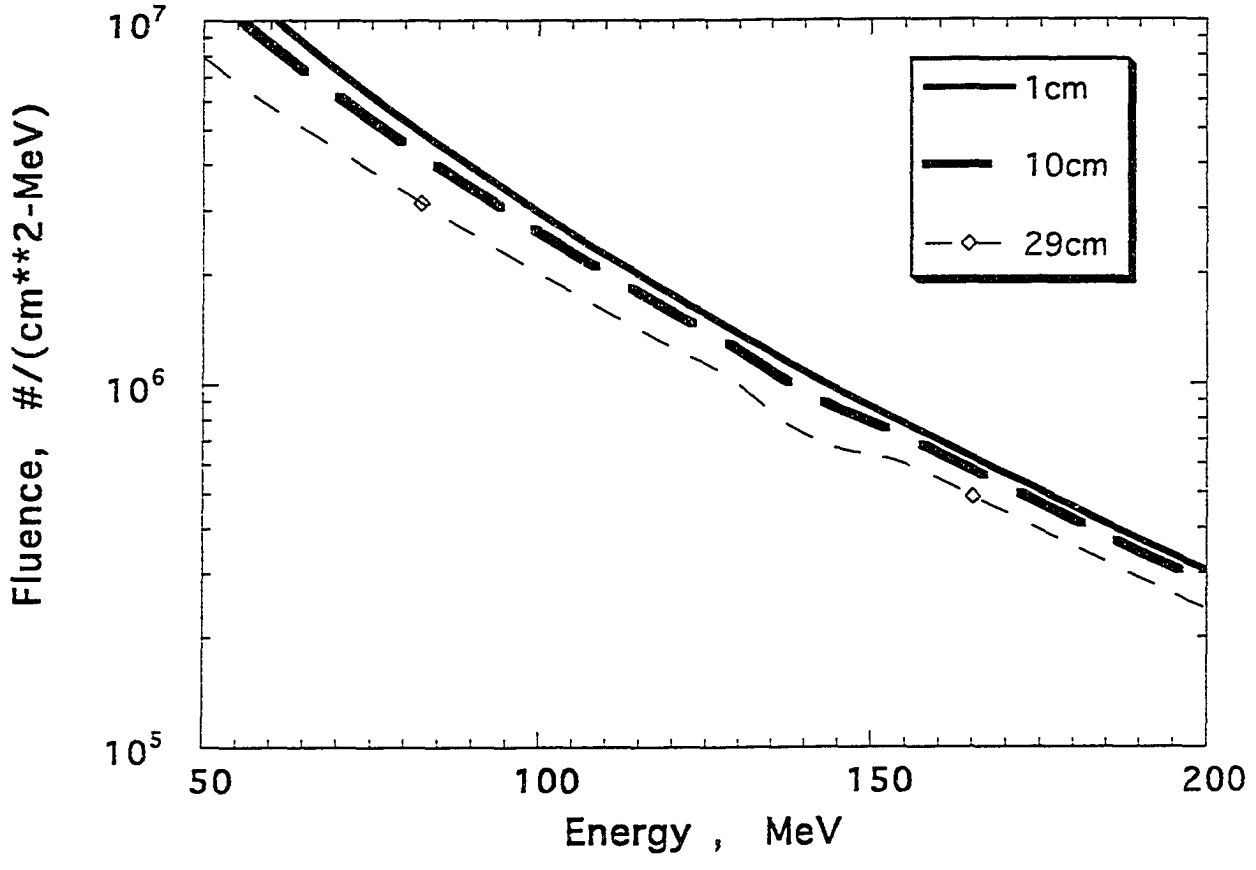

Fig. 44 Primary Neutron Fluence as a Function of Energy for Several Penetration Depths. Neutrons Incident on Aluminum Slab

shows a rapid fall-off between 0–2 MeV followed by a shoulder effect. The spectral behavior between 50–200 MeV is shown in figure 44. The effect of penetration depth is observed to be less pronounced at higher energies.

Figures 45 and 46 show the spectra for rescattered neutrons. The effect of increasing penetration depth is, not surprisingly, reversed with respect to the primary neutron behavior. We see that the 1 g/cm^2 curve is significantly lower than the 10 and 20 g/cm^2 curves at all energies. This effect is related to the fact that rescattered neutrons grow rapidly from an incident boundary value of zero to a relative equilibrium around 5–10 g/cm^2.

Figures 47–51 show a spectra for neutrons in lead. The results are qualitatively similar to the Aluminum results. However, the primary neutron spectra in lead is observed to be less sensitive to penetration depth than in Aluminum. Overall, our elastic scattering model produces qualitatively similar results for Lead and Aluminum. What happens if we employ a much lighter element as the target material?

Figure 52 shows the integrated fluence for neutrons in Beryllium ($A_T = 9$) using the BRYNTRN code with exactly the same conditions used for Aluminum and Lead. Comparing figure 52 with Aluminum (fig. 38) and Lead (fig. 40) we observe that the primaries decay rapidly in Beryllium. The neutron fluence at a penetration depth of 29 g/cm^2 in Beryllium is about 50% of the equivalent Aluminum value. Beryllium is known to be a good neutron moderator. What about the convergence behavior? Figure 53 shows that the model does a relatively poor job of conserving particles compared to Aluminum (fig. 39) and Lead (fig. 41). The conservation at 29 g/cm^2 is about 84% of the incident value. We also observe significant changes in the spectral character. Figure 54 shows the total (primary and rescattered) flux spectra for Beryllium at penetration depths of 1, 10, and 29 g/cm^2. Note the divergence of the curves at low energy and recall from figure 40 the equivalent Aluminum curves lay on top of each other over the entire energy range.

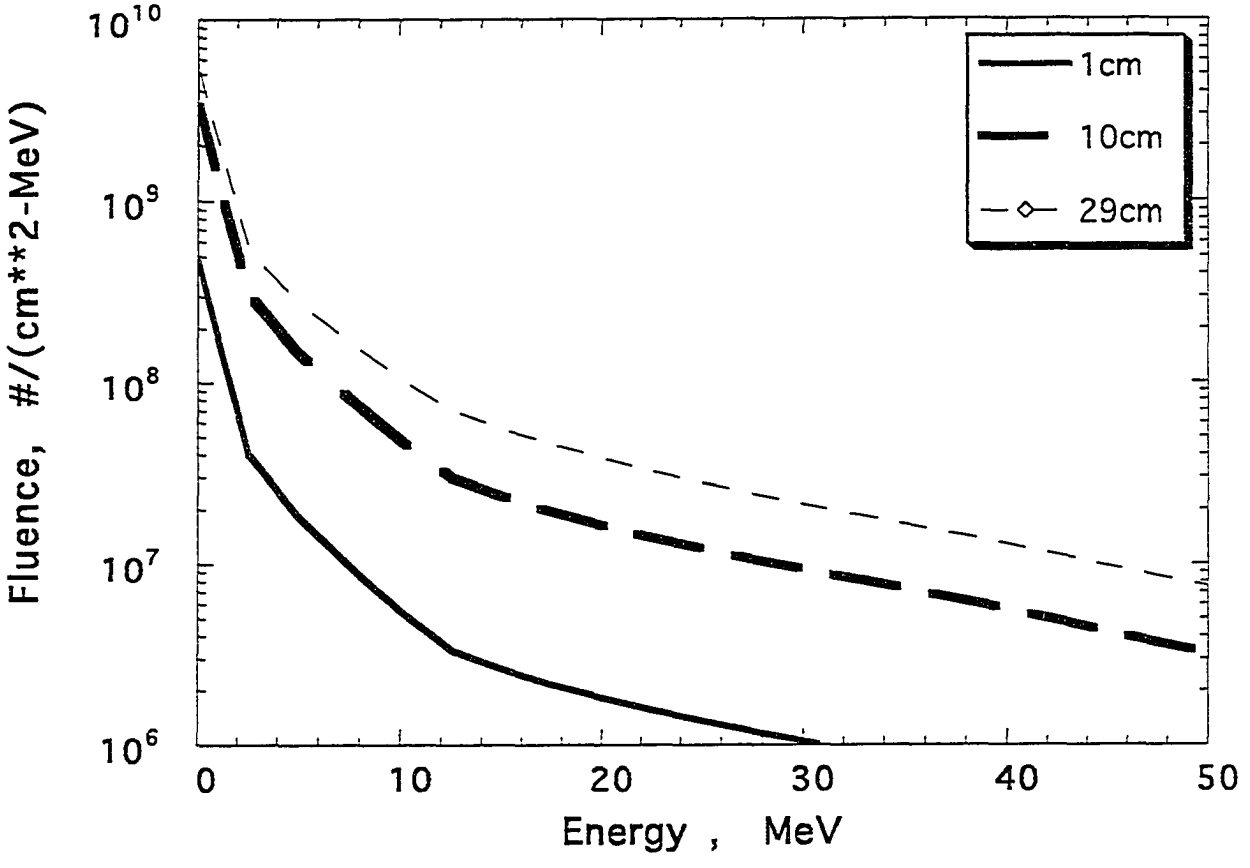

Fig. 45 Rescattered Neutron Fluence as a Function of Energy for Several Penetration Depths. Neutrons Incident on Aluminum Slab.

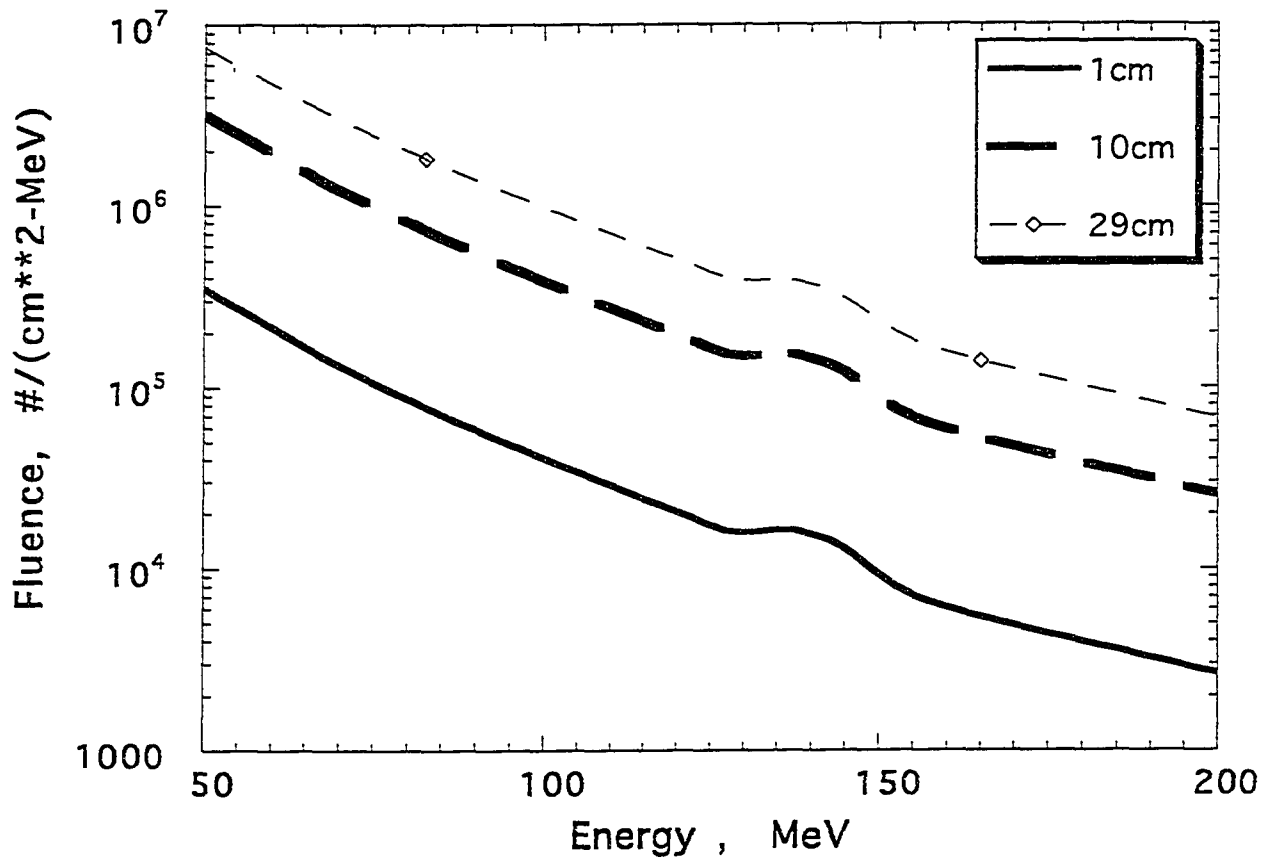

Fig. 46 Rescattered Neutron Fluence as a Function of Energy for Several Penetration Depths. Neutrons Incident on Aluminum Slab.

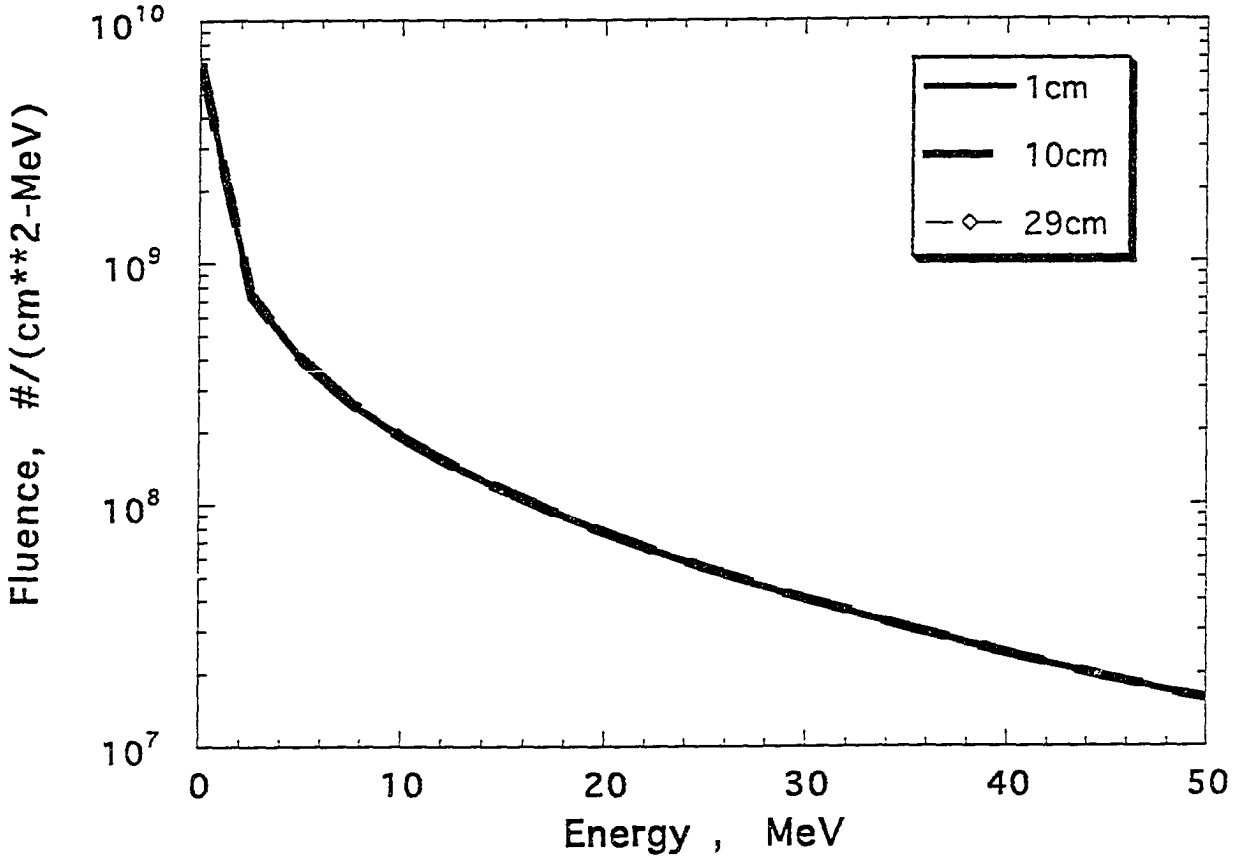

Fig. 47 Total Neutron Fluence as a Function of Energy for Several Penetration Depths. Neutrons Incident on Lead Slab.

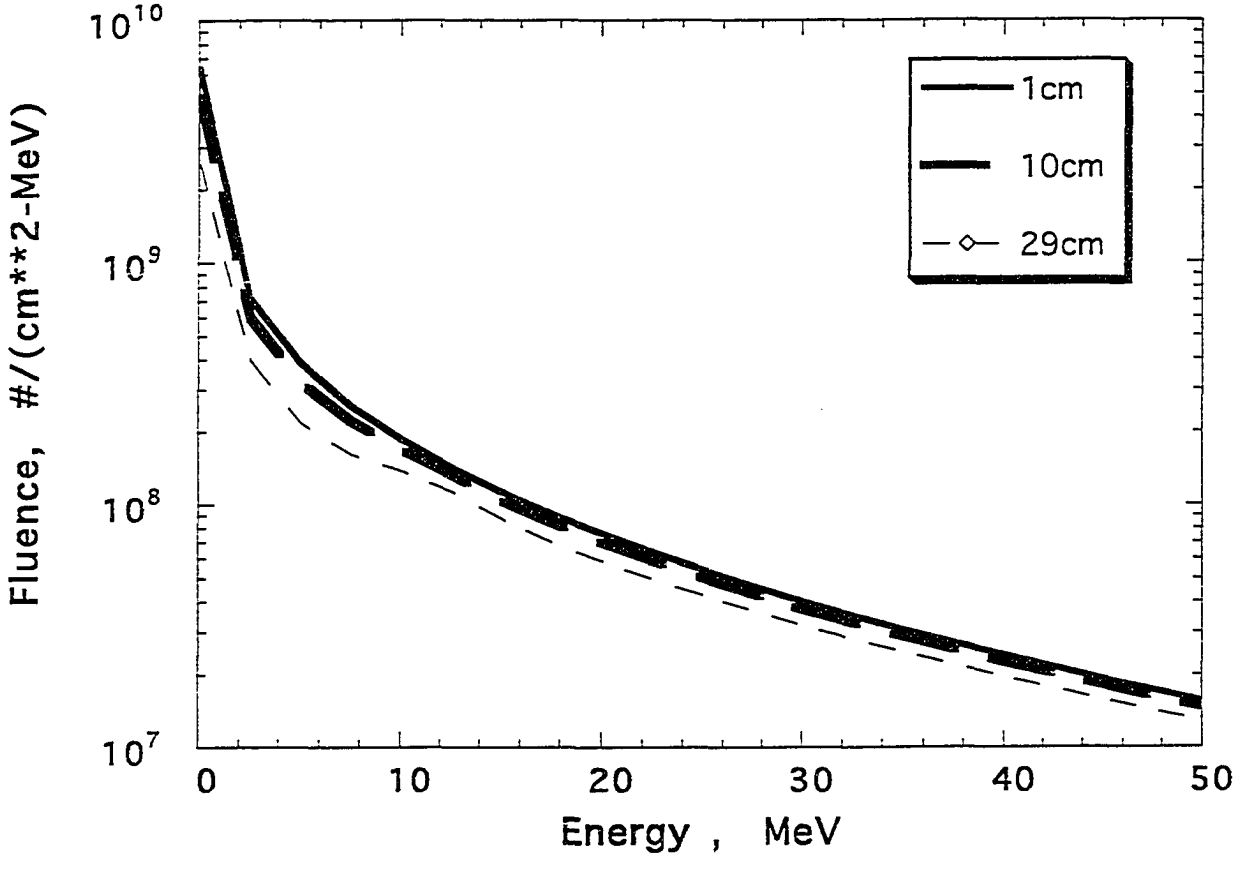

Fig. 48 Primary Neutron Fluence as a Function of Energy for Several Penetration Depths. Neutrons Incident on Lead Slab.

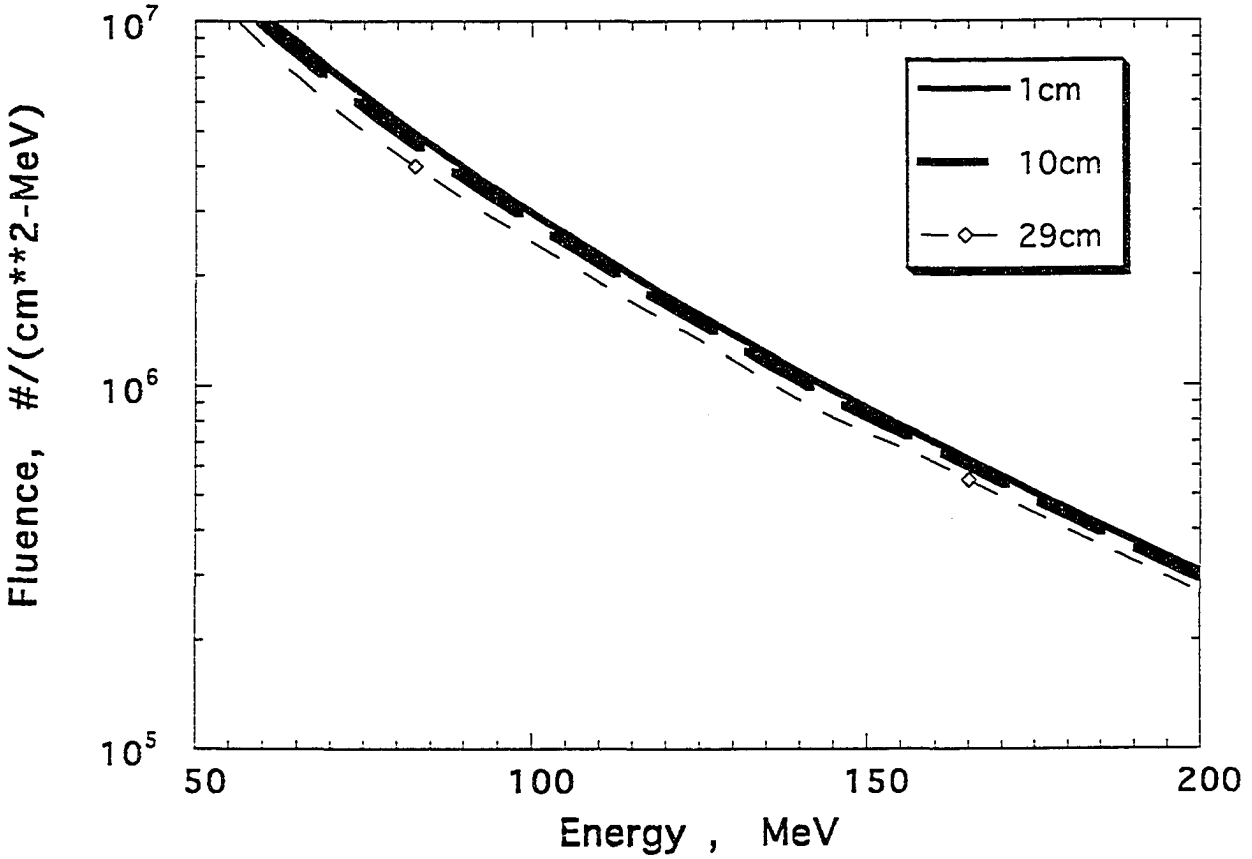

Fig. 49 Primary Neutron Fluence as a Function of Energy for Several Penetration Depths. Neutrons Incident on Lead Slab.

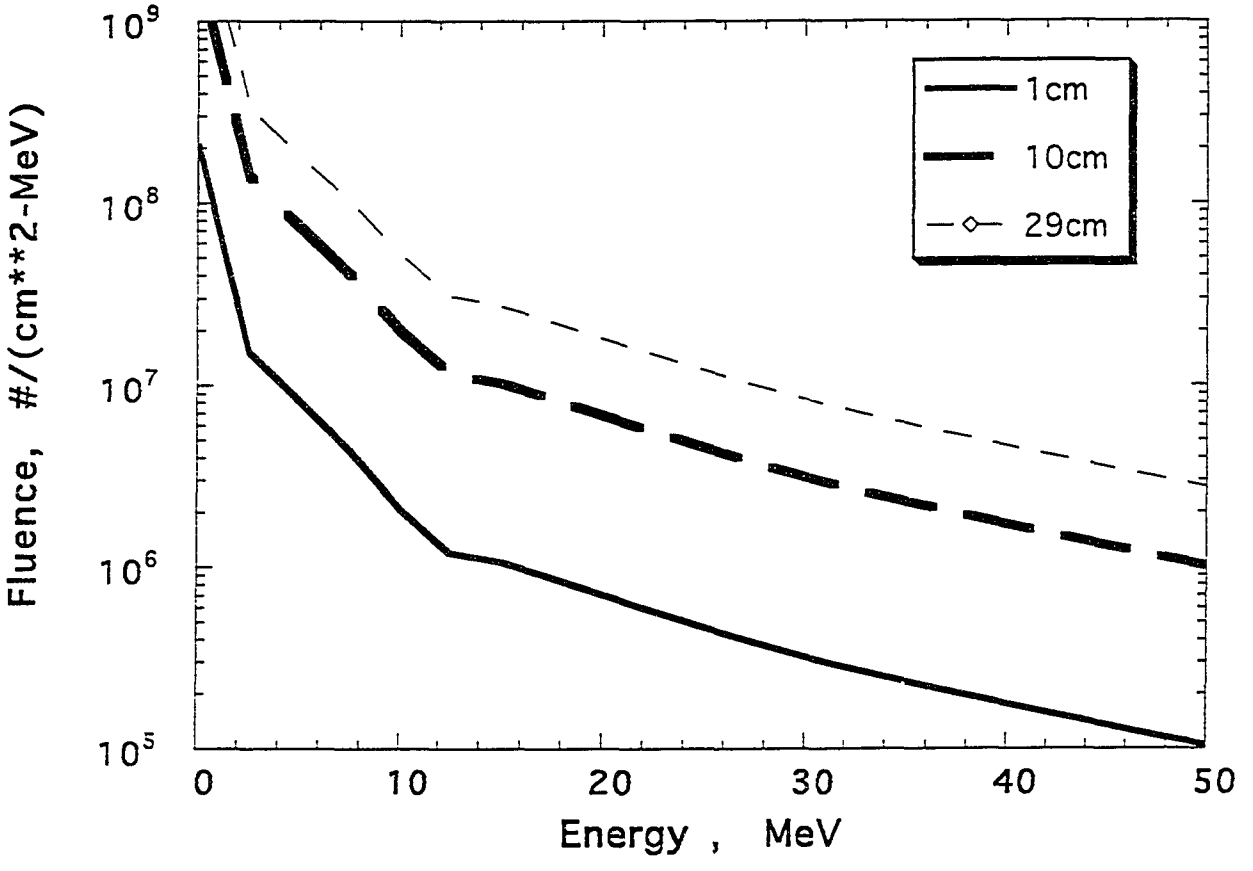

Fig. 50 Rescattered Neutron Fluence as a Function of Energy for Several Penetration Depths. Neutrons Incident on Lead Slab.

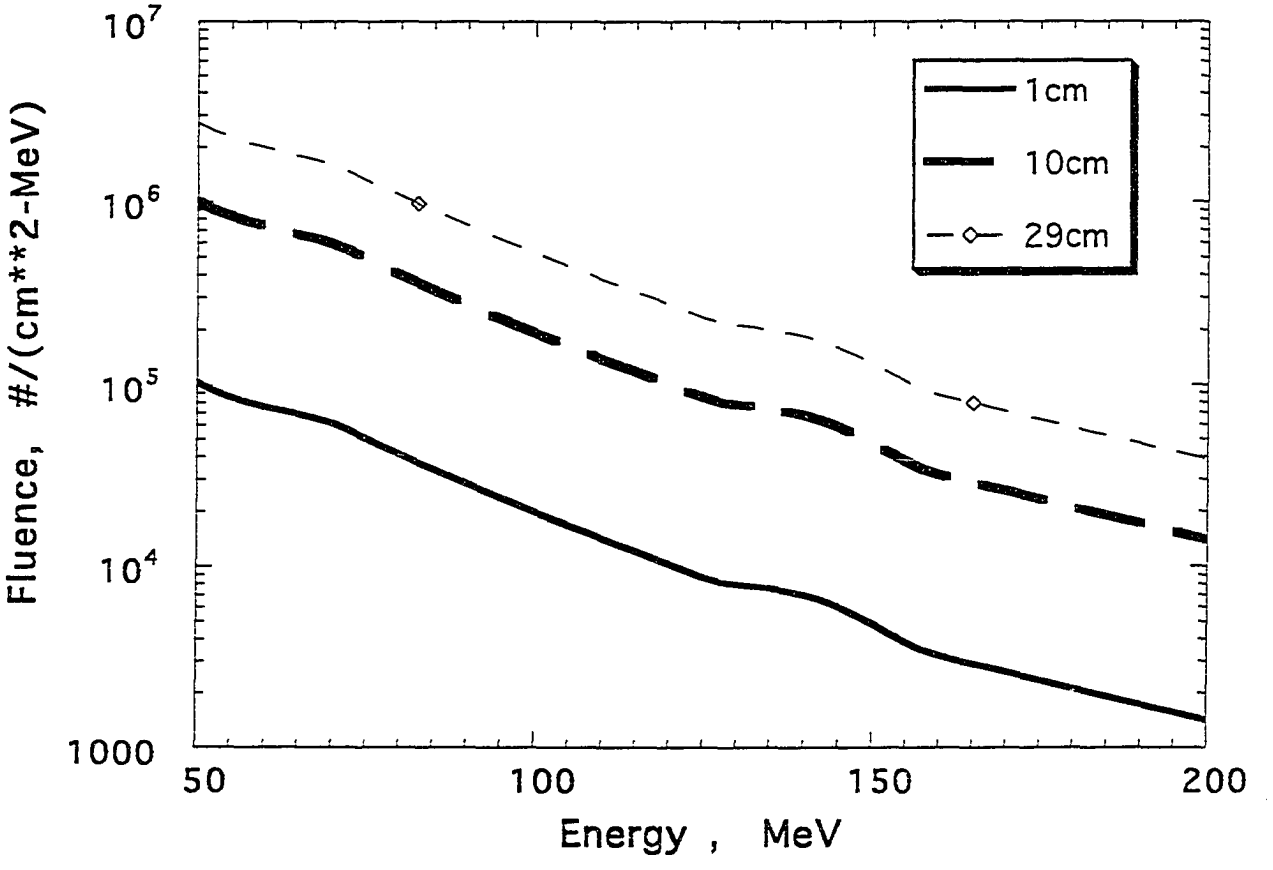

Fig. 51 Rescattered Neutron Fluence as a Function of Energy for Several Penetration Depths. Neutrons Incident on Lead Slab.

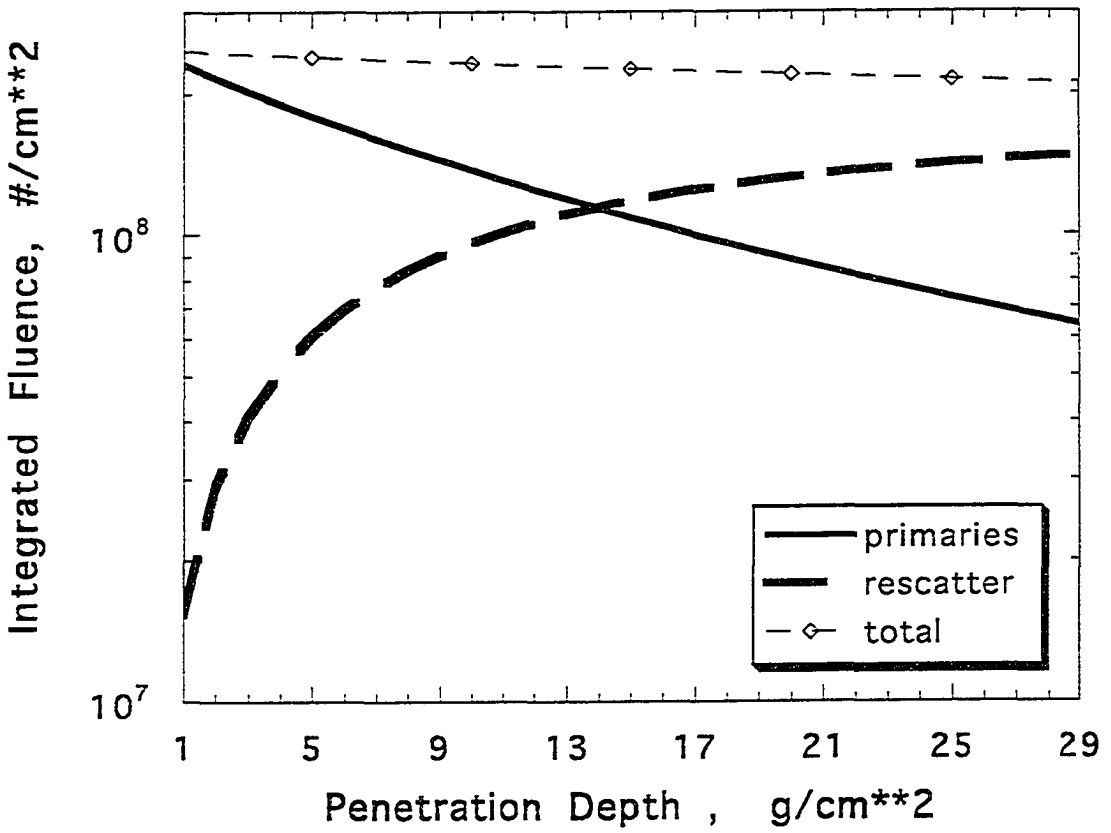

Fig. 52 Integrated Fluence. Elastically Scattered Neutrons in Beryllium Slab

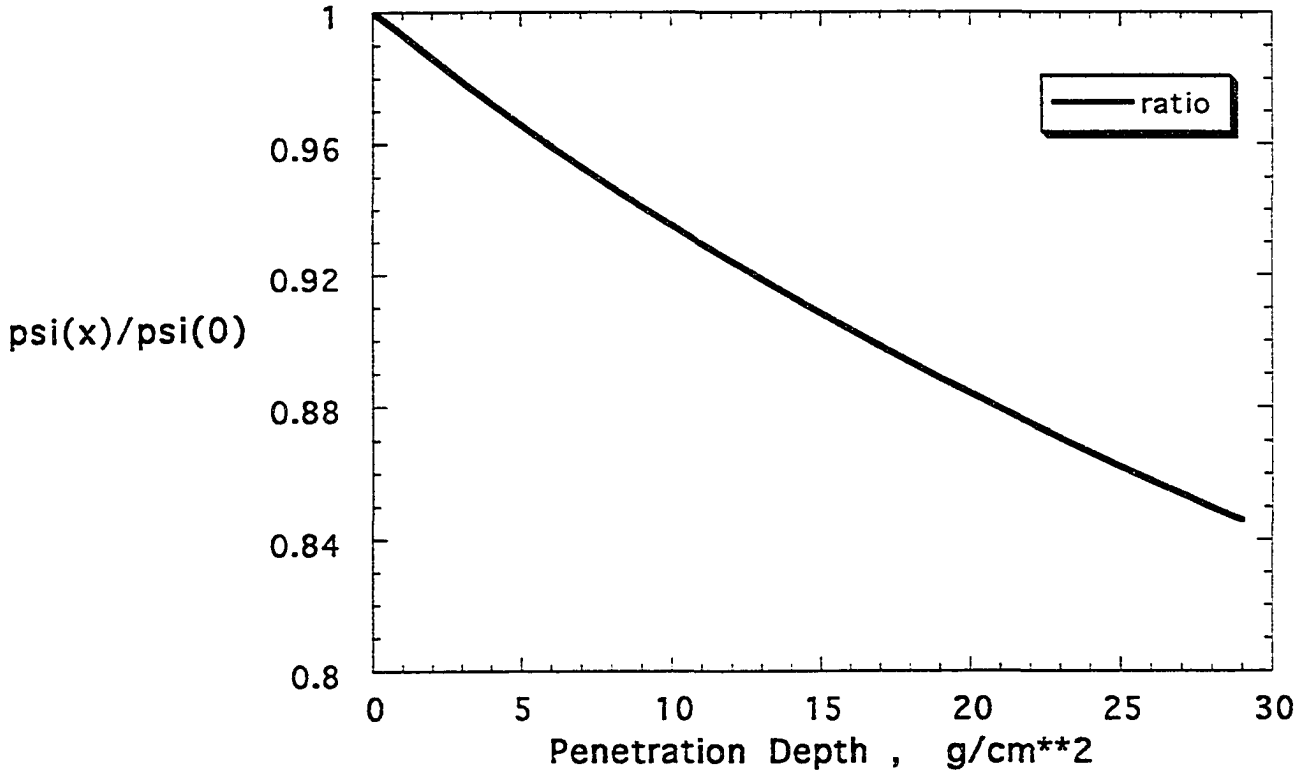

Fig. 53 Convergence Ratio. Elastically Scattered Neutrons in Beryllium.

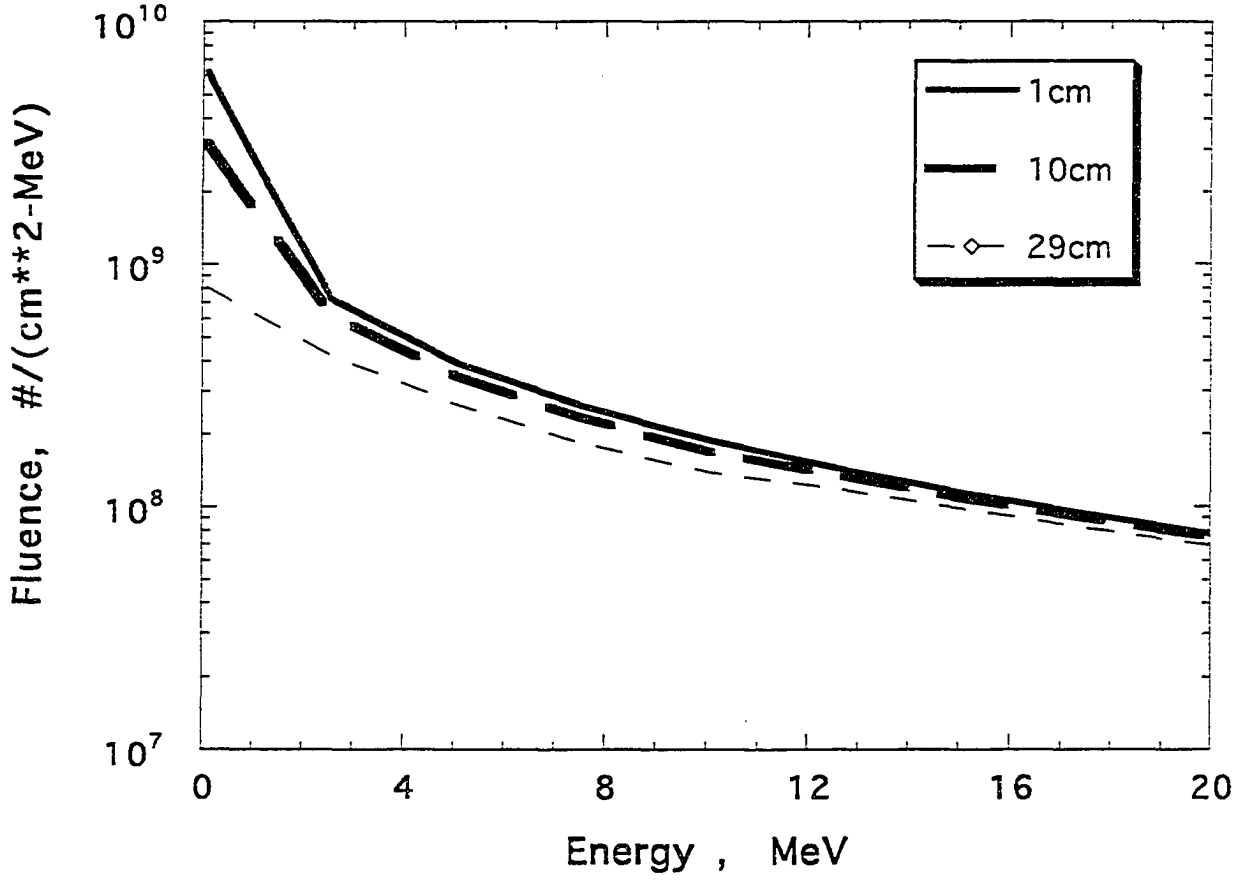

Fig. 54 Total Neutron Fluence as a Function of Energy for Several Penetration Depths. Neutrons Incident on Beryllium Slab.

The differences between neutron scattering in Beryllium and in Aluminum and lead can be understood by examining their respective $\overline{Q}$ spectra. Table 15 shows $\overline{Q}$ as a function of neutron kinetic energy for Beryllium, Aluminum, and Lead. The values of $\overline{Q}$ in Beryllium are consistently greater than for Aluminim by a factor of 4. The lead values are lower by two orders of magnitude. This means that the energy shift process in Beryllium is significantly more efficient than in the behavior elements. So neutrons are elastically slowed to the thermalization energy (for BRYNTRN at 0.1 MeV) at a faster rate in Beryllium. Neutrons which fall below this cut-off are removed from the beam.

Some of the particle loss from figure 53 is, of course, due to truncation error. In order to estimate the effect of truncation error we can add the second order correction to the elastic scattering equation (B.28) which becomes

$$\phi_n(x,E) = e^{-\sigma_n(E)x}\left\{\phi_n(0,E) + \sigma_n(E+\overline{Q})x\phi_n(0,E+\overline{Q}) + \frac{1}{2}\left[\sigma_n(E+2\overline{Q})x\right]^2\phi_n(0,E+2\overline{Q})\right\} \tag{B.33}$$

In figure 55 we plot the integrated fluence for elastically scattered neutrons in Beryllium slab using equation (B.34) with the second order correction. The results are not discernibly different from the first order result of figure 52. However, the plot of the convergence ratio in figure 56 shows a 2% increase at a penetration depth of 29 g/cm^2 when compared to figure 53. The effect, then, is discernable but not large. The spectra plot in figure 57 shows a slight change from the figure 54 result. It can be seen that the < 5 MeV fluence at a penetration depth of 29 g/cm^2 is slightly increased when compared to figure 54. So truncation error is not a significant factor in the deviation from particle conservation for the elastic scattering model applied to neutrons in Beryllium. We note that addition of the second correction has roughly the same effect on the solution as halving the integration step size h, but requires little increase in cpu time. Halving h, however, doubles in cpu usage.

In this appendix we have shown that neutron elastic scattering may be reasonably approximated physically as an energy shift on the particle fluence. This insight led to

Table 15. $\overline{Q}$ as a Function of Projectile Kinetic Energy for Elastically Scattered Neutrons in Beryllium, Aluminum and Lead Shields

E MeV	$\overline{Q}(E)$		
	Beryllium $A_T = 9$	Aluminum $A_T = 27$	Lead $A_T = 207$
0.1	.1757E-1	.6650E-2	.8805E-3
5	.4288E0	.1055E0	.4827E-2
10	.4673E0	.1071E0	.4837E-2
20	.4765E0	.1082E0	.4857E-2
50	.4962E0	.1111E0	.4904E-2
100	.5169E0	.1141E0	.4952E-2
200	.5097E0	.1128E0	.4940E-2
300	.4533E0	.1041E0	.4809E-2
400	.3792E0	.9173E-1	.4591E-2
500	.3104E0	.7900E-1	.4324E-2

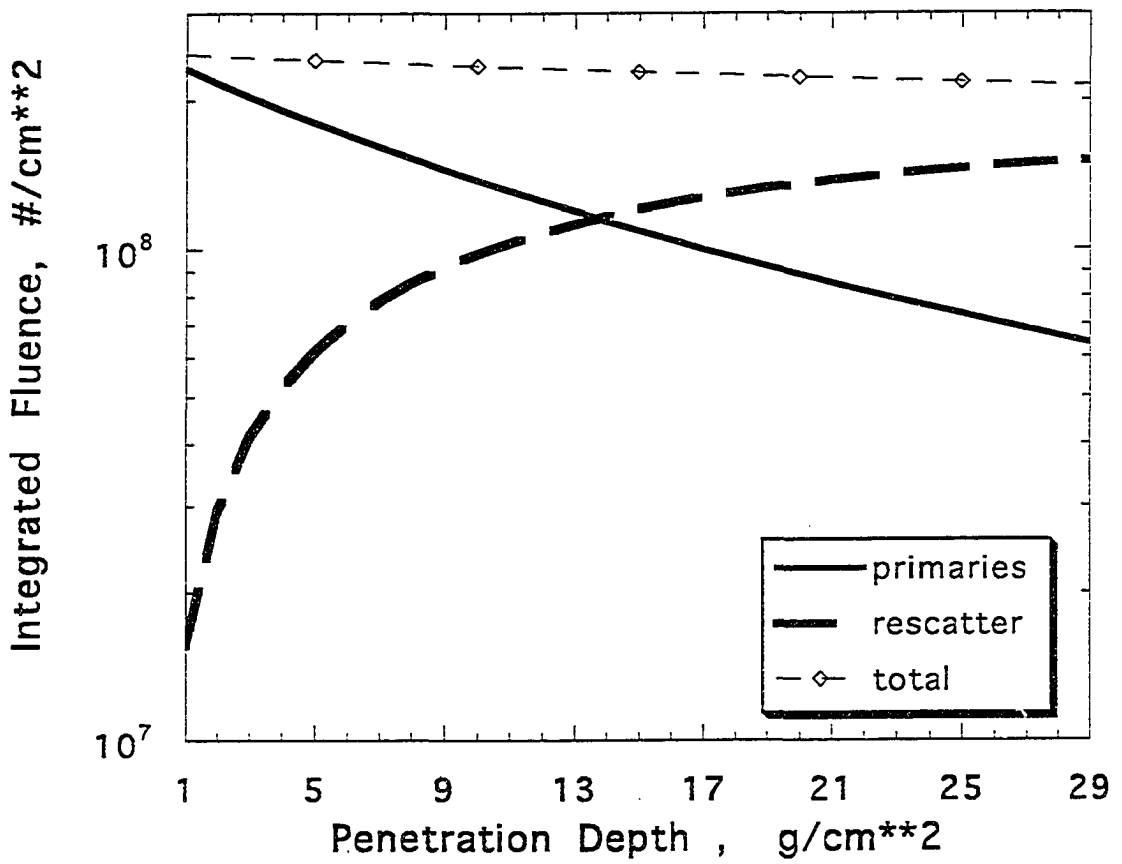

Fig. 55 Integrated Fluence. Elastically Scattered Neutrons in Beryllium Slab. Second order correction added.

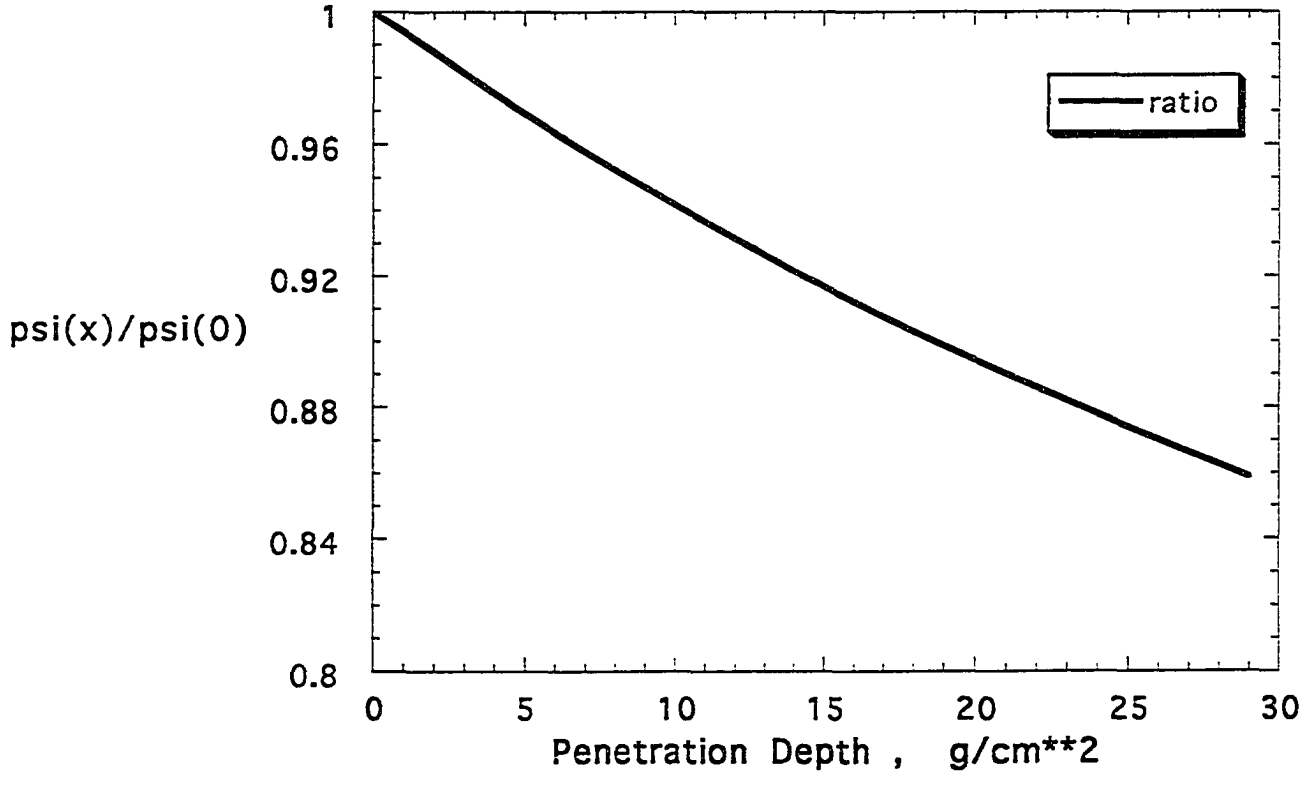

Fig. 56 Convergence Ratio. Elastically Scattered Neutrons in Beryllium. Second Order Correction Added.

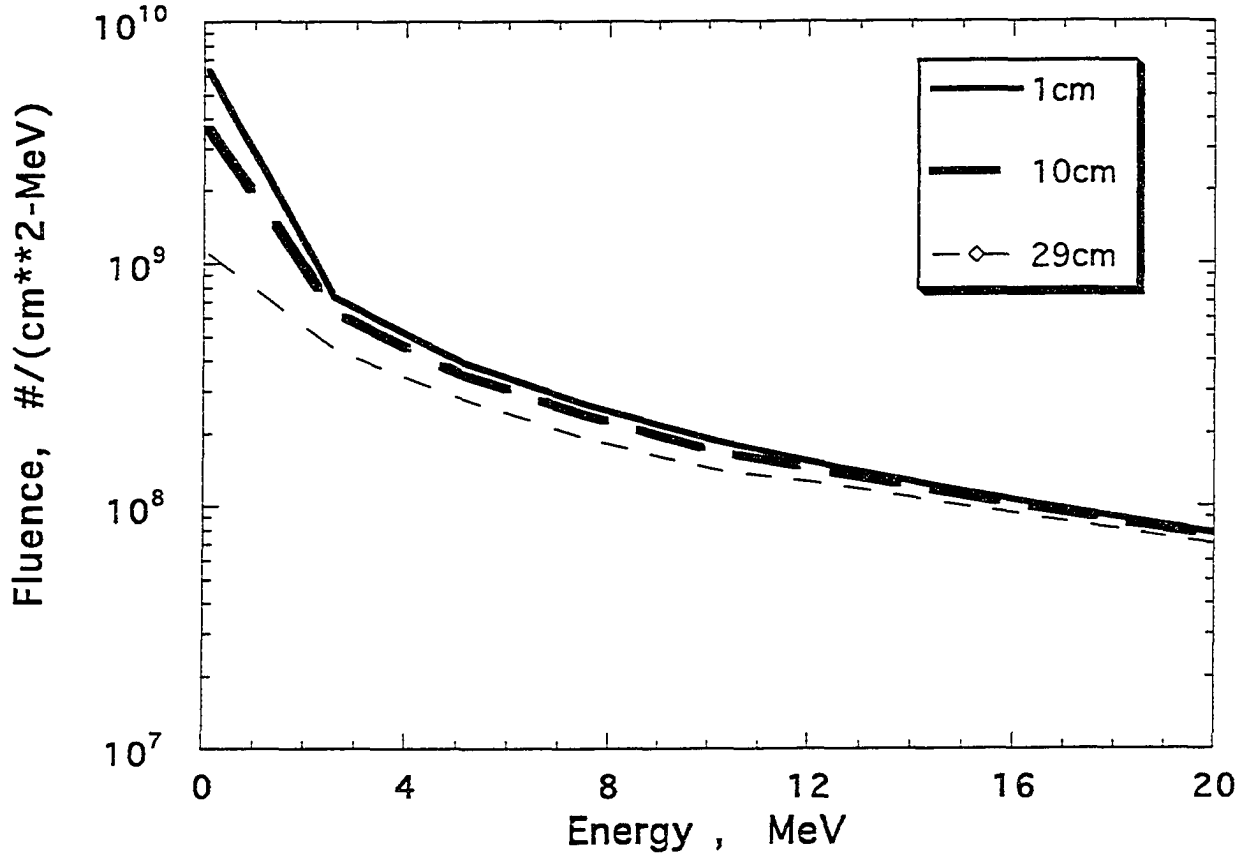

Fig. 57 Total Neutron Fluence as a Function of Energy for Several Penetration Depths. Neutrons Incident on Beryllium Slab. Second Order Corrections added.

the development of a simple model whose implementation requires only a small increase in computational resources.

Appendix C. Target and Projectile Flux

The particle fluence in high energy nucleon transport comes from three sources (1) incident beam (2) high energy nucleons produced in "knockout" interactions, and (3) target fragmentation products of nonelastic collisions. The knockout nucleons or "secondary" particles are scattered into a small cone of solid angle which is highly collimated in the forward direction. The target fragments are usually heavy ions isotropically scattered with low kinetic energy. Recalling equation (31) we can write the transport as[6]

$$\begin{aligned} B_j\phi_j(x,E) = S^T_{jk}\phi_k(x,E) \\ + S^P_{jk}\phi_k(x,E) \end{aligned} \tag{C.1}$$

Where the target fragmentation flux (T) and the projectile flux (P) are followed separately. The operator S_{jk} is given by

$$S_{jk}\phi_k(x,E) = \sum_k \int dE' F_{jk}(E,E')\phi_k(x,E')$$

and

$$F_{jk} = F^T_{jk} + F^P_{jk}$$

Defining the flux as the sum of two terms we can write

$$\begin{aligned} B_j\phi^P_j(x,E) &= S^P_{jk}\phi^P_k(x,E) + S^P_{jk}\phi^T_k(x,E) \\ B_j\phi^T_j(x,E) &= S^T_{jk}\phi^P_k(x,E) + S^T_{jk}\phi^T_k(x,E) \end{aligned} \tag{C.3}$$

The experiments of Heckman (1975) and the statistical model of Goldhaber (1974) suggest that the probability density for high momentum transfer to fragmentation products is small so that $\phi^T_{jk}(x,E)$ is negligibly small for

$$E \gg (F^T_{jk})^2$$

so for high energy transport

$$\phi^T_{jk}(x,E) \approx 0$$

then

$$B_j\phi_j^P(x,E) \approx S_{jk}^P\phi_k^P(x,E) \tag{C.4}$$

$$B_j\phi_j^T(x,E) \approx S_{jk}^T\phi_k^P(x,E) \tag{C.5}$$

Equation (C.4. for the projectile flux has been decoupled from the target flux equation. This means equation (C.5) can be solved in closed form once an expression for $\phi_{jk}^P(x,E)$ has been obtained. One solution for the target flux gives

$$\begin{aligned}\phi_j^T(x,E) \propto \zeta_j^T(x) \Bigg\{ & \frac{1}{2}\ \text{erfc}\left[\sqrt{\frac{ME}{(F_{jk}^T)^2}}\right] \\ & + \sqrt{\frac{ME}{\pi(F_{jk})^2}}\ \exp\left[\frac{-ME}{(F_{jk}^T)^2}\right]\Bigg\}\end{aligned} \tag{C.6}$$

where the complimentary error function

$$\text{erfc}\ (x) = \frac{2}{\sqrt{\pi}}\int_x^\infty e^{-t^2}dt$$

is related to the incomplete Gamma function and ζ_j^T is

$$\zeta_j^T(x) = \sum_k \int\ dE'\sigma_k(E')\nu_{jk}^T\phi_p(x,E') \tag{C.7}$$

similar to equation (A.18).

Equation (C.6) is not important for propagated flux but is used to calculate the total absorbed dose.

STANLEY L. LAMKIN

Stanley L. Lamkin, a native of Illinois, is a graduate of Ferguson High School, Newport News, Virginia. He entered Old Dominion College, Norfolk, Virginia, in 1965 and graduated with a Bachelor of Science degree in Physics in 1969.

After working as a designer in nuclear projects at the Newport News Shipbuilding Co., he returned to Old Dominion University. His Master of Science degree in Physics was awarded in 1974.

Since 1974, Mr. Lamkin has worked on NASA R&D contracts as a research engineer and as a program manager. His published research areas include aeroacoustics, computational fluid dynamics, and plasma physics. Mr. Lamkin is primarily interested in computational physics problems requiring large-scale systems modeling simulations on supercomputers such as the CRAY-2 and CRAY Y-MP, and also massively parallel syatems. In addition, he has continued an ongoing study of particle transport physics which provided the research foundation for his doctoral dissertation. The results of his work have been documented in over 28 technical publications.

Mr. Lamkin resumed his work at Old Dominion University to pursue a doctoral degree in Applied Physics. His research, in conjunction with NASA Langley Research Center, focused on high energy nucleon transport in one dimension.

He was co-author of the outstanding technical publication in the Space Directorate (1992) at NASA Langley and the Structures Directorate (1988). In 1991 he was named the recipient of an honorary NASA Superior Accomplishment Award. Mr. Lamkin is an Associate Fellow of the American Institute of Aeronautics and Astronautics and president-elect of the Hampton Roads section. He is also a member of Sigma Xi Research Society and the Society of Industrial and Applied Mathematics.